Anisotropy in Patterned Perovskite Oxides

Maarten Nijland

ANISOTROPY IN PATTERNED PEROVSKITE OXIDES

MAARTEN NIJLAND

PH.D. COMMITTEE

Chairman and secretary

Prof. dr. ir. J.W.M. Hilgenkamp	University of Twente

Supervisors

Prof. dr. ir. J.E. ten Elshof	University of Twente
Prof. dr. ing. A.J.H.M. Rijnders	University of Twente

Co-supervisor

Dr. ir. G. Koster	University of Twente

Members

Prof. dr. N. Pryds	DTU, Technical University of Denmark
Prof. dr. I. van Driessche	Ghent University
Prof. dr. T. Banerjee	University of Groningen
Prof. dr. B. Dam	Delft University of Technology
Prof. dr. ir. H.J.W. Zandvliet	University of Twente
Prof. dr. ing. D.H.A. Blank	University of Twente

COVER Photograph of a branch of a white birch found in rural estate "De Hellendoornse Berg", Hellendoorn, the Netherlands, symbolizing anisotropy and patterning.

The research described in this thesis was carried out in the Inorganic Materials Science group within the faculty of science and technology, and the MESA$^+$ Institute for Nanotechnology at the University of Twente. This work was financially supported by the Chemical Sciences division of the Netherlands Organization for Scientific Research (NWO-CW) in the framework of the TOP program.

Anisotropy in Patterned Perovskite Oxides
Ph.D. Thesis, University of Twente, Enschede, the Netherlands
Printed by CPI Royal Wöhrmann, Zutphen, the Netherlands

DOI:10.3990/1.9789036537681
ISBN: 978-90-365-3768-1

ANISOTROPY IN PATTERNED PEROVSKITE OXIDES

PROEFSCHRIFT

ter verkrijging van
de graad van doctor aan de Universiteit Twente,
op gezag van de rector magnificus,
Prof. dr. H. Brinksma,
volgens besluit van het College voor Promoties
in het openbaar te verdedigen
op woensdag 26 november 2014 om 12:45 uur

door
Maarten Nijland
geboren op 28 juli 1986
te Hellendoorn

Dit proefschrift is goedgekeurd door de promotoren
Prof. dr. ir. J.E. ten Elshof
Prof. dr. ing. A.J.H.M. Rijnders

en de copromotor
Dr. ir. G. Koster

TABLE OF CONTENTS

Acronyms

AFM	Atomic Force Microscopy	2, 4–6
AsB	Angle selective Backscattered	2
EBSD	Electron BackScatter Diffraction	2, 4–6
EDX	Energy Dispersive X-ray spectroscopy	3
EsB	Energy selective Backscattered	2, 5
FIB	Focused Ion Beam	2
FWHM	Full Width at Half Maximum	2, 4, 5
HCNO	$HCa_2Nb_3O_{10} \cdot 1.5\,H_2O$	4, 5
HE-SE2	High Efficiency Secondary Electron	2
HR	High-Resolution	3–6
HTO	$H_{1.07}Ti_{1.73}O_4 \cdot H_2O$	4, 5
MEMS	MicroElectroMechanical Systems	2–4
MiMiC	Micro Molding in Capillaries	2
MOKE	Magneto-Optic Kerr Effect	2, 5
NIL	Nano Imprint Lithography	6
NTM	Nano Transfer Molding	2
PAA	Poly(Acrylic Acid)	2, 6
Pc	*pseudo*-cubic	1, 3–5
PDMS	PolyDiMethylSiloxane	2, 6
PET	Poly(Ethylene Terephthalate)	6
PFM	Piezoresponse Force Microscopy	3
PLD	Pulsed Laser Deposition	1–6
PMMA	Poly(Methyl MethAcrylate)	2, 6

PPMS	Physical Properties Measurement System	2, 4, 5
PS	PolyStyrene	6
RHEED	Reflection High Energy Electron Diffraction	2, 5
RIE	Reactive-Ion Etching	6
RMS	Root Mean Square	2, 4, 5
SAMs	Self-Assembled Monolayers	6
SE	Secondary Electron	2
SEM	Scanning Electron Microscopy	3–6
TM	Tapping Mode	2, 4–6
TUNA	Tunneling Atomic Force Microscopy	2
U.C.	Unit Cells	5
UV	UltraViolet	1, 2, 6
VSM	Vibrating Sample Magnetometer	2, 4, 5
XPS	X-ray Photoelectron Spectroscopy	5
XRD	X-Ray Diffraction	2–6
XRR	X-Ray Reflectivity	5
YSZ	Yttria-Stabilized Zirconia	3, 4

1 ANISOTROPY IN PATTERNED PEROVSKITE OXIDES

> "WE LIVE IN A UNIVERSE OF PATTERNS."
> – IAN STEWART

Patterns are everywhere,[1] from the immense shapes of galaxies down to the nanostructures in the wings of butterfly species,[2] and from the dynamic development of cloudscapes to the seemingly frozen shapes of fossils. Nature provides stunning examples of regularities that are not just fascinating by their looks, but even more so by serving clear purposes while benefiting from millions of years of evolution. Some of the most intriguing examples include the peculiar decorations on some spider webs, which are used to attract insect pollinators by reflecting ultraviolet (UV) light in a similar way as some flowers do;[3] or the alternating microstructure of hydrophobic and hydrophilic patches on the back of some beetles, which allows them to collect drinking water from early morning fog in areas where rainfall is negligible.[4]

Having a *multi*-million year head start on patterning, nature has been an inexhaustible source of inspiration to contemporary technology, and many research efforts have aimed for mimicking natural patterns.[5,6] For instance, lotus leafs were studied to fabricate superhydrophobic micro- and nanostructured surfaces,[7] and spider silk inspired other researchers to make artificial fibers on which directional water collection was illustrated.[8] Besides introducing or improving functionalities of a certain material, patterning has also been used to engineer electrical circuits with the aim to fit a maximum number of active components (*e.g.* transistors, diodes, bits) on an area that is as small as possible. Artificial patterning is clearly rapidly catching-up with nature, and heading towards the ability to shape functional materials with control in the atomic limit.

Pulsed laser deposition (PLD) allows manipulating material at an atomic level, however, only in the direction of film growth. In the utilization of this technique, single crystalline substrates with matching lattice parameters are generally used to realize heteroepitaxial growth. These substrates are heated to several hundred degrees Celsius to promote surface mobilities of the adatoms and reach full control of growth, yielding thin films that are structurally ordered with the underlying substrates. The intrinsic properties of the deposited materials are not necessarily preserved in these films, as effects imposed by lattice matching may play a decisive role. For example, bulk $SrTiO_3$ is not ferroelectric at any temperature, but can be rendered in such state even at room temperature by straining it to $DyScO_3$.[9] Similarly, the polarization of $BaTiO_3$ can be enhanced by straining the material in an asymmetric environment of $SrTiO_3$ and $CaTiO_3$.[10] In the case of artificially layered $PbTiO_3$ and $SrTiO_3$, rotational distortions lead to new ground states and properties that are not present in the individual materials.[11]

All three examples were realized by using building blocks of the perovskite ABO_3 class of materials, which has tremendous potential for many applications. It allows an extensive number of cations on either the A or B site, and encompasses materials with very divergent properties: ranging from superconducting and metallic to semiconducting, or from di-, piezo- and ferroelectric, and from anti- and ferromagnetic, to multiferroic. The foregoing examples illustrate that the potential uses of these materials are greatly expanded by the possibility for strain or interfacial engineering, facilitated by the commensurate unit cell dimensions and common oxygen backbone of the different perovskite materials.

The intention of this thesis is to contribute to the ambitious objective to hold on to the unprecedented control of film growth that PLD offers, while at the same time reach for similar control in directions normal to that of growth. State-of-the-art lithographic techniques like those used for manufacturing logic or memory chips are incompatible with PLD, because they make use of organic polymers that degrade at elevated temperatures. Parallel patterning of epitaxial perovskite materials in arbitrary shapes is therefore still challenging even on micrometer length scales, illustrating the tremendous gap to reach atomic scale precision. No methods to achieve atomic accuracy are described in this thesis as well, but different routes are discussed to pattern epitaxial heterostructures on micrometer length scales and below. The structures and their properties are treated with a special emphasis on anisotropy, which may originate either from the shapes of the patterns, or the crystallographic order resulting from heteroepitaxy.

In this thesis, patterning of epitaxial perovskites is described from two perspectives: either from the viewpoint of a material or its crystal orientation. Regarding the first aspect, routes are discussed to pattern thin films by using sacrificial micro- or nanostructures to shield part of a substrate from interactions with a perovskite material. These sacrificial patterns can be introduced either before or during PLD and selectively removed afterwards. The notion of using soft lithography to mold metal oxide stencil masks onto single crystalline substrates is worked out, which allows bottom-up patterning of epitaxial films during subsequent high temperature depositions. Alternatively, self-organization events can be used to form nanostructures of one phase into a matrix of a sacrificial phase, where both phases may be simultaneously deposited. The second part of this thesis covers an entirely new concept to pattern the crystallographic orientation of a thin film rather than the material itself; an idea that is particularly interesting for materials that exhibit strong anisotropy. In essence, seed layers of inorganic nanosheets can be used to realize heteroepitaxial growth on substrates that do not allow for epitaxy by themselves. By patterning nanosheets with different lattice parameters, the strain, orientation, and properties of perovskite thin films can be locally tailored. The different approaches of patterning epitaxial thin films expounded in this thesis do not inevitably interfere with the high control of growth that can be reached with PLD. As demonstrated, these structures may have properties that are both reminiscent of fully oriented unpatterned thin films and simultaneously show clear influences from patterning, making them potentially useful for different electronic and electromechanical applications.

OUTLINE

In chapter 2, soft lithographic methods are described to pattern epitaxial films of $La_{0.67}Sr_{0.33}MnO_3$ and $SrRuO_3$ on (*sub*-)$\mu\mathrm{m}$ length scales. A two step, bottom-up process was developed benefiting from a first molding step to fabricate ZnO stencil masks, followed by PLD and lift-off to obtain epitaxial micro- and nanostructures. All analyses and characterizations indicated that the high degree of control in the direction of growth was maintained, while additional functionalities were added from shaping these materials. Magnetostatic anisotropy was found in epitaxial line patterns of $La_{0.67}Sr_{0.33}MnO_3$, the significance of which was illustrated by detailed analyses of all sources of anisotropy. In addition, electrical isolation was found in patterns of $SrRuO_3$, and signatures of local effects were found that may have been the result of a different chemical environment at the edges leading to local relaxation of epitaxial stress. The methods presented in this chapter offer unique advantages to current alternatives, as they are fast, inexpensive, practicable in any lab, and allow fabrication of patterns that can not be prepared by any other parallel patterning technique.

The next chapter discusses the concept of using self-organization to fabricate nanostructured material in a single deposition step. PLD was conducted with mixed targets consisting of ferroelectric $PbZr_{0.2}Ti_{0.8}O_3$ and (piezoelectric) ZnO, yielding nanocomposite films in which both phases were separated on nanometer length scales. By carefully controlling deposition conditions, ferroelectric nanopillars were formed, of which the tetragonality and piezoresponse increased after removal of the ZnO matrix. Electromechanical responses did not reach that expected for $PbZr_{0.2}Ti_{0.8}O_3$, possibly due to considerable off-stoichiometry and attack of these features during etching. Nonetheless, the combination of heteroepitaxy and a high surface area may lead to applications in, for instance, piezoelectric transducers. Additionally, the work may act as model for other perovskite/ZnO nanocomposites, extending the potential use to fields like those of catalysis or sensing.

Chapter 4 illustrates that inorganic nanosheets can be used to control the morphology, crystal orientation, and magnetic properties of $SrRuO_3$ thin films on arbitrary substrates. Two types of nanosheets were used: $Ca_2Nb_3O_{10}$ to realize $(001)_{\mathrm{pc}}$ oriented film growth, and $Ti_{0.87}O_2$ to effect growth in the $[110]_{\mathrm{pc}}$ direction (pc refers to the *pseudo*-cubic unit cell of $SrRuO_3$). Lattice matching between the films and nanosheets led to heteroepitaxy, where the oxygen octahedral backbones of the nanosheets persisted throughout the films. Magnetic anisotropy was measured for these films, in which a determinant role for the nanosheets was demonstrated. The perovskite material was also deposited on a mixed monolayer of both types of nanosheets, illustrating their capability to locally tailor the structure and properties of thin films.

Chapter 5 continues on the same topic, and describes ways to improve growth of $SrRuO_3$ on both types of nanosheets. Atomically smooth growth was realized on $Ca_2Nb_3O_{10}$ by introducing a buffer layer of $SrTiO_3$, and an increased preference for the $(110)_{\mathrm{pc}}$ orientation was achieved by using two layers of $Ti_{0.87}O_2$ nanosheets. Resulting films showed properties that were approximate to those of fully oriented layers, illustrating that nanosheets provide a viable alternative to costly single crystalline substrates. A route was developed to pattern both types of nanosheets on a single substrate, and a perovskite thin films was deposited of which the strain, texture and properties were determined by the pattern. This concept opens up completely new avenues to engineer functionalities in thin films.

Chapter 6 concludes this thesis with an outlook, containing preliminary results that sprang from the work presented in the preceding chapters. The limits of soft lithographic molding are discussed, as well as two alternative methods that may lead to further miniaturization of the patterns. The second part of this chapter evaluates methods for growing epitaxial films on nanosheets supported on thermally stable substrates, and transporting these films onto polymeric substrates for application in flexible electronics.

REFERENCES

[1] I. Stewart. "Chap. 1: The Natural Order". In: *Nature's numbers: The unreal reality of mathematics*. New York: Basic Books, 1995.

[2] P. Vukusic and J. R. Sambles. "Photonic structures in biology". *Nature*, **424** (6950):852–855, 2003.

[3] C. L. Craig and G. D. Bernard. "Insect attraction to ultraviolet-reflecting spider webs and web decorations". *Ecology*, **71** (2):616–623, 1990.

[4] A. R. Parker and C. R. Lawrence. "Water capture by a desert beetle". *Nature*, **414** (6859):33–34, 2001.

[5] B. Bhushan. *Biomimetics: Bioinspired hierarchical-structured surfaces for green science and technology*. Berlin Heidelberg: Springer Science & Business Media, 2012.

[6] S. S. R. Kumar, ed. *Biomimetic and bioinspired nanomaterials*. Weinheim: John Wiley & Sons, 2010.

[7] Z. Guo, F. Zhou, J. Hao, and W. Liu. "Stable biomimetic super-hydrophobic engineering materials". *J. Am. Chem. Soc.* **127** (45):15670–15671, 2005.

[8] Y. Zheng, H. Bai, Z. Huang, X. Tian, F.-Q. Nie, Y. Zhao, J. Zhai, and L. Jiang. "Directional water collection on wetted spider silk". *Nature*, **463** (7281):640–643, 2010.

[9] J. H. Haeni, P. Irvin, W. Chang, R. Uecker, P. Reiche, Y. L. Li, S. Choudhury, W. Tian, M. E. Hawley, B. Craigo, A. K. Tagantsev, X. Q. Pan, S. K. Streiffer, L. Q. Chen, S. W. Kirchoefer, J. Levy, and D. G. Schlom. "Room-temperature ferroelectricity in strained $SrTiO_3$". *Nature*, **430** (7001):758–761, 2004.

[10] H. N. Lee, H. M. Christen, M. F. Chisholm, C. M. Rouleau, and D. H. Lowndes. "Strong polarization enhancement in asymmetric three-component ferroelectric superlattices". *Nature*, **433** (7024):395–399, 2005.

[11] E. Bousquet, M. Dawber, N. Stucki, C. Lichtensteiger, P. Hermet, S. Gariglio, J. M. Triscone, and P. Ghosez. "Improper ferroelectricity in perovskite oxide artificial superlattices". *Nature*, **452** (7188):732–736, 2008.

2

PATTERNING OF EPITAXIAL PEROVSKITES FROM MICRO AND NANO MOLDED STENCIL MASKS

A process was developed that combines soft lithographic molding with PLD to make heteroepitaxial patterns of functional perovskite oxide materials. Micro- and nanostructures of sacrificial ZnO were made by micro molding in capillaries (MiMiC) and nano transfer molding (NTM), respectively, and used to screen the single crystalline substrates during subsequent PLD. ZnO was used because of its compatibility with the high temperatures reached during PLD and because of the ease of its removal after use by benefiting from its amphoteric nature. *Sub*-micrometer sized lines of $La_{0.67}Sr_{0.33}MnO_3$ were made by the transfer molding approach, in which the anisotropic features expected for a fully oriented thin film were preserved and a magnetostatic contribution from the line shapes was introduced. Different patterns of $SrRuO_3$ were made with lateral dimensions of a few micrometers, for which electrical isolation was illustrated. The bottom-up soft lithographic methods can be compliantly utilized for making epitaxial structures of various shapes and sizes in the $\mu\mathrm{m}$ down to the nm range, and offer unique opportunities for fundamental studies as well as for realizing technological applications.

2.1 INTRODUCTION

Physical vapor deposition techniques like PLD have evolved to a level in which atomic scale control is achieved in the direction of film growth. The high degree of control has facilitated preparation of artificial oxide materials with properties that strongly diverge from those of the individual building blocks, and has made the exploration of a wealth of interesting phenomena possible.[1–4] The ability to control the lateral position of materials on substrates is also required to allow future device integration. Patterning of oxide films can be accomplished via collisions with highly energetic particles that selectively remove the undesired parts. An example is focused ion beam (FIB) milling, which is well developed and allows fabrication of *sub*-100 nm features,[5,6] but is limited by inherent drawbacks including deterioration of the generated surfaces and issues related to the serial nature of such top-down approaches.[7,8] When it comes to patterning of complete films on the scale of substrates or wafers, parallel patterning methods are required to overcome the time-consuming character and low throughputs that are inextricably bound to serial techniques.

Only a handful of methods are currently available that allow parallel patterning of thin films while keeping the crystallographic orientation in control. All of these techniques rely on the use of top-down fabricated stencil masks to shield parts of the substrate and enable bottom-up formation of epitaxial structures during their depositions. Efforts were made to apply reusable silicon nitride membranes during PLD,[9–11] but issues like the need to deviate from optimal deposition conditions, limitations in shapes, and rapid degradation of the masks, led to the development of sacrificial stencil masks. Particular interest has been given to anodic aluminum oxide (AAO) membranes, with which nm-sized epitaxial arrays of oxide nanodots were made, but owing to the self-organized formation of these membranes, patterns were poorly ordered and limited to a single shape of restricted sizes.[12–14] Photolithography was recently used to pattern sacrificial metal oxide stencil masks and fabricate epitaxial microstructures in arbitrary shapes, however, with lateral dimensions of several micrometers and with limited throughputs due to the vapor deposition step used to deposit the sacrificial metal oxide.[15–17]

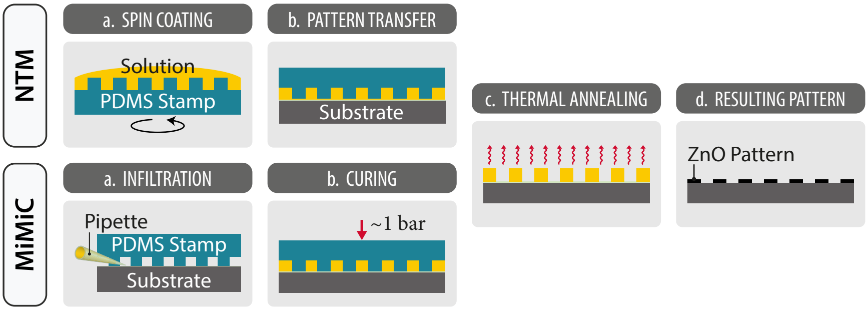

Figure 2.1: Schematic representations of the transfer molding and MiMiC processes to make ZnO stencil masks on single crystalline substrates for patterning of epitaxial oxides by PLD. In the case of transfer molding, (a) the solution is spin coated on the mold, (b) the mold is then placed on a substrate coated with a PMMA film, and the assembly is transferred to a hot stage at $80\,^{\circ}\mathrm{C}$ to allow the pattern to cure. In the case of MiMiC, (a) a PDMS mold is placed on a substrate (coated with a PMMA film) and the precursor solution is added in front of the channels, which are then filled spontaneously by capillary action. After complete filling of the channels, (b) the sample is heated to $60\,^{\circ}\mathrm{C}$ and a pressure of ~ 1 bar is applied to allow further curing. After curing the pattern (either made by MiMiC or transfer molding), (c) the mold is removed and the sample is thermally annealed to convert the polymeric precursor into (d) ZnO.

In spite of all progress made in parallel patterning of metal oxide thin films, a facile method with which epitaxial micro- and nanostructures can be made in arbitrary shapes and with high fidelity is still lacking. Originally introduced by the group of Whitesides,[18–21] a family of bottom-up methods that uses patterned elastomeric masks, stamps, or molds, known collectively as 'soft lithography', has evolved to one of the most common approaches to pattern a wide range of different materials on micro- and nanometer length scales.[22,23] Inspired by the multitude of examples of structures made by soft lithography, the potential of combining this technology with PLD was explored, aiming to profit from the distinct advantages of soft lithography while maintaining good control of nucleation and growth of technologically relevant perovskite oxides. The approach consists of two consecutive bottom-up fabrication steps, initiated by molding of sacrificial metal oxide stencil masks on single crystalline substrates (Figure 2.1), and followed by PLD to form negative and fully oriented replicas of perovskite-type oxide materials.

Two types of soft lithography were used, namely micro molding in capillaries (MiMiC) and nano transfer molding (NTM). The transfer molding route was developed to fabricate stencil masks containing features with lateral sizes well below $1\ \mu\mathrm{m}$, while MiMiC was employed to generate larger features. Comparing these two molding approaches, transfer molding requires optimized spin coating parameters to guarantee formation of structures that are sufficiently high but free from residues, while MiMiC does not require such optimization. MiMiC, on the other hand, is limited to open channels with dimensions in the micrometer range,[21] while no such fundamental limits apply to transfer molding. For this reason, both MiMiC and nano transfer molding were considered for the preparation of stencil masks with micrometer and nanometer dimensions, respectively. The stencil masks were made from ZnO, which was selected because of its excellent thermal stability and amphoterism. The first property is required to prevent any form of decomposition during high temperature PLD, and the latter property allows removal of these masks after use in either (weakly) acidic or basic environments, thus creating opportunities to use solutions in wide pH ranges in order to prevent degradation of the PLD grown epitaxial structures. Epitaxial patterns of $La_{0.67}Sr_{0.33}MnO_3$ and $SrRuO_3$ were formed at $750\ ^{\circ}\mathrm{C}$ and $700\ ^{\circ}\mathrm{C}$, respectively, of which the crystallographic structure and properties closely resembled those of unpatterned thin films while additional functionality was added from the patterns. Both perovskite oxide materials were selected because of their potential use as electrode in all oxide epitaxial heterostructures,[24,25] *e.g.* for ferroelectric capacitors,[26,27] microelectromechanical systems (MEMS),[28,29] and field-effect transistors.[30] The half-metallic character[31,32] and high Curie temperature[33] of $La_{0.67}Sr_{0.33}MnO_3$, extend the possible field of application of this material into spintronic devices such as magnetic tunnel junctions.[32,34]

Summarizing, the combination of two powerful techniques, soft lithographic molding and PLD, leads to an unprecedented control of shape and crystallographic orientation. Soft lithographic molding is currently the only parallel patterning approach with which stencil masks can be made in arbitrary shapes, and sizes down to nanometer length scales. In addition, the methods presented here are fast, inexpensive, and practicable in any lab, as no dedicated equipment, nor clean room conditions are required. When used during PLD, the polycrystalline masks allow patterning of epitaxial oxides of which the crystallographic orientations are fully dictated by the underlying substrates. Keeping in mind the unrivaled properties found in epitaxial thin films and the challenges associated with patterning such materials, the approach presented in this chapter may be broadly utilized for future fundamental studies as well as for realizing (all oxide) devices.

2.2 EXPERIMENTAL METHODS

CHEMICALS AND MATERIALS Zinc nitrate hexahydrate (reagent grade, 98%) and poly(acrylic acid) (PAA, $M_\mathrm{w} \sim 1,800\ \mathrm{g\,mol^{-1}}$) were purchased from Sigma-Aldrich. A commercial solution of $2\%\ w/w$ poly(methyl methacrylate) (PMMA, $M_\mathrm{w} \sim 950,000\ \mathrm{g\,mol^{-1}}$) in anisole was obtained from MicroChem. Anisole (99%) and ethanol (99.8%) were acquired from Merck and Assink Chemie, respectively. An ammonium fluoride etching mixture (AF 875-125, puranal) from Honeywell was used in a fume hood inside a lab with an emergency Hexafluorine washing station while wearing protective gloves, protective clothes and eye protection. Ultrapure water with a resistivity of $18.2\ \mathrm{M\Omega\,cm}$ was used. All chemicals were used as received, without additional purification.

Soft lithographic patterns were made either with an aqueous solution (NTM) or with a solution in ethanol (MiMiC). For the first solution, $0.18\ \mathrm{g}$ PAA was completely dissolved in $6\ \mathrm{ml}$ water and then $0.36\ \mathrm{g}$ $Zn(NO_3)_2{\cdot}6\,H_2O$ was added. The other solution was prepared by dissolving $0.36\ \mathrm{g}$ PAA in $5\ \mathrm{ml}$ ethanol and by subsequently adding $0.3\ \mathrm{g}$ $Zn(NO_3)_2\cdot 6\,H_2O$. Both solutions were stirred for at least $48\ \mathrm{h}$ after which they were stored and used within three months.

Nanopatterned silicon masters (part numbers: SNS-C14.3-0808-350-D45-P, S2D-24D3-0808-250/350-P, S2D-24D2-0808-250-P) were purchased from LightSmyth Technologies (Eugene, United States), and micropatterned silicon wafers with a $1\ \mu\mathrm{m}$ oxide layer were obtained from LioniX B.V (Enschede, the Netherlands). The nanopatterned masters were left in the straw (as received) and placed vertically in a desiccator together with a beaker containing $2\ \mu\mathrm{l}$ 1H,1H,2H,2H-perfluorooctyltrichlorosilane (Fischer Scientific, 97%). The glass desiccator was then pumped down to $10\ \mathrm{mbar}$ with a chemistry pumping unit (PC 3001 Vario Pro, Vacuubrand), closed off, and left for 13 to $14\ \mathrm{h}$. The micropatterned masters were silanized with a comparable procedure.

A Sylgard 184 silicone elastomer kit from Dow Corning was used to prepare polydimethylsiloxane (PDMS). The base agent and curing agent were properly mixed in a 10 to 1 weight ratio by mechanical stirring. Air bubbles were subsequently removed in a glass desiccator which was pumped down for at least $10\ \mathrm{min}$ with a standard diaphragm vacuum pump (Vacuubrand). The desired silanized master was placed on a piece of weighing paper on a cold heating plate and was surrounded by a ring of Teflon. The PDMS was then poured on the silanized master and cured at $60\,^\circ\mathrm{C}$ for at least $24\ \mathrm{h}$.

Single crystal (001) oriented $SrTiO_3$ substrates ($5 \times 5\ \mathrm{mm}^2$) were purchased from CrysTec GmbH. These substrates were treated to obtain a single TiO_2 termination according to the procedure of Koster *et al.*[35] The substrates where then protected with a thin layer of PMMA by spin coating $30\ \mu\mathrm{l}$ of a $1\%\ w/w$ solution of PMMA in anisole yielding a layer thickness of approximately $20\ \mathrm{nm}$. The liquid was added to the spin coater (WS-400B-6NPP, Laurell Technologies Corporation) during a spin on stage at $500\ \mathrm{revolutions\ min}^{-1}$. After $5\ \mathrm{s}$, the spinner accelerated to $6000\ \mathrm{revolutions\ min}^{-1}$ and decelerated $60\ \mathrm{s}$ later until it came to a halt. The acceleration or deceleration between every step was fixed at $27.5\ \mathrm{revolutions\ s}^{-2}$. The substrate was subsequently transferred to a hot plate at $160\,^{\circ}\mathrm{C}$ and covered with a Petri dish. After $2\ \mathrm{min}$, the substrate coated with the $\sim 20\ \mathrm{nm}$ thick PMMA film was stored.

NANO TRANSFER MOLDING

Just before transfer molding, the mold was released from the master and cut to $8 \times 8\ \mathrm{mm}^2$. Both the mold and substrate were cleaned by oxygen plasma (Harrick plasma) at $30\ \mathrm{W}$ for $2\ \mathrm{min}$. The thickness of the PMMA film on the $SrTiO_3$ substrate had reduced to $\sim 6\ \mathrm{nm}$ after this step. The mold was then placed on a flat puck which was placed inside the spin coater and held by vacuum. Prior to actual spin coating, the mold was exposed to a pulse of N_2 gas, $30\ \mu\mathrm{l}$ of the precursor solution was added to the mold, and complete wetting of the mold was confirmed. Spin coating was then initiated according to the program of Table 2.1 where the acceleration was $27.5\ \mathrm{revolutions\ s}^{-2}$ between each step. After spin coating, the mold was observed by optical microscopy to confirm formation of a smooth film without significant contamination. Directly after this step, the mold was placed onto the substrate and carefully pressed to ensure complete adhesion. The assembly was then transferred to a pre-heated hot stage at $80\,^{\circ}\mathrm{C}$ and left there for $45\ \mathrm{min}$ to allow the pattern to cure. The mold was released from the substrate and proper transfer was confirmed by optical microscopy and atomic force microscopy (AFM).

Table 2.1: Program used for spin coating a solution on a mold during transfer molding.

t (s)	15	5	180	15
ν (revolutions min^{-1})	500	1000	5000	500

Prior to thermal annealing the patterns, the samples were cleaned by repeated dipping in a water bath for $10\ \mathrm{s}$, followed by dipping in ethanol and drying in a stream of N_2. The adhesive strength between the patterns and the substrates was found to depend on the humidity of the environment during patterning, where a high humidity was favorable for stronger adhesion. The patterns were then annealed in a pre-heated microwave furnace (Microsynth, Milestone Srl) at $750\,^{\circ}\mathrm{C}$ for $15\ \mathrm{min}$.

MICRO MOLDING IN CAPILLARIES

Just before patterning by MiMiC, the desired micropatterned mold was cut into sizes of $10 \times 10\ \mathrm{mm}^2$ and cleaned by ultrasonication in ethanol for $5\ \mathrm{min}$. The mold was then dried in a stream of N_2 and stored in a Petri dish. A microscope slide (Thermo Scientific) was cleaned on a hot plate at $250\,^{\circ}\mathrm{C}$ with a jet of supercritical CO_2. Together with the substrate, the glass plate was subsequently cleaned by oxygen plasma at $30\ \mathrm{W}$ for $2\ \mathrm{min}$. The mold was placed on the microscope slide, carefully pressed to ensure full adhesion and directly pulled off. The substrate was then placed on the other side of the microscope slide and the mold was placed on the substrate and carefully pressed. Using a pipette, $30\ \mu\mathrm{l}$ of the precursor solution was placed just in front of the mold, after which initial filling of the channels was confirmed by optical microscopy. MiMiC was continued in the middle of a closed Petri dish containing a few droplets of ethanol at the sides. After $60\ \mathrm{min}$, the microscopy slide was transferred to a home made molding machine and a pressure of $\sim 1\ \mathrm{bar}$ was applied on the mold and substrate to guarantee proper contact between the two. Maintaining the pressure, the sample was heated from room temperature to $60\,^{\circ}\mathrm{C}$, without allowing the temperature to overshoot. The assembly was released from the molding machine after $2\ \mathrm{h}$, the mold was removed from the substrate and proper transfer of the pattern was confirmed by optical microscopy. The sample was then annealed in the microwave furnace under the conditions given in Table 2.2.

Table 2.2: Temperature program used to anneal the patterns made by MiMiC.

t (min)	15	15	9	30
T (°C)	400	400	620	620

Before PLD, the samples were cleaned by repeated dipping in a bath of 0.0004% w/w hydrochloric acid. Samples made by transfer molding were dipped into the solution for 5 s and samples made by MiMiC were cleaned for 30 s. Directly after this step, the samples were quickly immersed in a beaker containing water (to stop the slow dissolution of ZnO by the acid), then in a beaker containing ethanol, and were then dried in a jet of N_2.

$La_{0.67}Sr_{0.33}MnO_3$ was deposited on the samples patterned by transfer molding. Depositions were carried out in an O_2 environment of 0.27 mbar. The temperature of the samples during depositions was controlled by a thermocouple inside the heater, which was set at $750\,^{\circ}\mathrm{C}$. The laser beam was produced by a 248 nm KrF excimer laser (LPXPro™ from Coherent, Inc.) with a typical pulse duration of 20 to 30 ns, operated at 21.5 kV. A square mask of $99\ \mathrm{mm}^2$ was used to select the most homogeneous part of the laser beam. The laser was then focused on the stoichiometric $La_{0.67}Sr_{0.33}MnO_3$ target (Praxair electronics) with a spot size of $2.3\ \mathrm{mm}^2$. Laser fluence was controlled with a variable attenuator at $2.0\ \mathrm{J\,cm^{-2}}$. For all depositions, target and sample were directly facing each other at a distance of 5 cm. The target was pre-ablated at 5 Hz for 2 min to remove possible surface contaminations. Depositions were performed at 1 Hz and deposition times were varied to yield a layer thickness of 26 monolayers. Growth was monitored *in situ* by reflection high energy electron diffraction (RHEED), allowing the determination of growth rate on a unit cell level and studying growth dynamics. After deposition, the PLD chamber was filled with O_2 to 100 mbar and the heater power was turned off to allow cooling to room temperature.

$SrRuO_3$ was deposited on the samples patterned by MiMiC. Depositions were performed in an O_2 environment of 0.08 mbar at a heater temperature of $700\,^{\circ}\mathrm{C}$. An image of a square mask with rounded corners ($56\ \mathrm{mm}^2$) with a size of $1.8\ \mathrm{mm}^2$ was produced on the stoichiometric $SrRuO_3$ target (Praxair electronics). A variable attenuator was used to adjust the laser fluence to $2.1\ \mathrm{J\,cm^{-2}}$ on the target. The target was pre-ablated at 5 Hz for 6 min and depositions were carried out at 2 Hz for 30 min (corresponding to a final layer thickness of $\sim$ 50 nm). After deposition, the samples were allowed to cool to room temperature at a maximum rate of $20\ ^{\circ}\mathrm{C\,min^{-1}}$ in an environment of 100 mbar O_2.

The patterns of ZnO were removed by ultrasonication in an aqueous solution of 0.04% w/w hydrochloric acid for $5\ \mathrm{min}$. Ultrasonication was repeated twice in water and once in ethanol, all for $2\ \mathrm{min}$. The sample was then dipped in ethanol and dried on lens paper (LENSX 90 from Berkshire).

Analysis and characterization

The topography of the samples was analyzed with a Dimension Icon atomic force microscope (Bruker AXS) using the standard tapping mode (TM) option. A selected sample was further studied using the tunneling AFM (TUNA) option. The data were processed using Gwyddion 2.30, and some images were additionally analyzed by ImageJ 1.46r. The height images from the samples made by transfer molding are visualized with the adaptive nonlinear color mapping option, whereas the samples made by MiMiC are visualized with a linear color range. ImageJ was used to determine the relative coverage of the patterns, which was used as input for calculation of the magnetic moment per cation.

Crystallographic information was obtained with an X'Pert PRO MRD (PANalytical) using the parallel beam mirror, monochromator and PIXcel 3D detector modules. The polar and in-plane miscut angles of the substrates were determined from the $\omega-$offsets of the (202) and (022) diffraction planes and corresponding optical planes. Further crystallographic information was obtained by electron backscatter diffraction (EBSD) performed on a Merlin field emission microscope (Zeiss), equipped with an in-lens secondary electron (SE) detector, a high efficiency secondary electron (HE-SE2) detector, an energy selective backscattered (EsB) detector, and an angle selective backscattered (AsB) detector (NordlysNano from Oxford Instruments).

Magnetization measurements were conducted on a vibrating sample magnetometer (VSM) installed on a physical properties measurement system (PPMS by Quantum Design). The magnetic moments were determined as a function of the magnetic field and temperature, where the applied field and measured magnetization were along the same direction. Most samples were cut with a wafering blade (Isomet, Buehler) in order to fit into the pick-up coil for measurements in the out-of-plane and $[110]$ directions. For selected samples, the temperature dependence of the saturation magnetization was determined and fitted to the Brillouin functions from Weiss theory of ferromagnetism assuming no external field and for different total angular momenta (J). Best fits were obtained by iteratively changing Curie temperature (T_C) and absolute saturation magnetization $M_\mathrm{S,abs}$ and determining least squares. T_C and $M_\mathrm{S,abs}$ were then chosen from the best fit. Shifts of the hysteresis loops in H_ext were corrected by measuring a Pd reference sample after every measurement at $300\ \mathrm{K}$. Magnetization was also studied by a modified Sagnac interferometer, which could map the out-of-plane magnetization by making use of the polar magneto-optic Kerr effect (MOKE).[36]

The error bars and deviations used in the entire thesis all represent a confidence of 95% (two times the standard deviation).

2.3 *Sub*-μm LINE PATTERNS OF EPITAXIAL $\mathrm{LA_{0.67}SR_{0.33}MNO_3}$

FABRICATION OF ZnO STENCIL MASKS BY NANO TRANSFER MOLDING

The nano transfer molding process to create stencil masks of ZnO is schematically illustrated in Figure 2.1 on page 9, and is explained in more detail in the experimental section. In brief, complexes of Zn^{2+} with PAA were spin-cast on top of a PDMS mold, then transferred onto a substrate that was pre-coated with a thin layer of PMMA, and decomposed into ZnO during subsequent thermal annealing. Numerous patterns were made on both Si and $\mathrm{SrTiO_3}$, all with high fidelity and reproducibility. Figure 2.2 shows one of the samples at different stages in the patterning process (images of a second sample can be found in the appendix on page 40).

After molding, the samples were analyzed by optical microscopy and by observation of the interference colors from reflected light (Figure 2.2a). Generally, nearly the entire sample was covered with the pattern, even though the experiments were performed without specialized equipment in a lab without conditioning of environmental pollutants or humidity. The samples were washed with water to rinse away all species that were not part of the (cross-linked) PAA-Zn complex (the evolution of the line profiles is shown in Figure 2.2d, and includes results before and after washing). The resulting organometallic lines were typically around $200\ \mathrm{nm}$ high, as is shown by the AFM height image in Figure 2.2b. During annealing, the polymer degraded and ZnO formed, leading to significant shrinkage of the patterns in both vertical and horizontal directions. After annealing, the atomic steps on the substrates were well visible in between the lines

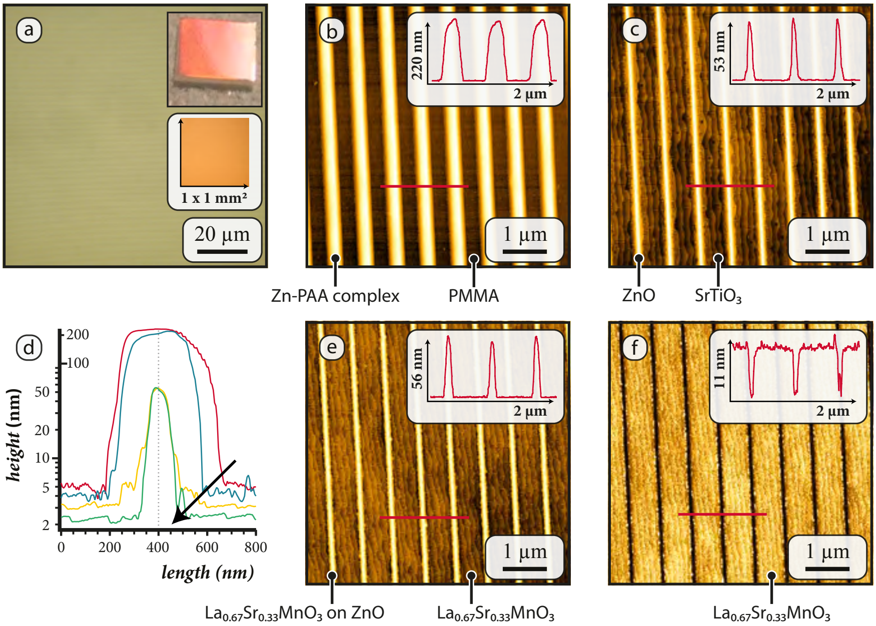

Figure 2.2: (a) Optical microscopy image made directly after transfer molding, together with a photograph of the entire sample (upper inset) and microscopy image made at lower magnification (lower inset). (b,c,e,f) Tapping-mode AFM height images of the same sample during subsequent steps in the patterning process, where the scanning direction was aligned to the principal crystal axis of the substrate. The top two AFM images were obtained (b) before and (c) after thermal treatment (in both cases after subsequent cleaning) of the patterned complex of PAA and Zn^{2+}. The other two images were obtained after PLD of $La_{0.67}Sr_{0.33}MnO_3$, (e) before and (f) after removal of the ZnO mask. The insets in the AFM images show height profiles as measured along the lines in the corresponding AFM images. (d) Additional line profiles of a single line of (precursory) ZnO after different steps in the fabrication process of the stencil mask, for which the four different steps were: patterning, washing, calcination, and pre-etching (these steps are described in the experimental section; the order is indicated by the arrow).

of ZnO, indicating the absence of a residual layer in these regions. The lines had relatively broad bases before reaching a certain height and to reduce the width of these bases, a pre-etching step was introduced in which the samples were exposed to a highly diluted solution of hydrochloric acid, leaving a pattern of ZnO as shown in Figure 2.2c. These patterns were used as stencil masks during subsequent high-temperature depositions of $La_{0.67}Sr_{0.33}MnO_3$. Figure 2.2e shows lines of $La_{0.67}Sr_{0.33}MnO_3$ (having a width of $620\ \mathrm{nm}$ and a spacing of $80\ \mathrm{nm}$) that were obtained after PLD but before dissolution of the ZnO mask. Isolated lines of this material were obtained after removal of the stencil mask, and are displayed in Figure 2.2f.

All substrates were covered with a thin layer of PMMA before patterning, so that the process could be optimized independent of the underlying substrate. This step led to a more universal process that could be carried out on arbitrary substrates, and for the work described in this chapter, allowed optimization of patterning on Si substrates, after which the procedure could be repeated on $SrTiO_3$. The polymeric films were removed during thermal annealing, and results discussed below showed no indications for an influence of this way of removal on subsequent growth of epitaxial films. The presence of trace amounts of organic contaminations can not be excluded though, but may be avoided either by dissolving the polymer directly after molding or by not using the coating at all. Regarding the first option, PMMA can be dissolved in a solvent like acetone (without affecting the organometallic patterns), followed by submerging the samples in ethanol and drying in N_2. Note that this sequence is also used after single termination treatments,[35] and may thus be useful when the uncovered parts of substrates should be perfectly free from organic residues. Patterning was also possible when the use of a coating was omitted, but led to a reduced reproducibility of the molding step on $SrTiO_3$.

The organometallic lines obtained after patterning were uniform in dimensions and shape, but they were generally not perfectly symmetrical as can be seen from the profile in the inset of Figure 2.2b. The observed slight asymmetry may be due to cohesive rupturing of the organometallic lines during removal of the mold, as discussed on page 19. The samples were annealed by rapid thermal annealing, and resulting decomposition and densification led to significant shrinkage, about a factor of four in height and more than a factor of three in width. Also the shape of the patterns changed during thermal treatment, leading to narrow lines ($\mathrm{FWHM} \approx 85\ \mathrm{nm}$) that widened near their valleys, indicating that motion of material at the bottom of the lines was impeded by clamping with the substrates. To obtain a more square-shaped form, samples were shortly immersed in a weakly acidic solution of hydrochloric acid ($\mathrm{pH} = 4.1$), during which the width at the bottom of the lines reduced significantly while the FWHM was barely affected. Note that shrinkage may be controlled by various means, for instance by changing the concentration or contents of the solution, or by using a different mold design.

When the precursor solution was added to the PDMS mold, its channels filled and the concentration of Zn^{2+} increased as a consequence of solvent evaporation and diffusion into the mold. Using the area A of a single channel of arbitrary length l, the initial number of zinc cations in volume Al can be calculated from the concentration of the parent solution. Provided that only fully densified ZnO was left after thermal treatment, the final number of zinc cations in a typical patterned line of length l was determined by integrating the AFM height profile as displayed in the inset of Figure 2.2c. Comparing the two values, almost 15 times the amount of Zn was present in the annealed structures than directly after infiltrating the mold. These calculations strongly indicate that filling of the channels by solution from the outside continued even at an advanced stage of drying, a process that is essential for obtaining structures that are sufficiently high to be used as stencil masks.

Patterns of ZnO could be made without residual layers between the patterned ZnO features, even though no pressure was applied on the mold during curing and also when the washing step before annealing was skipped (this conclusion was made from the visibility of atomic steps after the annealing process). In contrast to this work, soft lithographic patterning is generally associated with residuals, either by transfer of oligomers from the mold[37] or by incomplete expulsion of the fluid.[38] In related work describing an edge printing process, absence of residual layers was observed and explained by a relative large adhesive strength between PDMS and PAA.[39] The complex of PAA and Zn^{2+} is expected to cover the entire sample during patterning, forming a thin layer that protects the sample from interactions with oligomers on the PDMS mold. When the mold is removed this protective layer is removed as well due to a larger adhesive strength with PDMS than with the PMMA film on the substrate. The precursor that is present in the grooves of the mold is more prone to cohesive failure, leading to successful transfer in these regions.

ANALYSIS OF THE EPITAXIAL PATTERNS OF $La_{0.67}Sr_{0.33}MnO_3$

Growth of $La_{0.67}Sr_{0.33}MnO_3$ was monitored by RHEED, with the electron beam aligned parallel to the lines of ZnO and the principal axis of the substrate. Like for growth of continuous thin films of $La_{0.67}Sr_{0.33}MnO_3$ on $SrTiO_3$ and typical for layer by layer growth, the intensity of the specular spot oscillated with deposition time and slowly faded out (Figure 2.3). The period of the oscillations was determined to control the final layer thickness to 26 monolayers (10.0 nm). For some of the depositions the intensity of the specular spot increased during the first few pulses, suggesting that (initial) growth may have been influenced

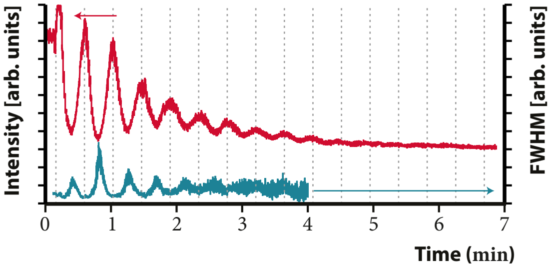

Figure 2.3: Time evolution of the RHEED specular spot intensity and FWHM during the initial stage of growth of $La_{0.67}Sr_{0.33}MnO_3$ on the sample of Figure 2.2. The RHEED pattern was obtained with the electron beam aligned parallel to the principal crystal axis of the $SrTiO_3$ substrate, parallel to the line pattern.

by the presence of the ZnO patterns. Note that the increase in intensity does not necessarily imply that the surface smoothed during this period, since the increase can similarly be explained by the comparatively high structure factors of the deposited material (compared to $SrTiO_3$).

After deposition, the original atomic terraces on the surface of the substrate were replicated on the patterns of $La_{0.67}Sr_{0.33}MnO_3$ and the films were uniform up to the edges of the structures (Figure 2.2e,f). The root mean square (RMS) roughness of a typical line ($0.32\ \mathrm{nm}$) confirmed smooth growth and was only slightly higher than the roughness measured on an unpatterned film that was deposited under the same conditions ($0.20\ \mathrm{nm}$). Epitaxy was confirmed by EBSD (see Figure 2.4), which indicated a single orientation of the patterns even at their edges. Since the Kikuchi patterns of the substrate and deposited material were almost identical, the different materials could not be successfully discriminated, and almost the entire dataset (99.9%) was assigned to $La_{0.67}Sr_{0.33}MnO_3$. The subtle differences of the Kikuchi patterns were recognized though, but incorrectly resolved by a rotation of the $[001]$ direction between in-plane and out-of-plane. The waviness that is mainly observed in the lower parts of the EBSD images is due to drifting of the sample during the measurements.

No detrimental effects of etching the stencil masks were found in the structures of $La_{0.67}Sr_{0.33}MnO_3$, as no significant changes in film topography (roughness) were observed before and after removal of the stencil masks, and characterization discussed below indicated ferromagnetic properties of a well-oriented film of $La_{0.67}Sr_{0.33}MnO_3$. The polycrystalline ZnO stencil masks disintegrates both under acidic and basic conditions, and for this work only highly diluted

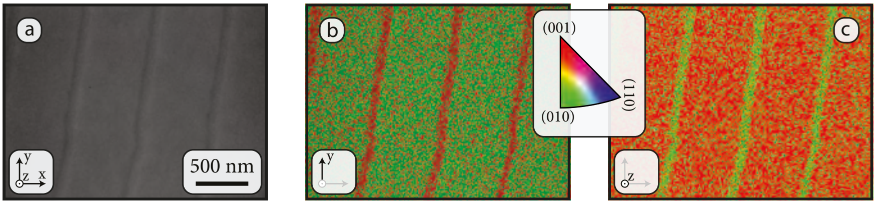

Figure 2.4: EBSD maps of the line pattern of $La_{0.67}Sr_{0.33}MnO_3$, showing the (a) band contrast and (b,c) inverse pole figure maps with respect to (b) an in-plane y direction and (c) the out-of-plane z direction. The Kikuchi patterns were fitted simultaneously to the cubic unit cell of $SrTiO_3$ ($\mathrm{P_{m\bar{3}m}}$; $a_\mathrm{c} = 3.905$ Å), and a tetragonal unit cell ($\mathrm{P_{4/mmm}}$; $a = b = 3.905$ Å, $c = 3.846;$Å) that was assumed for $La_{0.67}Sr_{0.33}MnO_3$.[40] Only the legend for the tetragonal solutions is given in the inset.

solutions of hydrochloric acid were used for etching. In the case of using a solution of $\mathrm{pH} = 4.1$, etch rates were found already to be sufficiently fast, in the order of $\sim 0.5\ \mathrm{nm\ s^{-1}}$.

2.4 MAGNETIC ANISOTROPY IN PATTERNED $\mathrm{LA_{0.67}SR_{0.33}MNO_3}$

Merely considering growth dynamics is not sufficient to conclude about the quality of a film (as defined by Boschker *et al.*[40]), since properties also strongly depend on other factors like oxygen stoichiometry[41] and epitaxial strain.[42] For this reason the effect of patterning was further studied by comparing the ferromagnetic properties of lines of $La_{0.67}Sr_{0.33}MnO_3$ with those measured in a thin film deposited under the same conditions. Magnetic properties were measured primarily to study the influence of patterning on the quality of the epitaxial films, and to illustrate control of anisotropy resulting from the patterns. An external magnetic field was applied in the plane of the film in different directions and for each case magnetization was measured in the same direction as the external field. Magnetic hysteresis loops of the patterned sample at $10\ \mathrm{K}$ and $300\ \mathrm{K}$ are shown in Figure 2.5, and the temperature dependencies of saturation magnetization (M_s), remnant magnetization (M_r) and coercive field (H_c) are also displayed in this figure.

When the field was applied perpendicular to the lines, more slanted curves with lower coercive field and remnant magnetization were obtained as compared to the curves obtained with parallel magnetization. Since VSM measures the bulk magnetic properties, the shapes of these curves reflect the uniformity of the patterns over the complete areas of the samples. Parallel and perpendicular to the lines, saturation magnetization values were comparable near T_C, but started to diverge approximately $80\ \mathrm{K}$ below T_C. Remnant magnetization values and coercive forces were different for parallel and perpendicular alignment over the entire temperature range below T_C, where highest values were obtained for the case of parallel magnetization. The patterns of $La_{0.67}Sr_{0.33}MnO_3$ had an absolute saturation magnetization of $M_{0,s} = 3.1\ \mu_B$/Mn and a Curie temperature of approximately $T_C = 331$ K. Note that the calculated value of magnetization per Mn is not as accurate as that for unpatterned films, since calculations are based on topographical information (Figure 2.2f) to determine the coverage of the lines of $La_{0.67}Sr_{0.33}MnO_3$ (alternatively, the coverage of the lines of ZnO can be determined from Figure 2.2c to estimate the amount of $La_{0.67}Sr_{0.33}MnO_3$, yielding $M_{0,s} = 3.5\ \mu_B$/Mn).

Introduction of the different sources of anisotropy

Magnetic anisotropy in epitaxial thin films of $La_{0.67}Sr_{0.33}MnO_3$ on $SrTiO_3$ was studied previously and was found to be determined by the crystallographic orientation and atomic terrace steps.[43,44] Uniaxial anisotropy from the steps forces the easy axis along the step edges, while biaxial anisotropy from the crystal structure forces the magnetization in one of the $[110]_c$ directions. To indicate the direction of the steps, a distinction is made between the $[100]_c$ and $[010]_c$ directions, which are defined as the crystallographic directions making the lowest and highest angle to the direction of the atomic step ledges, respectively. Whether the uniaxial or biaxial component has the upper hand depends on the polar miscut angle of the substrate and temperature: Low (high) temperatures and low (high) miscut angles lead to a relatively stronger biaxial (uniaxial) component.

Because of the epitaxial nature of the patterns of $La_{0.67}Sr_{0.33}MnO_3$, similar contributions of the steps and crystal to the magnetic anisotropy are expected to add up to the magnetostatic anisotropy from the line shapes,[45] as schematically illustrated in Figure 2.6. Magnetostatic anisotropy is developed due to free poles creating a magnetic field in the direction opposite to the direction of magnetization, which value can be calculated for different shapes.[46] A magnetometric demagnetization factor $N_\perp = 0.030$ was calculated, assuming that the lines in this work can be described by rectangular prisms with thickness $a = 10$ nm, length $b = 5\ \text{mm} \approx \infty$ (yielding $N_\parallel = 0$), and width $c = 600$ nm. The corresponding demagnetizing field and magnetostatic self energy are $H_d = 12\ \text{kA m}^{-1}$ and $E_d = 3.3\ \text{kJ m}^{-3}$, respectively,[45,47] for magnetization perpendicular to the lines at 10 K.

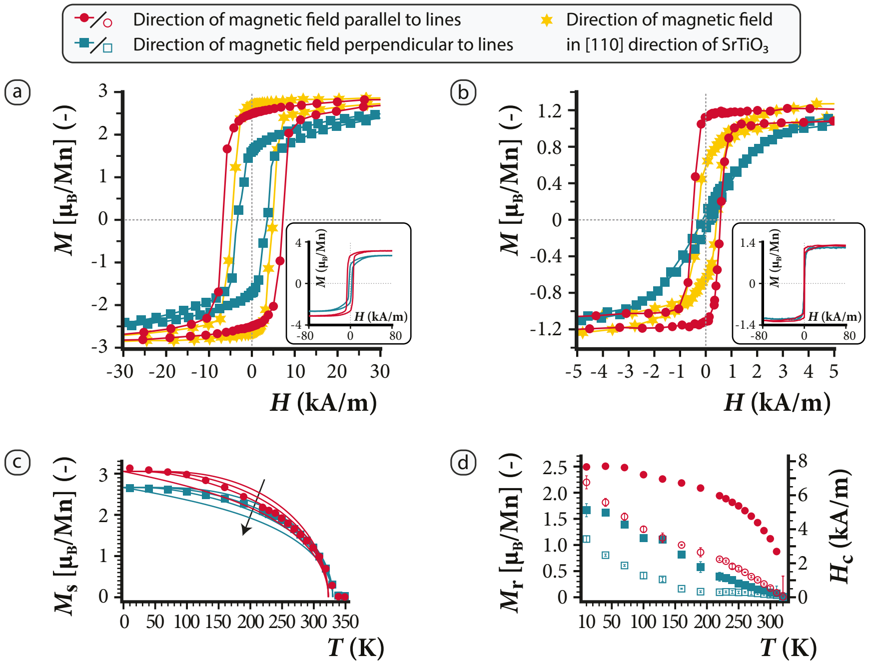

Figure 2.5: Magnetic characterization of the line pattern of Figure 2.2f measured by VSM. Magnetic hysteresis curves at (a) 10 K and (b) 300 K, where the field was applied parallel ($[100]_c$), perpendicular ($[010]_c$) and at 45^o ($[110]_c$) to the lines. (c) Temperature dependence of saturation magnetization, together with fits to a Brillouin functional dependency for different total angular momentum quantum numbers ($J = 1, 2, 4, \infty$ and increases in the direction of the arrow). (d) Remnant magnetization (closed symbols) and coercive field (open symbols) plotted versus temperature.

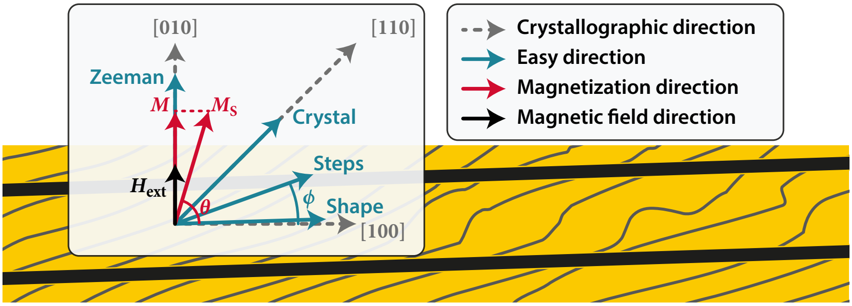

Figure 2.6: Schematic representation of lines of $La_{0.67}Sr_{0.33}MnO_3$ as viewed from the top having the direction of the step ledges about $\phi = 20^o$ to $[100]$. The arrows in the insets indicate the direction of an applied magnetic field (H_{ext}), crystallographic directions, the easy directions from the different sources of anisotropy and the magnetization itself assuming coherent magnetization rotation (Stoner-Wohlfarth mode) and a finite external magnetic field.

The situation of Figure 2.6 is described mathematically by Equation 2.1, which gives the sum of all anisotropy energies. The first term of this equation is the uniaxial magnetostatic anisotropy energy (from the line shapes), and was derived by assuming that the lines were perfectly aligned with the $[100]_\mathrm{c}$ direction. The second term describes the uniaxial part from the atomic terrace steps, and the third term the biaxial crystal anisotropy energy for a purely in-plane magnetized film with the easy axis in one of the $[110]_\mathrm{c}$ directions. The last term (E_Zeeman) is that of the external field energy, for an external field applied orthogonally to the stripes and in the plane of the film. The meaning of all individual symbols can be found in Table 2.4 on page 41. Minimizing E_tot by Equation 2.2, and eliminating θ using the relation between the length of the magnetization vector M_s and the measured magnetization $M = M_\mathrm{s}\ \sin\theta$, gives Equation 2.3, which can be used to calculate the field required to reach a certain magnetization in the $[010]_\mathrm{c}$ direction.

$$
\begin{aligned}
E_\mathrm{tot} = {} & \underbrace{{}^{1}\!/_{2}\,\mu_0 \left(\frac{M_\mathrm{s}}{V}\right)^2 \left(N_\perp\ \sin^2\theta + N_\parallel\ \cos^2\theta\right)}_{E_\mathrm{magnetostatic}} + \underbrace{K_\mathrm{u}\ \sin^2(\theta - \phi)}_{E_\mathrm{steps}} \\
& + \underbrace{K_0 + K_1\ \left(\sin^2(45+\theta)\ \cos^2(45+\theta)\right)}_{E_\mathrm{magnetocrystalline}} - \underbrace{\mu_0\,\frac{M_\mathrm{s}}{V}\,H_\mathrm{ext}\ \sin\theta}_{E_\mathrm{Zeeman}}
\end{aligned}
\tag{2.1}
$$

$$
\begin{aligned}
\frac{dE_\mathrm{tot}}{d\theta} = {} & {}^{1}\!/_{2}\,\mu_0 \left(\frac{M_\mathrm{s}}{V}\right)^2 \ \sin 2\theta\ \left(N_\perp - N_\parallel\right) + K_\mathrm{u}\ \sin(2\theta - 2\phi) \\
& - {}^{1}\!/_{2}\,K_1\ \sin 4\theta - \mu_0\,\frac{M_\mathrm{s}}{V}\,H_\mathrm{ext}\ \cos\theta = 0
\end{aligned}
\tag{2.2}
$$

$$
\begin{aligned}
H_\mathrm{ext} = {} & \underbrace{\frac{M}{V}\ \left(N_\perp - N_\parallel\right)}_{\text{Shape}} + \underbrace{\frac{2K_\mathrm{u}\,V}{\mu_0\,M_\mathrm{s}} \left(\frac{M}{M_\mathrm{s}}\ \cos 2\phi + \frac{({}^{M}\!/_{M_\mathrm{s}})^2 - {}^{1}\!/_{2}}{\sqrt{1 - ({}^{M}\!/_{M_\mathrm{s}})^2}}\ \sin 2\phi\right)}_{\text{Steps}} \\
& + \underbrace{\frac{4K_1\,V}{\mu_0\,M_\mathrm{s}}\,\frac{M}{M_\mathrm{s}} \left(\left(\frac{M}{M_\mathrm{s}}\right)^2 - {}^{1}\!/_{2}\right)}_{\text{Crystal}}
\end{aligned}
\tag{2.3}
$$

Experimental determination of the anisotropy constants and demagnetization factor

To study the influence of the different sources of anisotropy, the problem was simplified by considering an unpatterned thin film of $La_{0.67}Sr_{0.33}MnO_3$, which was deposited under similar conditions as the patterned samples. Analysis and magnetic characterization of this sample can be found in Figure 2.15 (appendix), in which the hysteresis curves were measured in the $[100]_\mathrm{c}$, $[010]_\mathrm{c}$, and $[110]_\mathrm{c}$ directions. The areas between the different magnetization curves equals the work done against the anisotropy energy,[45] and so the demagnetization curves were fitted and integrated from $M = M_\mathrm{s}$ to $M = 0$. The three expressions for the anisotropy energy in Equation 2.4 (as derived from Equation 2.1) were then used to calculate K_u and K_1. Alternatively, values for K_u and K_1 were obtained by fitting the demagnetization curves of the $[010]_\mathrm{c}$ direction with equation 2.3, as displayed in Figure 2.7. The results from both methods can be found in Table 2.3.

$$E_{[100]} = K_u\ \sin^2(\phi) + K_0 + {}^1\!/\!{}_4\ K_1 + {}^1\!/\!{}_2\ \mu_0\ \left(\frac{M_\mathrm{s}}{V}\right)^2\ N_\parallel \tag{2.4a}$$

$$E_{[010]} = K_u\ \sin^2(90 - \phi) + K_0 + {}^1\!/\!{}_4\ K_1 + {}^1\!/\!{}_2\ \mu_0\ \left(\frac{M_\mathrm{s}}{V}\right)^2\ N_\perp \tag{2.4b}$$

$$E_{[110]} = K_u\ \sin^2(45 - \phi) + K_0 + {}^1\!/\!{}_4\ \mu_0\ \left(\frac{M_\mathrm{s}}{V}\right)^2\ (N_\perp + N_\parallel) \tag{2.4c}$$

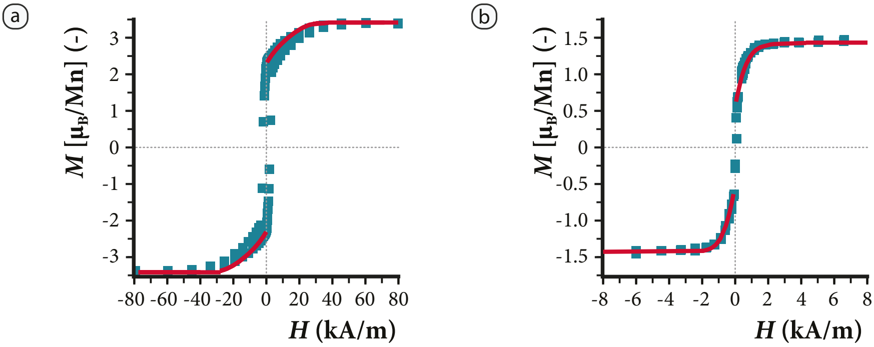

Figure 2.7: Field dependence of magnetization in $[010]$ at (a) 10 K and (b) 300 K together with fits (least squares) to Equation 2.3 for the thin film of $La_{0.67}Sr_{0.33}MnO_3$ (see Figure 2.15).

Table 2.3: K_u and K_1 determined by the area method and by fitting the magnetization curves (value in brackets) of the thin film of $La_{0.67}Sr_{0.33}MnO_3$ (Figure 2.15).

Temperature (K)	K_u (kJ m^{-3})	K_1 (kJ m^{-3})
10	2.2 (1.0)	6.3 (7.2)
300	0.11 (0.12)	−0.02 (0.03)

Like the contribution from atomic steps to anisotropy, the magnetostatic contribution from the line patterns was of uniaxial nature, which hindered easy discrimination between these two effects. To obtain a value for the demagnetization factor, two samples were considered that had similar polar miscut angles but different in-plane miscut angles (ϕ), and the assumption was made that the demagnetization factors and anisotropy constants were equal for the two samples (measured miscut angles can be found in Table 2.5 on page 41). One of these samples was that of Figure 2.2, with the lines running in the $[100]_\mathrm{c}$ direction ($\phi_\mathrm{a} = 5.6^o$), and the other sample had the lines directed in the $[010]_\mathrm{c}$ direction ($\phi_\mathrm{b} = 71^o$), as displayed in Figure 2.14 (appendix).

Two approaches were used to obtain a value for the demagnetization factor: In a first approach, numbers for the shearing of the magnetization curves were obtained by fitting their slopes near $M = 0$, which was done for the two samples measured at $300\ \mathrm{K}$ with the field applied perpendicular to the lines. The problem was then simplified by considering $\phi_\mathrm{a} \approx 0^o$, $\phi_\mathrm{b} \approx 90^o$, and by assuming $K_1 = 0$, since now simple calculus on Equation 2.3 yields that the demagnetization factor is the average of the shearing of the two magnetization curves. Using this approach, $N_\perp - N_\| = 0.013$ was obtained. Alternatively, Equation 2.4a and 2.4b were combined in Equation 2.5, yielding $N_\perp - N_\| = 0.017$ and $K_\mathrm{u} = 78\ \mathrm{J\ m}^{-3}$. The average of these two demagnetization factors is only half of that calculated from the dimensions of the patterns (see page 22). In fact, the demagnetizing factor is better approximated when an elliptic cylinder is assumed,[48] yielding $N_\perp = 0.016$ (for $a = 10\ \mathrm{nm}$, $b = \infty$, and $c = 600\ \mathrm{nm}$).

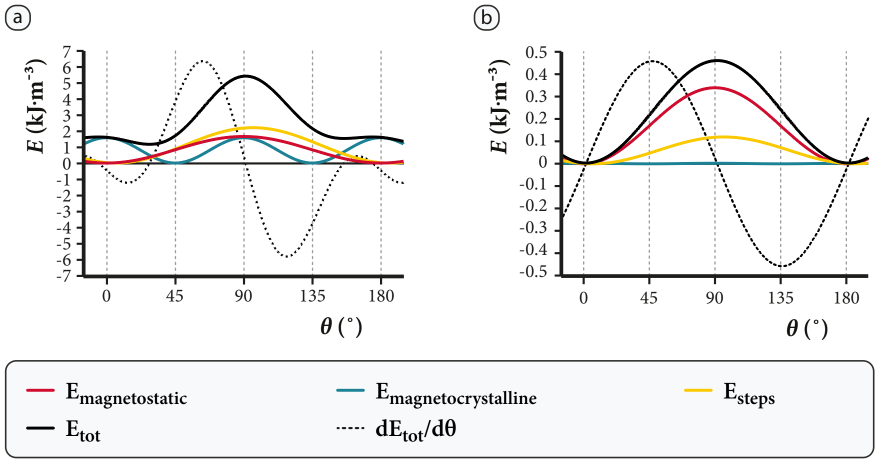

Figure 2.8: Angular dependence of the anisotropy energy at (a) 10 K and (b) 300 K, showing the contribution of the line shapes, lattice, and atomic steps to the anisotropy. For both plots $N_\perp = 0.015$, $N_\parallel = 0$ and $\phi = 6^o$ were used. In (a) $M_s = 2.7\ \mu_B$/Mn, $K_u = 2.2$ kJ m^{-3} and $K_1 = 6.3$ kJ m^{-3} and in (b) $M_s = 1.2\ \mu_B$/Mn, $K_u = 0.12$ kJ m^{-3} and $K_1 = 0.01$ kJ m^{-3}.

$$N_\perp - N_\parallel = 2\,\frac{(E_{010} - E_{100})_\mathrm{b} - \frac{\cos 2\phi_\mathrm{b}}{\cos 2\phi_\mathrm{a}}\,(E_{010} - E_{100})_\mathrm{a}}{\mu_0\,\left(\frac{M_\mathrm{s}}{V}\right)^2\left(1 - \frac{\cos 2\phi_\mathrm{b}}{\cos 2\phi_\mathrm{a}}\right)} \tag{2.5}$$

With the approximations made for the anisotropy constants and demagnetization factor, the angular dependence of the anisotropy energy can be displayed like in Figure 2.8, for $\phi = 6^o$. From this figure, a clear influence of the patterns on the total anisotropy can be seen, both at 10 K and 300 K. At 300 K, the magnetostatic anisotropy is dominant over the other anisotropies, whereas at 10 K all sources of anisotropy have a substantial role. The plots indicate a strong preference for magnetization in the direction of the lines at 300 K, whereas at 10 K a weak preference for magnetization close to the $[110]$ direction is illustrated (in fact the plots indicate that magnetization can easily rotate between $[1\bar{1}0]$, $[100]$, and $[110]$ in this case, since $E_{\text{tot}}(\theta)$ has a nearly flat minimum in this range). These results are in line with the measurements displayed in Figure 2.5, as these measurements indicated that at 300 K, the easy and hard directions were aligned parallel and perpendicular to the lines, respectively; whereas at 10 K a small preference for magnetization in the [110] direction was observed, as compared to magnetization parallel to the lines.

OTHER EFFECTS OF PATTERNING ON THE MAGNETIC BEHAVIOR OF $La_{0.67}Sr_{0.33}MnO_3$

Patterning influenced the magnetic behavior of $La_{0.67}Sr_{0.33}MnO_3$ as anisotropy was clearly observed in the shearing of the hysteresis curves and in the values of the remnant magnetization and coercive field. Despite the clear effects of patterning on ferromagnetic hysteresis, magnetic characterization indicated only a minor influence of patterning on the quality of the films. That is, the absolute saturation magnetization and Curie temperature measured for the epitaxial lines strongly resembled those measured for an unpatterned film (for the thin film, the total angular momentum quantum number $J = 2$, $M_{0,\mathrm{s}} = 3.5\ \mu_B/Mn$ and $T_\mathrm{C} = 334$ K were obtained). These similarities confirm the ability to maintain a high degree of control during film growth while using stencil masks made by nano transfer molding.

Conceptually, patterns cause shearing of the hysteresis curves but do not alter the saturation magnetization of a material, whereas in this work an effect of the patterns on the saturation magnetization at cryogenic temperatures was measured. This effect is also illustrated by the different best fits to the temperature dependence of the saturation magnetization with Brillouin functions, indicating $J_\mathrm{effective} = 4$ and $J_\mathrm{effective} = 2$ for magnetization parallel and perpendicular to the lines, respectively (note that the label $\mathrm{effective}$ is used in this context to distinguish from the actual value for J, which is an intrinsic value that is independent of direction). The reason for the measured differences in saturation magnetization can be understood by considering that the patterns of this work were epitaxially coupled to the single crystalline substrates. Patterning resulted in periodic interruptions of the lattice of $La_{0.67}Sr_{0.33}MnO_3$, leaving altered or dangling bonds at the sides of the lines and leading to local distortions (like strain gradients) in the lattice, changing crystal field interactions and thus the magnetic behavior locally.

2.5 Epitaxial micropatterns of $SrRuO_3$

Fabrication of ZnO stencil masks by MiMiC To illustrate flexibility in terms of size ranges, shapes, and deposited material, soft lithographic molding was used to make stencil masks of various shapes for fabrication of epitaxial microstructures of $SrRuO_3$. As noted in the introduction on page 9, micro molding in capillaries (MiMiC) was used, which is preferable to transfer molding because it requires fewer experimental parameters to be optimized. The process of making the stencil masks is essentially similar to the transfer molding process, except that the channels are filled by capillary action while the mold is attached to the substrate, as schematically shown in Figure 2.1. Note that alternatively, a photolithographic approach can be used to pattern stencil masks of arbitrary shapes with micrometer dimensions,[15–17] but MiMiC offers distinct advantages in that it requires less experimental operations and is far less time consuming than a photolithographic approach.

With MiMiC, two different patterns were made and successfully used to make lines (Figure 2.9) and triangles (Figure 2.10) of $SrRuO_3$ (having lateral dimensions around 4–$7\ \mu\mathrm{m}$, separated by 0.5–$7\ \mu\mathrm{m}$). Both samples were completely covered with the desired patterns as was observed by optical microscopy and by eye looking at the color from interference of reflected light (image a in both figures). The lines were designed such that at one side of the sample twice as many lines were present as compared to the opposite side of the sample. Figure 2.9b shows the ZnO mask at the transition region, where clear differences are seen between the shape of the narrow and broad lines. The broad lines were on average lower than the narrow lines and were clearly highest at the edges. This edge effect was previously observed and explained by preferential wetting and drying at the corners of the PDMS mold.[49] Although the height of the ZnO structures did depend on the exact shape of the mold, no significant variations were measured at different locations on the samples as long as the geometry was the same. Similarly as for the patterns made by transfer molding, calculations indicated that the narrow (broad) lines contained 17 (14) times more material than could be expected from complete filling of the channels with the original solution. Although the patterns will not have reached the bulk density of ZnO, the significant numbers prove that filling and drying occurred simultaneously.

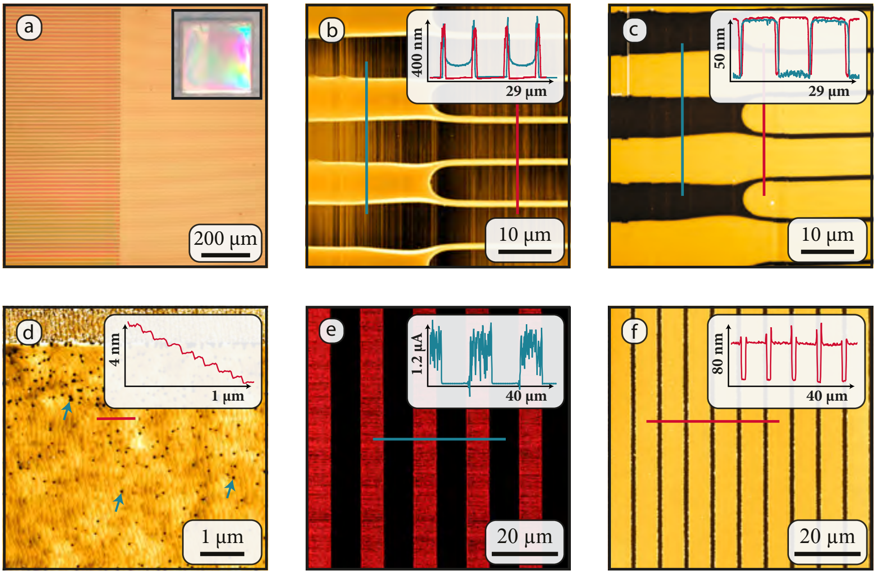

Figure 2.9: Fabrication and characterization of a line pattern of epitaxial SrRuO$_3$ on SrTiO$_3$, prepared by combining MiMiC with PLD. (a) Optical microscopy images made with a $5\times$ objective after MiMiC, showing a photograph in the inset. Tapping mode AFM height images show a sample (b) before, and (c,d) after PLD and subsequent dissolution of the ZnO mask. (e) TUNA image recorded with a sample bias of 1.5 V DC, and (f) topographical information that was measured simultaneously. In this case, only one line was connected to a back electrode (ground) for every two lines. The insets are (b-d,f) height profiles and (e) a current profile, all measured along the lines in the corresponding images.

Analysis of the epitaxial micropatterns of SrRuO$_3$

For the line patterns, the deposition of SrRuO$_3$ was followed with RHEED (Figure 2.11). The observed oscillations were typical for growth of SrRuO$_3$ on SrTiO$_3$ terminated on the TiO$_2$ plane,[50] as was concluded from a nearly doubled width of the first oscillation as compared to subsequent ones. A coherently grown pattern with in-plane lattice constants equal to that of the substrate was confirmed by reciprocal space mapping (Figure 2.12), indicating that epitaxial strain was preserved after removal of the mask. The patterns of SrRuO$_3$ were mostly atomically flat up to the edges, but contained pits that were mainly situated at the atomic step ledges. The pits were concentrated at the edges of the line pattern (Figure 2.9d), while for the triangles pits were predominantly observed near their centers (Figure 2.10d; in both images, three blue arrows are used to indicate three such pits).

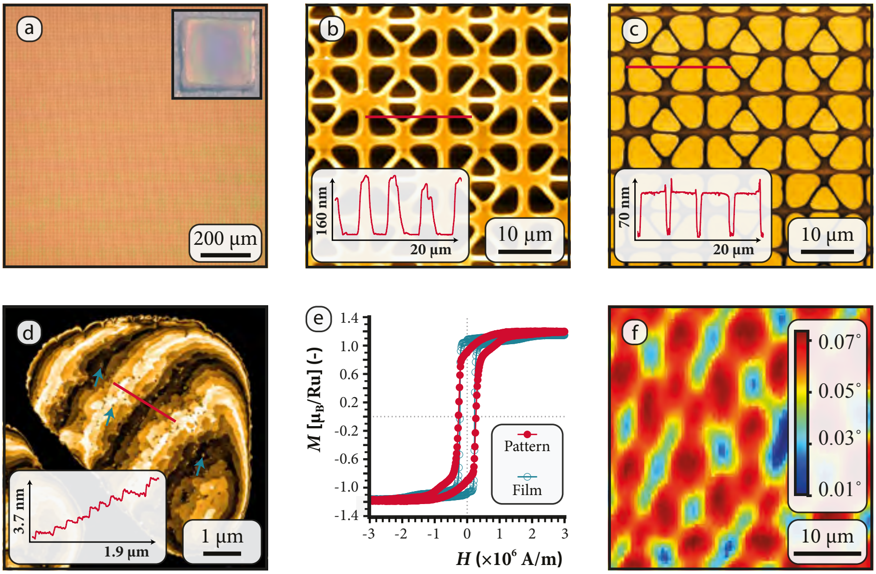

Figure 2.10: A pattern of triangles on $SrTiO_3$ made by MiMiC and followed by deposition of epitaxial $SrRuO_3$. (a) Optical microscopy images of the organometallic pattern and a photograph in the inset. AFM height images (b) before, and (c,d) after PLD and removal of the ZnO mask, together with height profiles in the insets. (e) Magnetic hysteresis loops of this sample and an unpatterned film of $SrRuO_3$, both were measured by VSM at $10\ \mathrm{K}$ with the field applied perpendicular to the surface of the samples. (f) Map scan showing the Kerr signal of the patterned sample, obtained by optical magnetometry at $78\ \mathrm{K}$ after cooling the sample in a field of $0.2\ \mathrm{T}$.

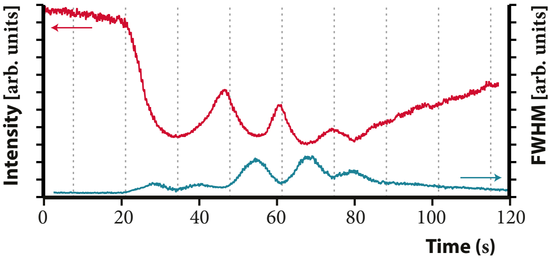

Figure 2.11: Time dependence of the intensity and FWHM of the specular RHEED spot during the initial stage of deposition of $SrRuO_3$ on the sample of Figure 2.9. The RHEED pattern was obtained with the electron beam aligned parallel to the principal crystal axis of $SrTiO_3$, parallel to the line pattern.

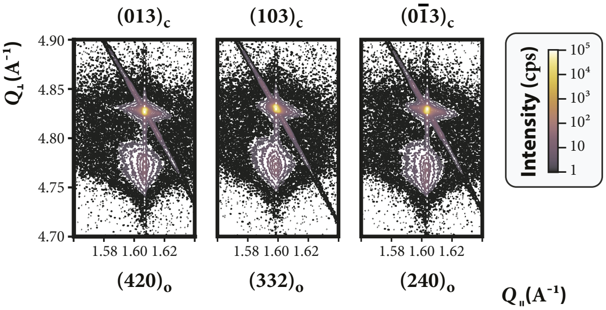

Figure 2.12: Reciprocal space map around the $(013)_\mathrm{C}$ planes of the substrate that was obtained after PLD of $SrRuO_3$ and removal of the stencil mask ($Q = 4\pi \sin\theta/\lambda$). The lattice parameters (distorted orthorhombic) of the film were refined to $a_\mathrm{O} = 5.56$ Å, $b_\mathrm{O} = 5.57$ Å, $c_\mathrm{O} = 7.86$ Å and $\alpha = 90.1^o$, $\beta = 90.0^o$, $\gamma = 89.4^o$.

Growth of $SrRuO_3$ is highly sensitive to the chemistry of the underlying substrate and for a purely TiO_2 terminated substrate, smooth films are expected to grow in a step flow growth mode.[50,51] Pits were observed even in a film made for reference (Figure 2.16b on page 43), which was deposited under the same conditions on a $SrTiO_3$ substrate that was treated to obtain a single TiO_2 termination. The presence of pits even without patterning demonstrates that the pits are not solely the result of the patterning process, although the uneven distribution indicates that there was at least some effect from patterning.

Near the edge of the patterns the surface steps were bending away from the direction of the steps on the substrate, which is most clearly observed for the triangles (Figure 2.10d). Bending of the steps implies that growth was not fully dictated by the underlying substrate and can be explained by considering that step flow growth leads to an unstable situation in confined areas, as is illustrated in Figure 2.13. In a pattern the number of steps can be strongly limited (1) and step advancement (in the direction of the arrow) causes the first (highest) step to grow in lateral dimension (2-3). After a certain time in the deposition process (after deposition of a first monolayer in Figure 2.13), the first step has grown to an extent that not all $SrRuO_3$ will diffuse to the step ledge but will nucleate into islands (4). During advancement of growth, an equilibrium situation is reached where new islands are formed and existing steps and islands will keep advancing (in the direction of the arrow, 5-6). In this discussion any influence of the stencil mask on the adatom sticking coefficient was ignored, but irrespective of this additional complexity the shape of the steps is influenced by confinement.

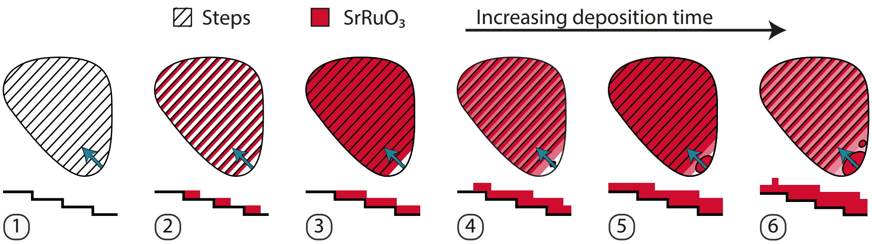

Figure 2.13: Graphical representation used on page 32 to explain the evolution of the atomic terraces during step-flow growth of $SrRuO_3$ while confined by the ZnO stencil mask (conversion of termination is ignored). For every image, a top view and a section across the arrow are given. Every next image corresponds to deposition of half a monolayer of $SrRuO_3$.

Characterization of the epitaxial micropatterns of $SrRuO_3$

The line patterns were characterized by TUNA, imaging tunneling current and topography simultaneously as displayed in Figure 2.9e and f, respectively. The special design of this pattern was used to connect only half of the lines, which is why for every two lines only one showed conductivity. This result proves that the lines were electrically isolated from each other, though it should be noted that it was only the case after post-annealing (the result before post-annealing is not included). Possibly oxygen vacancies were formed near the surface of the substrate during formation of the ZnO stencil mask, rendering the surface of $SrTiO_3$ conductive. By post-annealing the sample in oxygen for $4\ \mathrm{h}$ at $600\ ^{\circ}\mathrm{C}$ after removal of the stencil mask, vacancies were filled and leakage was prevented.

In order to obtain a better understanding of the effects of the used patterning route on the quality of the heteroepitaxial features of $SrRuO_3$, magnetic characterization was performed on the triangular pattern and compared to the case of an unpatterned thin film. Measurements were performed by using a VSM and a scanning optical magnetometer using the polar magneto-optic Kerr effect.[36] The typical shape of the patterns is reflected by the magnetic map in Figure 2.10f, in which the gradual change of the Kerr signal was due to the probe size of the experimental method ($\sim 2\ \mu\mathrm{m}$). The Curie temperature of the sample was determined as $T_{\mathrm{C}} \approx 150\ \mathrm{K}$, which (in line with the diffraction results) points to preservation of epitaxial strain inside the structures.[52] The hysteresis curve that resulted from VSM analysis is shown in Figure 2.10e and was obtained at $10\ \mathrm{K}$ with the field applied out of the surface plane. A hysteresis curve of the unpatterned film is shown as well, for which similar saturation magnetization and coercivity were measured. The most prominent difference between the two curves is the reduction of squareness that is observed for the patterned sample, indicating that extra energy was needed to rotate the magnetization vector out of the surface plane in the case of the patterned sample. The rounding is possibly the result of a local change of the magnetocrystalline anisotropy due to partial relaxation of the stress, either at the imperfections (as indicated by the higher number of pits in the AFM images) or near the edges of the patterns. Additional proof for partial stress relaxation was obtained from X-ray diffraction (see Figure 2.12 as compared to Figure 2.16c on page 43), since broader and more asymmetric film peaks were observed for the patterns than for the unpatterned thin film. The minor differences between the ferromagnetic behavior of the two films, points to near complete preservation of control of thin film growth after using the MiMiC route.

2.6 CONCLUSIONS AND PROSPECTS

Soft lithographic molding techniques were used to make stencil masks of ZnO directly on single crystalline substrates, with which isolated features of epitaxial perovskite oxides were obtained after pulsed laser deposition and lift-off. The bottom-up approach presented in this chapter is more than a supplement to currently available alternatives, as functional structures of $La_{0.67}Sr_{0.33}MnO_3$ and $SrRuO_3$ were made that can neither be fabricated by state-of-the-art shadow masking nor by using self-organized AAO membranes. Micro molding in capillaries (MiMiC) and transfer molding were used complementary to cover both the micrometer and nanometer lateral size range, and both methods allowed fabrication of residue-free patterns of ZnO with high fidelity over the entire area of the substrate. Both molding approaches did not compromise in the control of growth that is generally achieved for unpatterned films, as surface morphology, RHEED patterns, crystal structure, and magnetic properties of patterned and unpatterned films were comparable. Besides, new functionality was added as *e.g.* magnetic anisotropy of the lines of $La_{0.67}Sr_{0.33}MnO_3$ was mainly dictated by the patterns and electrical isolation of the structures was demonstrated for the lines of $SrRuO_3$. Next to these effects acting on the entire structures, signatures of local effects were measured in both materials, which are the result of relaxation and ensuing strain gradients at the surfaces, and may offer unique opportunities to locally engineer strain in epitaxial thin films.

The ZnO structures presented in this chapter may find uses other than as thermally stable sacrificial stencil masks, as all structures made by soft lithographic processes and discussed above were well organized over the complete sample areas and were free from residues. ZnO is a wide bandgap semiconductor (with a bandgap of $3.37\ \mathrm{eV}$) with an exciton binding energy ($60\ \mathrm{meV}$) significantly larger than the thermal energy at room temperature ($26\ \mathrm{meV}$). Interest in this material has mainly been focused on its optical properties, in particular its sharp emission in the near-UV wavelengths for laser applications.[53–55] The conductivity of ZnO is highly sensitive to dopants, adsorbates, interstitials, and oxygen vacancies, making it an interesting candidate for transparent conducting and gas sensing applications.[56–58] At least some of the aforementioned applications may be realized with the methods presented in this chapter.

REFERENCES

[1] A. Ohtomo, D. A. Muller, J. L. Grazul, and H. Y. Hwang. "Artificial charge-modulation in atomic-scale perovskite titanate superlattices". *Nature*, **419** (6905):378–380, 2002.

[2] A. Ohtomo and H. Y. Hwang. "A high-mobility electron gas at the $LaAlO_3/SrTiO_3$ heterointerface". *Nature*, **427** (6973):423–426, 2004.

[3] D. A. Muller, N. Nakagawa, A. Ohtomo, J. L. Grazul, and H. Y. Hwang. "Atomic-scale imaging of nanoengineered oxygen vacancy profiles in $SrTiO_3$". *Nature*, **430** (7000):657–661, 2004.

[4] H. N. Lee, H. M. Christen, M. F. Chisholm, C. M. Rouleau, and D. H. Lowndes. "Strong polarization enhancement in asymmetric three-component ferroelectric superlattices". *Nature*, **433** (7024):395–399, 2005.

[5] A. Stanishevsky, S. Aggarwal, A. S. Prakash, J. Melngailis, and R. Ramesh. "Focused ion-beam patterning of nanoscale ferroelectric capacitors". *J. Vac. Sci. Technol., B*, **16** (6):3899–3902, 1998.

[6] C. S. Ganpule, A. Stanishevsky, Q. Su, S. Aggarwal, J. Melngailis, E. Williams, and R. Ramesh. "Scaling of ferroelectric properties in thin films". *Appl. Phys. Lett.* **75** (3):409–411, 1999.

[7] A. Stanishevsky, B. Nagaraj, J. Melngailis, R. Ramesh, L. Khriachtchev, and E. McDaniel. "Radiation damage and its recovery in focused ion beam fabricated ferroelectric capacitors". *J. Appl. Phys.* **92** (6):3275, 2002.

[8] H. Han, Y. Kim, M. Alexe, D. Hesse, and W. Lee. "Nanostructured ferroelectrics: Fabrication and structure-property relations". *Adv. Mater.* **23** (40):4599–4613, 2011.

[9] P. M. te Riele, G. Rijnders, and D. H. A. Blank. "Ferroelectric devices created by pressure modulated stencil deposition". *Appl. Phys. Lett.* **93** (23):233109, 2008.

[10] C.-V. Cojocaru, R. Nechache, C. Harnagea, A. Pignolet, and F. Rosei. "Nanoscale patterning of functional perovskite-type complex oxides by pulsed laser deposition through a nanostencil". *Appl. Surf. Sci.* **256** (15):4777–4783, 2010.

[11] I. Vrejoiu, A. Morelli, F. Johann, and D. Biggemann. "Ordered 180 ferroelectric domains in epitaxial submicron structures". *Appl. Phys. Lett.* **99** (8):082906, 2011.

[12] W. Lee, H. Han, A. Lotnyk, M. A. Schubert, S. Senz, M. Alexe, D. Hesse, S. Baik, and U. Gösele. "Individually addressable epitaxial ferroelectric nanocapacitor arrays with near $\mathrm{Tb\,inch^{-2}}$ density". *Nat. Nanotechnol.* **3** (7):402–407, 2008.

[13] X. Gao, L. Liu, B. Birajdar, M. Ziese, W. Lee, M. Alexe, and D. Hesse. "High-density periodically ordered magnetic cobalt ferrite nanodot arrays by template-assisted pulsed laser deposition". *Adv. Funct. Mater.* **19** (21):3450–3455, 2009.

[14] X. Lu, Y. Kim, S. Goetze, X. Li, S. Dong, P. Werner, M. Alexe, and D. Hesse. "Magnetoelectric coupling in ordered arrays of multilayered heteroepitaxial $BaTiO_3/CoFe_2O_4$ nanodots". *Nano Lett.* **11** (8):3202–3206, 2011.

[15] N. Banerjee, M. Huijben, G. Koster, and G. Rijnders. "Direct patterning of functional interfaces in oxide heterostructures". *Appl. Phys. Lett.* **100** (4):041601, 2012.

[16] J. Karthik, A. R. Damodaran, and L. W. Martin. "Epitaxial ferroelectric heterostructures fabricated by selective area epitaxy of $SrRuO_3$ using an MgO mask". *Adv. Mater.* **24** (12):1610–1615, 2012.

[17] N. Banerjee, G. Koster, and G. Rijnders. "Submicron patterning of epitaxial $PbZr_{0.52}Ti_{0.48}O_3$ heterostructures". *Appl. Phys. Lett.* **102** (14):142909, 2013.

[18] A. Kumar and G. M. Whitesides. "Features of gold having micrometer to centimeter dimensions can be formed through a combination of stamping with an elastomeric stamp and an alkanethiol "ink" followed by chemical etching". *Appl. Phys. Lett.* **63** (14):2002–2004, 1993.

[19] Y. Xia, E. Kim, X.-M. Zhao, J. A. Rogers, M. Prentiss, and G. M. Whitesides. "Complex optical surfaces formed by replica molding against elastomeric masters". *Science*, **273** (5273):347–349, 1996.

[20] X.-M. Zhao, Y. Xia, and G. M. Whitesides. "Fabrication of three-dimensional microstructures: microtransfer molding". *Adv. Mater.* **8** (10):837–840, 1996.

[21] E. Kim, Y. Xia, and G. M. Whitesides. "Polymer microstructures formed by moulding in capillaries". *Nature*, **376** (6541):581–584, 1995.

[22] Y. Xia and G. M. Whitesides. "Soft lithography". *Angew. Chem., Int. Ed.* **37** (5):550–575, 1998.

[23] J. E. ten Elshof, S. U. Khan, and O. F. Göbel. "Micrometer and nanometer-scale parallel patterning of ceramic and organic-inorganic hybrid materials". *J. Eur. Ceram. Soc.* **30** (7):1555–1577, 2010.

[24] J. M. D. Coey, M. Viret, L. Ranno, and K. Ounadjela. "Electron localization in mixed-valence manganites". *Phys. Rev. Lett.* **75** (21):3910–3913, 1995.

[25] C. B. Eom, R. J. Cava, R. M. Fleming, J. M. Phillips, R. B. Van Dover, J. H. Marshall, J. W. P. Hsu, J. J. Krajewski, and W. F. Peck Jr. "Single-crystal epitaxial thin films of

the isotropic metallic oxides $Sr_{1-x}Ca_xRuO_3$ $(0 \leq x \leq 1)$". *Science*, **258** (5089):1766–1769, 1992.

[26] W. Wu, K. H. Wong, C. L. Choy, and Y. H. Zhang. "Top-interface-controlled fatigue of epitaxial $Pb(Zr_{0.52}Ti_{0.48})O_3$ ferroelectric thin films on $La_{0.7}Sr_{0.3}MnO_3$ electrodes". *Appl. Phys. Lett.* **77** (21):3441–3443, 2000.

[27] C. B. Eom, R. B. Van Dover, J. M. Phillips, D. J. Werder, J. H. Marshall, C. H. Chen, R. J. Cava, R. M. Fleming, and D. K. Fork. "Fabrication and properties of epitaxial ferroelectric heterostructures with ($SrRuO_3$) isotropic metallic oxide electrodes". *Appl. Phys. Lett.* **63** (18):2570–2572, 1993.

[28] L. Pellegrino, M. Biasotti, E. Bellingeri, C. Bernini, A. S. Siri, and D. Marré. "All-oxide crystalline microelectromechanical systems: Bending the functionalities of transition-metal oxide thin films". *Adv. Mater.* **21** (23):2377–2381, 2009.

[29] M. D. Nguyen, H. Nazeer, K. Karakaya, S. V. Pham, R. Steenwelle, M. Dekkers, L. Abelmann, D. H. A. Blank, and G. Rijnders. "Characterization of epitaxial $Pb(Zr,Ti)O_3$ thin films deposited by pulsed laser deposition on silicon cantilevers". *J. Micromech. Microeng.* **20** (8):085022, 2010.

[30] M. W. J. Prins, K.-O. Grosse-Holz, G. Müller, J. F. M. Cillessen, J. B. Giesbers, R. P. Weening, and R. M. Wolf. "A ferroelectric transparent thin-film transistor". *Appl. Phys. Lett.* **68** (25):3650–3652, 1996.

[31] J. H. Park, E. Vescovo, H.-J. Kim, C. Kwon, R. Ramesh, and T. Venkatesan. "Direct evidence for a half-metallic ferromagnet". *Nature*, **392** (6678):794–796, 1998.

[32] M. Bowen, M. Bibes, A. Barthélémy, J.-P. Contour, A. Anane, Y. Lemaître, and A. Fert. "Nearly total spin polarization in $La_{2/3}Sr_{1/3}MnO_3$ from tunneling experiments". *Appl. Phys. Lett.* **82** (2):233–235, 2003.

[33] A. Urushibara, Y. Moritomo, T. Arima, A. Asamitsu, G. Kido, and Y. Tokura. "Insulator-metal transition and giant magnetoresistance in $La_{1-x}Sr_xMnO_3$". *Phys. Rev. B: Condens. Matter Mater. Phys.* **51** (20):14103–14109, 1995.

[34] J. Z. Sun, W. J. Gallagher, P. R. Duncombe, L. Krusin-Elbaum, R. A. Altman, A. Gupta, Y. Lu, G. Q. Gong, and G. Xiao. "Observation of large low-field magnetoresistance in trilayer perpendicular transport devices made using doped manganate perovskites". *Appl. Phys. Lett.* **69** (21):3266–3268, 1996.

[35] G. Koster, B. L. Kropman, G. Rijnders, D. H. A. Blank, and H. Rogalla. "Quasi-ideal strontium titanate crystal surfaces through formation of strontium hydroxide". *Appl. Phys. Lett.* **73** (20):2920–2922, 1998.

[36] J. Xia, P. T. Beyersdorf, M. M. Fejer, and A. Kapitulnik. "Modified Sagnac interferometer for high-sensitivity magneto-optic measurements at cryogenic temperatures". *Appl. Phys. Lett.* **89** (6):062508, 2006.

[37] J. A. Wigenius, M. Hamedi, and O. Inganäs. "Limits to nanopatterning of fluids on surfaces in soft lithography". *Adv. Funct. Mater.* **18** (17):2563–2571, 2008.

[38] O. F. Göbel, M. Nedelcu, and U. Steiner. "Soft lithography of ceramic patterns". *Adv. Funct. Mater.* **17** (7):1131–1136, 2007.

[39] A. George and J. E. ten Elshof. "Sub-50 nm patterning of functional oxides by soft lithographic edge printing". *J. Mater. Chem.* **22** (19):9501–9504, 2012.

[40] H. Boschker, M. Huijben, A. Vailionis, J. Verbeeck, S. Van Aert, M. Luysberg, S. Bals, G. Van Tendeloo, E. P. Houwman, G. Koster, D. H. A. Blank, and G. Rijnders. "Optimized fabrication of high-quality $La_{0.67}Sr_{0.33}MnO_3$ thin films considering all essential characteristics". *J. Phys. D: Appl. Phys.* **44** (20):205001, 2011.

[41] M. Huijben, L. W. Martin, Y.-H. Chu, M. B. Holcomb, P. Yu, G. Rijnders, D. H. A. Blank, and R. Ramesh. "Critical thickness and orbital ordering in ultrathin $La_{0.7}Sr_{0.3}MnO_3$ films". *Phys. Rev. B: Condens. Matter Mater. Phys.* **78** (9), 2008.

[42] M. Izumi, Y. Konishi, T. Nishihara, S. Hayashi, M. Shinohara, M. Kawasaki, and Y. Tokura. "Atomically defined epitaxy and physical properties of strained $La_{0.6}Sr_{0.4}MnO_3$ films". *Appl. Phys. Lett.* **73** (17):2497–2499, 1998.

[43] Z.-H. Wang, G. Cristiani, and H.-U. Habermeier. "Uniaxial magnetic anisotropy and magnetic switching in $La_{0.67}Sr_{0.33}MnO_3$ thin films grown on vicinal $SrTiO_3(100)$". *Appl. Phys. Lett.* **82** (21):3731–3733, 2003.

[44] M. Mathews, F. M. Postma, J. C. Lodder, R. Jansen, G. Rijnders, and D. H. A. Blank. "Step-induced uniaxial magnetic anisotropy of $La_{0.67}Sr_{0.33}MnO_3$ thin films". *Appl. Phys. Lett.* **87** (24):242507, 2005.

[45] B. D. Cullity and C. D. Graham. *Introduction to magnetic materials*. 2nd. John Wiley & Sons, 2009.

[46] A. Aharoni. "Demagnetizing factors for rectangular ferromagnetic prisms". *J. Appl. Phys.* **83** (6):3432–3434, 1998.

[47] S. Chikazumi. *Physics of ferromagnetism*. 2nd. Oxford University Press, 1997.

[48] J. A. Osborn. "Demagnetizing factors of the general ellipsoid". *Phys. Rev.* **67** (11-12):351–357, 1945.

[49] C. R. Martin and I. A. Aksay. "Topographical evolution of lead zirconate titanate (PZT) thin films patterned by micromolding in capillaries". *J. Phys. Chem. B*, **107** (18):4261–4268, 2003.

[50] G. Rijnders, D. H. A. Blank, J. Choi, and C.-B. Eom. "Enhanced surface diffusion through termination conversion during epitaxial $SrRuO_3$ growth". *Appl. Phys. Lett.* **84** (4):505–507, 2004.

[51] R. Bachelet, F. Sánchez, J. Santiso, C. Munuera, C. Ocal, and J. Fontcuberta. "Self-assembly of $SrTiO_3(001)$ chemical-terminations: A route for oxide-nanostructure fabrication by selective growth". *Chem. Mater.* **21** (12):2494–2498, 2009.

[52] Q. Gan, R. A. Rao, C. B. Eom, J. L. Garrett, and M. Lee. "Direct measurement of strain effects on magnetic and electrical properties of epitaxial $SrRuO_3$ thin films". *Appl. Phys. Lett.* **72** (8):978–980, 1998.

[53] R. F. Service. "Will UV lasers beat the blues?" *Science*, **276** (5314):895, 1997.

[54] Y. C. Kong, D. P. Yu, B. Zhang, W. Fang, and S. Q. Feng. "Ultraviolet-emitting ZnO nanowires synthesized by a physical vapor deposition approach". *Appl. Phys. Lett.* **78** (4):407–409, 2001.

[55] M. H. Huang, S. Mao, H. Feick, H. Yan, Y. Wu, H. Kind, E. Weber, R. Russo, and P. Yang. "Room-temperature ultraviolet nanowire nanolasers". *Science*, **292** (5523):1897–1899, 2001.

[56] M. Hiramatsu, K. Imaeda, N. Horio, and M. Nawata. "Transparent conducting ZnO thin films prepared by XeCl excimer laser ablation". *J. Vac. Sci. Technol., A*, **16** (2):669–673, 1998.

[57] J.-H. Lee, K.-H. Ko, and B.-O. Park. "Electrical and optical properties of ZnO transparent conducting films by the sol-gel method". *J. Cryst. Growth*, **247** (1-2):119–125, 2003.

[58] Q. Wan, Q. H. Li, Y. J. Chen, T. H. Wang, X. L. He, J. P. Li, and C. L. Lin. "Fabrication and ethanol sensing characteristics of ZnO nanowire gas sensors". *Appl. Phys. Lett.* **84** (18):3654–3656, 2004.

Lines of $La_{0.67}Sr_{0.33}MnO_3$ running normal to the step edges

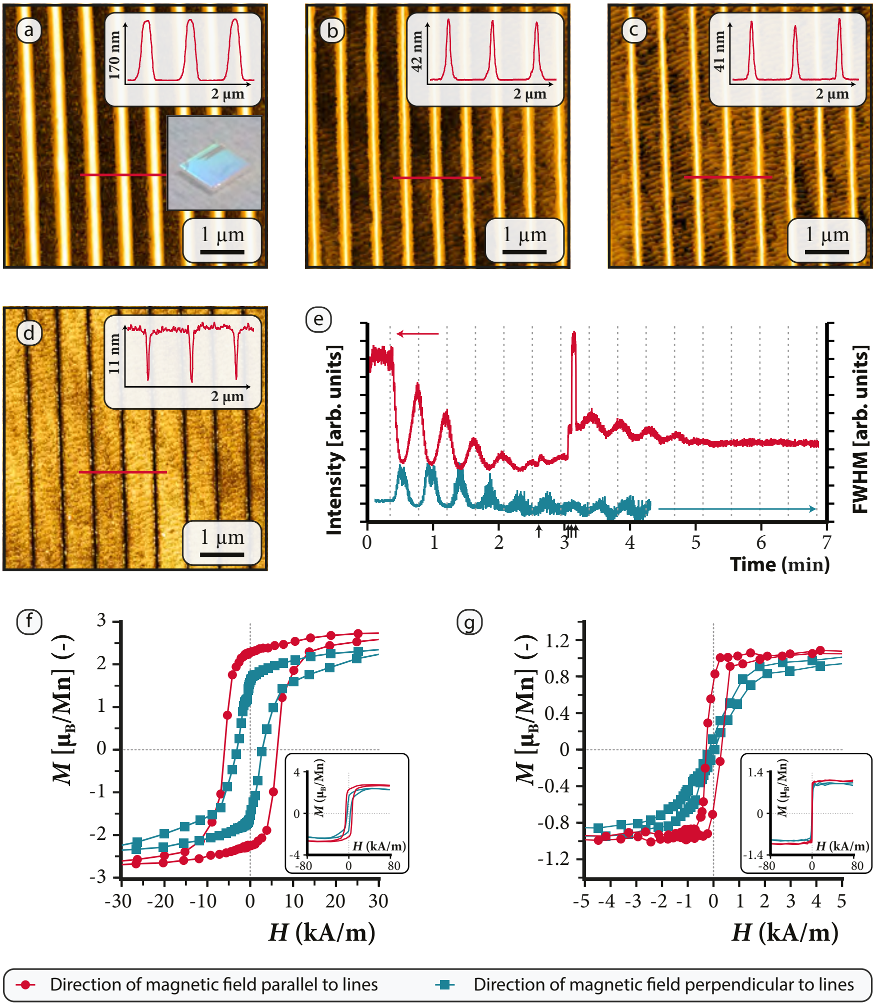

Figure 2.14: Results from a second line pattern of $La_{0.67}Sr_{0.33}MnO_3$, where the lines and atomic step edges ran perpendicular to each other. Tapping-mode AFM height images and height profiles (insets) after (a) transfer molding and water dipping, (b) calcination, (c) pre-etching and (d) PLD and dissolution of the stencil mask. The scanning direction of the AFM was aligned to the principal axis of the substrate. The additional inset in image (a) shows a photograph of the sample after patterning. (e) Time evolution of the RHEED specular spot intensity and FWHM during PLD. The intensity of the electron beam was adjusted at several moments indicated by the arrows on the time axis. Magnetic hysteresis loops measured in-plane in the two principal crystal directions at (f) $10\ \mathrm{K}$ and (g) $300\ \mathrm{K}$ using a VSM.

LIST OF SYMBOLS

Table 2.4: Meaning of the symbols used in the equations.

Symbol	Unit	Meaning
E_{tot}	J m^{-3}	Total anisotropy energy density
N	–	Demagnetization factor; labels $\perp$ and $\parallel$ are used to refer to the factor perpendicular and parallel to the lines, respectively.
μ_0	N A^{-2}	Permeability of vacuum; $4\pi \cdot 10^{-7}$ N A^{-2}
M_{s}	A m^2	Saturation magnetization
V	m^3	Volume of the specimen
θ	^{o}	Angle between [100] and M_{s} (see Figure 2.6)
ϕ	^{o}	Angle between the average direction of the atomic step edges and [100] (see Figure 2.6)
K_{u}	J m^{-3}	Anisotropy constant from atomic terrace steps
K_0	J m^{-3}	Anisotropy constant that is independent of the angle of magnetization; constant for a particular material and temperature
K_1	J m^{-3}	Crystal anisotropy constant; constant for a particular material and temperature
H_{ext}	A m^{-1}	External magnetic field

MISCUTS OF SUBSTRATES USED FOR EPITAXIAL GROWTH OF $LA_{0.67}SR_{0.33}MNO_3$

Table 2.5: Polar miscut (θ) and in-plane miscut (ϕ) of substrates used to prepare different samples of $La_{0.67}Sr_{0.33}MnO_3$.

Sample	Figure	θ (^{o})	ϕ (^{o})
Thin film	2.15	0.08	20
Lines stretched in [100]	2.2	0.16	5.6
Lines stretched in [010]	2.14	0.17	19

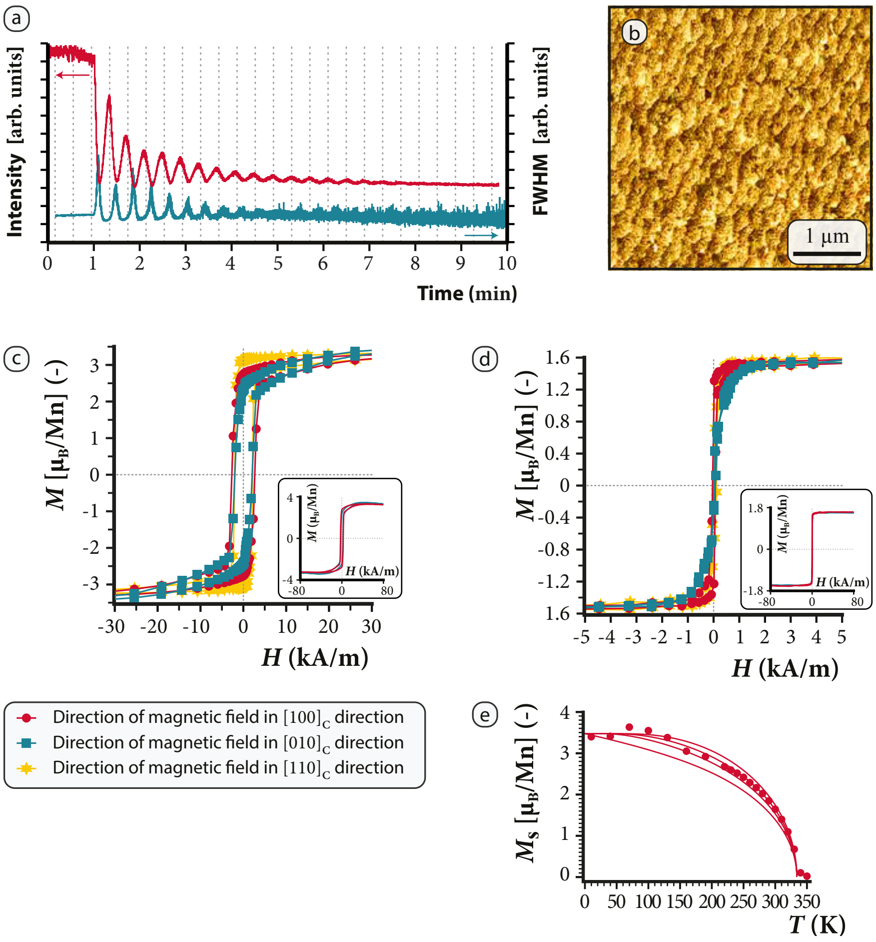

Figure 2.15: Results from a continuous film of $La_{0.67}Sr_{0.33}MnO_3$ showing (a) the RHEED specular spot intensity and FWHM during the initial stage of growth of $La_{0.67}Sr_{0.33}MnO_3$ on $SrTiO_3$ and (b) resulting topography as measured by tapping-mode AFM after deposition (the scanning direction was aligned to the principal crystal axis of the substrate). Magnetic hysteresis curves at (c) $10\ \mathrm{K}$ and (d) $300\ \mathrm{K}$ measured in three different in-plane directions by VSM (the insets show the hysteresis curves in the principal directions over a broader range of applied fields). (e) Temperature dependency of saturation magnetization fitted to Brillouin functions for different total angular momentum quantum numbers ($J = 1, 2, 4, \infty$). The film was deposited under the same conditions as the patterns.

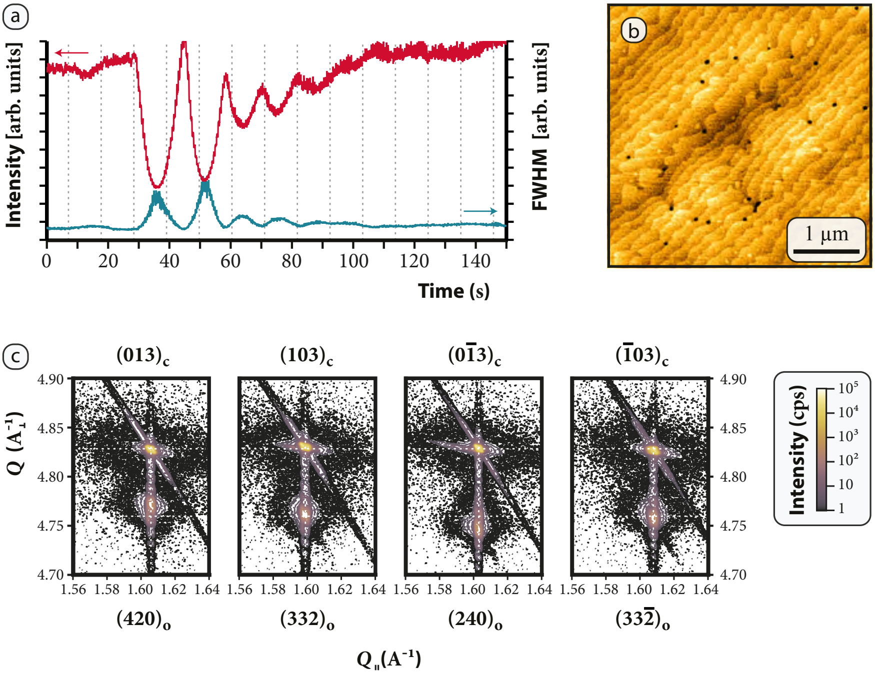

Figure 2.16: (a) *In-situ* analysis of the initial growth of a thin film of SrRuO$_3$ on SrTiO$_3$ monitored with RHEED (the film was deposited under the same conditions as the patterns). *Ex-situ* analysis by (b) AFM and (c) XRD reciprocal space mapping. Note the different peak positions in $Q_\perp$ for the $(420)_\mathrm{O}$ and $(240)_\mathrm{O}$ planes, indicating different values for the a_O and b_O lattice vectors of SrRuO$_3$. The lattice parameters of the film were refined to $a_\mathrm{O} = 5.55$ Å, $b_\mathrm{O} = 5.59$ Å, $c_\mathrm{O} = 7.84$ Å and $\alpha = 90.0^o$, $\beta = 90.0^o$, $\gamma = 89.4^o$.

3

SELF-ORGANIZED NANOSTRUCTURES OF $\mathrm{PBZR}_{0.2}\mathrm{TI}_{0.8}\mathrm{O}_3$

Mixed targets consisting of $PbZr_{0.2}Ti_{0.8}O_3$ and ZnO were used during pulsed laser depositions to form self-organized heteroepitaxial nanostructures. The nanocomposite films that were obtained after depositions on (001) $SrTiO_3$ were exposed to aqueous solutions of hydrochloric acid to selectively remove ZnO and obtain $PbZr_{0.2}Ti_{0.8}O_3$ features with high surface areas. By carefully controlling the deposition conditions, (001) oriented ferroelectric nanopillars were formed with periodicities of approximately $40\ \mathrm{nm}$. Increasing the repetition rate of the laser pulses or the O_2 partial pressure led to reduced lateral sizes of the patterns, accompanied by a change of the morphology from a pillars-and-matrix-like pattern into a maze structure where both phases were meandering through the films. Etching ZnO led to an increase of the tetragonality of $PbZr_{0.2}Ti_{0.8}O_3$, indicating that both phases were coherently coupled and strain was of elastic origin. The electromechanical response of the nanopillars was measured by piezoresponse force microscopy, and was found to increase from $18 \pm 4\ \mathrm{pm\ V^{-1}}$ to $27 \pm 6\ \mathrm{pm\ V^{-1}}$ upon removal of the matrix.

3.1 INTRODUCTION

The previous chapter describes fabrication of (*sub*–)micrometer sized epitaxial structures, which were obtained from stencil masks of ZnO fabricated by soft lithographic routes. Restrictions that are inherent to using soft elastomeric molds limit the aspect ratio (*i.e.* $^{\text{height}}/_{\text{width}}$) of these stencil masks,[1] and as a consequence only planar epitaxial features can be obtained. Applications like catalysis or gas sensing require the functional materials to have high surface areas,[2] and thus ask for other approaches for patterning.

In 2004, Zheng and co-workers reported on PLD of high-aspect ratio (spinel) $CoFe_2O_4$ nanopillars embedded in a (perovskite) $BaTiO_3$ matrix.[3] They illustrated a strong coupling of the electric and magnetic order parameters by the elastic interactions between the two materials. Extensive research followed, focusing on understanding and controlling growth, exploiting combinations of other materials, and utilizing the *semi*-coherency between the two phases.$^{e.g.}$[4–10] As proposed by Macmanus-Driscoll, targeted dissolution of one of the phases leads to nanoporous material,[11] which by its single crystal orientation may have superior properties to current (polycrystalline) alternatives. Nonetheless, apart from a specific example where $BiFeO_3$ was (incompletely) etched in hydrochloric acid (10%) to expose pillars of $CoFe_2O_4$,[12] this concept was never explored.

In this chapter, formation of epitaxial nanostructures of $PbZr_{0.2}Ti_{0.8}O_3$ from composites with ZnO is discussed, as schematically shown in Figure 3.1. ZnO was chosen for its amphoteric nature (as discussed in previous chapter), and because formation of nanocomposites between this material and perovskite $La_{0.7}Sr_{0.3}MnO_3$ was already illustrated.[13,14] Ferroelectric $PbZr_{1-x}Ti_xO_3$ (PZT) was selected for its outstanding piezoelectric properties. Nanostructures of this material may find use in numerous applications, like MEMS or non-volatile memory devices.[15–17]

Using relatively low oxygen partial pressures and laser pulse frequencies, high enough diffusivities of the adatoms were assured while large losses of lead were inhibited, resulting in successful formation of nanopillars of $PbZr_{0.2}Ti_{0.8}O_3$. These nanostructures were found compressively strained by the ZnO matrix and relaxed during etching, leading to a significant increase in their electromechanical responses. The features had periodicities of up to $\sim 40\ \mathrm{nm}$, and upon reducing their lateral sizes, patterns gradually changed from a pillars and ma-

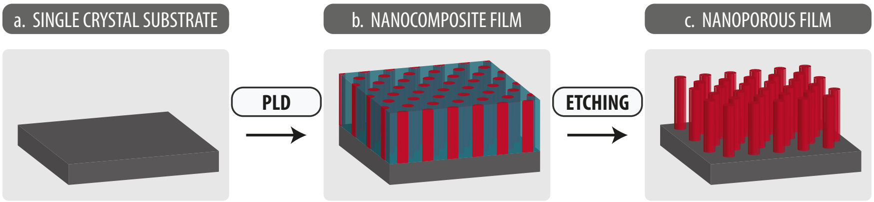

Figure 3.1: Graphical representation of formation of high-aspect ratio heteroepitaxial patterns of $PbZr_{0.2}Ti_{0.8}O_3$ from nanocomposite films. Using PLD, (a) a single crystalline $SrTiO_3$ substrate is covered with (b) a film of $PbZr_{0.2}Ti_{0.8}O_3$ and ZnO from a mixed target. The latter phase is selectively etched with an aqueous solution containing hydrochloric acid, leaving (c) a nanoporous film.

trix form into a maze-like distribution of the phases. The piezoresponse of the nanopillars ($d_{33} = 27 \pm 6\ \mathrm{pm\ V^{-1}}$) fell behind that predicted for a single domain and bulk single crystal of $PbZr_{0.2}Ti_{0.8}O_3$ ($d_{33} = 87\ \mathrm{pm\ V^{-1}}$).[18] Still, the high surface area and epitaxial nature of the nanostructured $PbZr_{0.2}Ti_{0.8}O_3$ presented here may offer distinct advantages over thin film or bulk counterparts, as these nanostructures may find use as piezoelectric transducers,[19] for instance in hydrophones. In addition, the present work may act as model for growth of other perovskite/ZnO composites that can potentially be applied in other fields, like those mentioned at the beginning of this chapter.

3.2 EXPERIMENTAL METHODS

CHEMICALS AND MATERIALS ZrO_2 (99.978%), TiO_2 (99.995%), PbO (99.999%), and ZnO (99.999%), were all from the puratronic class (metals basis), and were supplied by Alfa Aesar. $PbZrO_3$ (99%, trace metals basis) was purchased from Sigma-Aldrich. All other chemicals and materials that were used, were mentioned in section 2.2 on page 11.

FABRICATION OF TARGETS

Using mortar and pestle, PbO, ZrO_2, and TiO_2 were mixed in molar ratios of $1.2 : 0.2 : 0.8$, respectively (the excess of PbO was used to account for lead evaporation during target fabrication and film deposition). The powder (~ 20 g) was subsequently mixed for at least 24 h, using milling balls of yttria-stabilized zirconia (YSZ) in ethanol as milling fluid. The slurry was placed in a drying oven (Memmert) and dried overnight at 70 °C, after which a ceramic pellet was pressed from the powder by uniaxial pressing at ~ 140 bar. The ceramic disk was placed in a Pt container, which was closed with a cap, and heated to $850\,^{\circ}\mathrm{C}$ in a chamber furnace (Carbolite) where it was kept for 2 h (ramp rates were $5\ ^{\circ}\mathrm{C\,min^{-1}}$). Before and after sintering, the pellet was weighted in order to calculate the amount of lead that had evaporated, which was 5%.

The sintered pellet was ground and the appropriate amount of ZnO was added. The powders were mixed, dried and pressed using the same procedure that preceded the formation of $PbZr_{0.2}Ti_{0.8}O_3$. After uniaxial pressing, the pellet was further compressed by an isostatic step at 4000 bar. The disk was then weighted, and placed in an open Pt crucible that was placed in a closed Al_2O_3 crucible (100 ml Coors, purchased from Sigma-Aldrich), containing some $PbZrO_3$ powder to minimize evaporation of lead during thermal annealing. The pellet was sintered at $1150\,^{\circ}\mathrm{C}$ for 2 h (at maximum ramp rates), and weighted to calculate the loss of lead.

Two targets with different ratios between $PbZr_{0.2}Ti_{0.8}O_3$ and ZnO were prepared: One with a volume ratio (PZT:ZnO) of 53:47, and another of 30:70 (bulk densities were assumed to calculate volume ratios). Comparing the mass of a target before and after annealing, and assuming that only PbO had escaped during thermal annealing, loss of atomic lead was estimated. Calculations yielded that the final ratio of $^{\mathrm{Pb}}/_{(\mathrm{Zr+Ti})}$ was 1.11 in target 53:47, and 1.05 in target 30:70 (the lower excess in this target is explained by prolonged thermal annealing of this target that resulted from an error in the temperature controller). XRD analysis was performed on both targets, and all peaks could be assigned either to $PbZr_{0.2}Ti_{0.8}O_3$, PbO, or ZnO.

PULSED LASER DEPOSITION OF NANOCOMPOSITE FILMS

Single crystalline (001) $SrTiO_3$ substrates were TiO_2-terminated by following the treatment of Koster *et al.*[20] A substrate was mounted on a resistive heater using silver glue, and was then brought into the PLD system with a base pressure of 10^{-6} mbar. The chamber was evacuated to at least 10^{-5} mbar, after which a continuous stream of O_2 and Ar in a ratio of $1:9$ was supplied to reach a total pressure of 0.13 mbar. The laser was fired through a square mask of $102\ \mathrm{mm^2}$, and was focused on the target to yield a spot size of $3.0\ \mathrm{mm^2}$. Laser fluence was fixed on the target at $2.5\ \mathrm{J\ cm^{-2}}$ by adjusting the operating voltage of the laser. A thermocouple inside the heater was used to control the temperature at $600\,^{\circ}\mathrm{C}$, where a ramp rate of $10\,^{\circ}\mathrm{C\ min^{-1}}$ was used during heat-up.

Target 30:70 was used for the optimized deposition of nanopillars, which was pre-ablated at $5\ \mathrm{Hz}$ for $6\ \mathrm{min}$ to remove possible surface contaminations. A target to substrate distance of $5\ \mathrm{cm}$ was maintained, and the deposition was carried out at $1\ \mathrm{Hz}$ for $60\ \mathrm{min}$, yielding a layer thickness of $\sim 95\ \mathrm{nm}$. After deposition, the sample was allowed to cool to room temperature at a maximum rate of $20\ \mathrm{^{\circ}C\ min^{-1}}$ in $\sim 100\ \mathrm{mbar}$ O_2.

To reach optimized deposition conditions, the effects of changing substrate temperature, laser repetition rate, composition and pressure of the background gas, and composition of the target were studied. Deviations from the optimized deposition settings are indicated where applicable.

PULSED LASER DEPOSITION OF $SrRuO_3$

$SrRuO_3$ was deposited using the conditions of Kuiper and co-workers,[21] in a $1:1$ O_2 and Ar environment of $0.30\ \mathrm{mbar}$, with the heater at $670\,^{\circ}\mathrm{C}$. A square mask of $56\ \mathrm{mm}^2$ with rounded corners was used to select the most homogeneous part of the laser beam, which was focused on the stoichiometric $SrRuO_3$ target to a spot size of $1.8\ \mathrm{mm}^2$.

The target was pre-ablated at $5\ \mathrm{Hz}$ for $6\ \mathrm{min}$ and depositions were performed at $1\ \mathrm{Hz}$, always with a fluence of $2.1\ \mathrm{J\ cm^{-2}}$ on the target. Depositions were carried out for $60\ \mathrm{min}$, yielding a layer thickness of $\sim 40\ \mathrm{nm}$. Without breaking the vacuum, nanocomposite films were deposited on top of these layers.

ETCHING

Etching of ZnO was typically performed in a $40\ \mathrm{ml}$ aqueous solution of hydrochloric acid ($0.01\ \mathrm{M}$) for $60\ \mathrm{min}$. Samples were subsequently immersed in water for $2\ \mathrm{min}$, rinsed with ethanol, and then dried in a stream of N_2.

ANALYSIS AND CHARACTERIZATION

Crystallographic information was obtained with a D8 Discover diffractometer (Bruker AXS). High resolution scanning electron microscopy (HR-SEM) images were acquired with a Merlin field emission microscope (Zeiss).

In order to investigate the piezo- and ferroelectric properties of partly etched films on $SrRuO_3$, piezoresponse force microscopy (PFM) was performed on a dimension Icon atomic force microscope (Bruker AXS). The samples were

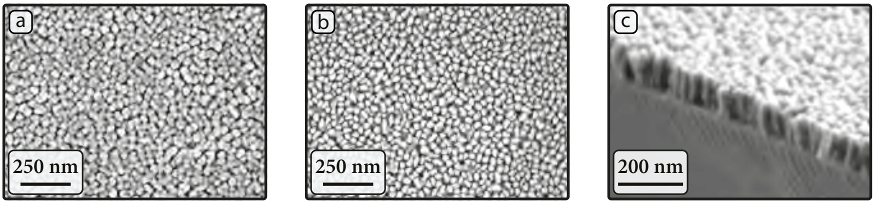

Figure 3.2: InLens HR-SEM images of nanopillars of PZT, (a) before and (b) after etching the ZnO matrix. (c) Cross section of the pillars after etching, obtained with the HE-SE2 detector. The film was deposited on (001) oriented $SrTiO_3$ after deposition of a $SrRuO_3$ bottom electrode.

mounted on metal discs using silver glue, which acted as electric contact to the $SrRuO_3$ bottom electrode. In order to convert the amplitude signal of the microscope (in mV) to mechanical displacement (d_{33}; in $\mathrm{pm\,V^{-1}}$), the system was calibrated by measuring the response of a quartz reference sample with known piezoelectric constant. Piezoresponse was measured by application of an AC bias of $4000\ \mathrm{mV}$ at $50\ \mathrm{kHz}$, while simultaneously a DC bias was swept between -10 and $10\ \mathrm{V}$.

3.3 Epitaxial nanopillars of $PbZr_{0.2}Ti_{0.8}O_3$

Nanocomposites were deposited on a substrate with and without a $SrRuO_3$ bottom electrode, yielding similar morphology as measured by HR-SEM. Figure 3.2 shows images that were measured on the film that was deposited on $SrRuO_3$, both before and after etching. Densely packed nanopillars were imaged before etching, having a rectangular shape and periodicities in the order of $\sim 40\ \mathrm{nm}$ The facets of the rectangular shaped features were running in two direction, possibly aligning with the principal axes of the substrate. The structures had rounded off after etching and appeared separated. Firm conclusions on the extent of separation can not be made though, since the resolution of the cross sectional image in particular, was limited by the non-optimal measuring angle and charging of the nanopillars.

XRD patterns were recorded before and after etching, as shown in Figure 3.3a for the case where no bottom electrode was deposited. Next to the substrate peaks, all diffraction spots could be assigned either to $(00l)$ PZT or (0002) ZnO. The XRD pattern of a film on $SrRuO_3$ was comparable, with the only notable differences that a significantly stronger ZnO $(11\bar{2}0)$ peak was found, and that PZT peaks were largely overshadowed by the stronger peaks of $SrRuO_3$

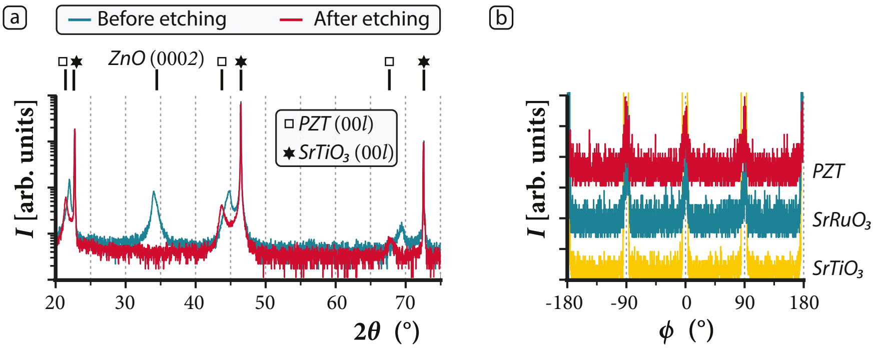

Figure 3.3: (a) XRD $\omega - 2\theta$ patterns of a nanocomposite film deposited on $SrTiO_3$ measured before and after etching, and (b) ϕ-scans measured after etching around the (103) diffraction peaks when a $SrRuO_3$ layer was present as well (for this material the pseudo-cubic crystal notation is used).

(especially before etching). Three clear effects of etching were observed: The PZT $(00l)$ peaks shifted indicating that the out-of-plane lattice parameters increased from $d = 0.404$ nm to $d = 0.413$ nm; the intensities of these peaks subsided; and the peaks of ZnO vanished completely. XRD ϕ-scans displayed in Figure 3.3b, indicated alignment of the $[100]$ axes of the films with that of the substrate. Before etching, very weak twelve fold symmetry was indicated from scanning around the ZnO $(10\bar{1}5)$ plane, indicating that ZnO was twinned with in-plane $[01\bar{1}0]//[110]$ and $[11\bar{2}0]//[110]$ relationships, as schematically displayed in Figure 3.4a. Energy dispersive X-ray spectroscopy (EDX) was performed on the sample before and after etching as well, of which results are summarized in Table 3.1.

Table 3.1: Summary of EDX analysis showing the elemental amounts of lead and zinc relative to that of zirconium, for a nanocomposite film on $SrRuO_3$. For comparison, the expected ratios in the target are displayed as well.

Elements	Before etch	After etch	Target 30:70
Pb : 5×Zr	0.8 ± 0.2	0.6 ± 0.1	1.05
Zn : 5×Zr	4 ± 1	0.09 ± 0.05	6.3

Elemental analysis of the nanocomposite films

Both from XRD and EDX analyses, complete removal of ZnO was indicated after etching. The amount of ZnO in the as-deposited films was lower than that in the target, which was also indicated from the morphology (Figure 3.2) by a relatively high surface area of the nanopillars (image analysis indicated $\sim 60\,\%$ of the total surface area was occupied by pillars). The strong deficiency of ZnO can be explained by the high vapor pressure of metallic Zn, which is even orders of magnitudes higher than that of Pb.[22]

Based on EDX analyses, nanocomposite films were indicated to be lead deficient as well, and further loss of this element was indicated after etching (see Table 3.1; similar trends were found when no bottom electrode was used). Note that ZnO can be doped with Pb,[23] which may also explain the further loss of Pb after etching. Additional hints of partial etching of the PZT features was provided by the rounding of these nanopillars (Figure 3.2b), and reduced XRD intensities after etching (Figure 3.3).

Crystallographic analysis before and after etching

Before and after etching, single diffraction peaks were observed for the PZT pillars, indicating that mainly domains of one kind were present. This indication was further confirmed by reciprocal space mapping around the (003) and (103) peaks (not shown), in which single, broad, spots were found for the PZT phase. After etching, the tetragonality of the PZT pillars increased by out-of-plane lattice expansion to a lattice parameter close to that of c-domains in unstrained $PbZr_{0.2}Ti_{0.8}O_3$. The lattice parameter that was measured for ZnO ($d = 0.527\ \mathrm{nm}$) indicated that the matrix was elongated in the out-of-plane direction. These observations suggest that the pillars were compressively strained by the surrounding ZnO, and *vice versa* that the ZnO matrix was strained tensilely by the PZT pillars.

Lattice matching between the pillars and matrix may have resulted in heteroepitaxial growth between the two phases and build-up of elastic stress, similar as described for the perovskite-spinel nanocomposites.[3] As a result of removal of the matrix phase, stresses were released and the nanopillars could relax by adopting to the most favorable configuration. Possible lattice matching between ZnO and PZT is schematically visualized in Figure 3.4b. Note that

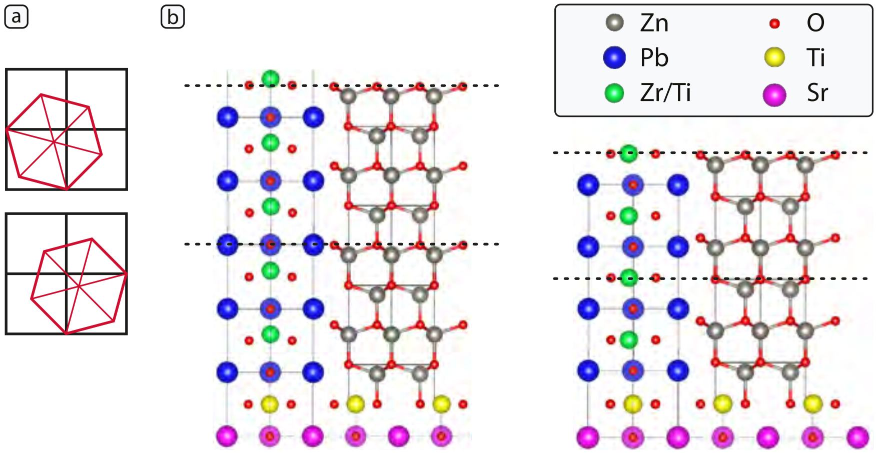

Figure 3.4: Graphical representations of (a) in-plane alignment of hexagonal $(000l)$ oriented ZnO (red) on cubic $(00l)$ oriented $SrTiO_3$ (black), and (b) possible lattice matching between PZT and ZnO. Matching of 5 unit cells of c-domain PZT (001) with 4 unit cells of ZnO (0001) is displayed on the left, and 4 unit cells of a-domain PZT (100) are matched with 3 unit cells of ZnO (0001) on the right (the (110) plane is parallel to the paper).

partial degradation of the pillars by the etchant may have also led to changing lattice parameters, caused by an altered stoichiometry. Milder etching conditions should be used to prevent degradation of the PZT nanostructures and shed more light on the reason behind its out-of-plane lattice expansion, which can either be accomplished by further diluting the acidic etchant or by using basic media to etch ZnO.

3.4 Ferroelectric characterization of the nanopillars

PFM was used to determine the electromechanical response of the nanopillars. In order to study the effects of etching, a partially etched sample was used (Figure 3.5b). Figure 3.5a shows that the material could be switched, since two regions with opposite polarization were successfully written, as indicated by the $\sim 180^o$ phase contrast. Due to their dense packing, nanopillars could not be switched individually though.

Square-shaped hysteresis curves and characteristic butterfly-shaped displacement loops were obtained from the phase and amplitude signals, as displayed in Figure 3.5c and d for a non-etched and etched part of the film, respectively. Comparing the hysteresis curves before and after etching, strong differences

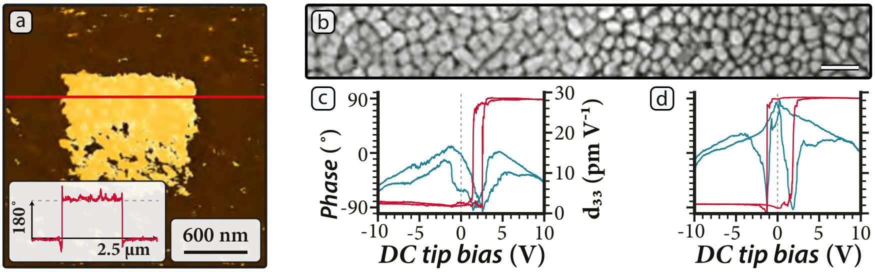

Figure 3.5: (a) PFM phase image of an etched film after writing an area of $2 \times 2\ \mu\mathrm{m}$ with a tip bias of $+10\ \mathrm{V}$, followed by writing an inner area of $1 \times 1\ \mu\mathrm{m}$ with a tip bias of $-10\ \mathrm{V}$. (b) HR-SEM image showing the partially etched sample that was used for the PFM measurements, where the right side was etched and the scale-bar corresponds to $100\ \mathrm{nm}$. (c,d) Representative results from PFM phase and amplitude measurements on (c) the non-etched part and (d) the etched part of the sample. The vertical axes in (d) have the same meaning and values as those in (c).

were observed in terms of their coercivity and imprint. Before etching, loops were found shifted from zero bias to either side, while after etching no imprint was observed and the coercivity had doubled. Electromechanical displacement increased by etching, from $d_{33} = 18 \pm 4\ \mathrm{pm\ V^{-1}}$ (calculated from 8 measurements) to $d_{33} = 27 \pm 6\ \mathrm{pm\ V^{-1}}$ (10 measurements).

Deformations of the nanopillars may have been limited by clamping of their lattices with that of the matrix phase, as this hypothesis explains the lower d_{33} value before etching. In addition, the measured increases of piezoresponses and coercive fields that resulted from etching are explained by the increased tetragonality as measured by XRD.

The facts that imprint was only observed when the matrix phase was still present and hysteresis curves could shift both to the negative and positive side of the bias voltage, lead to the conclusions that this effect was not caused by defects in the nanopillars or strain gradients through the film. A role of the matrix material on imprint is manifest, but the exact cause remains a matter of debate. Charged defects in the matrix may have coupled with the polarization in the nanopillars, causing the observed preferential polarization. Also, ZnO itself is piezoelectric, and its polarization may have coupled with that of the PZT phase. Polarization in ZnO is caused by asymmetry in the oxygen tetrahedra, and its direction will thus depend on the crystallographic orientation of ZnO. Explaining the observed shifts purely by coupling requires that ZnO should have been both (0001) and $(000\bar{1})$ oriented, with a non-homogeneous distribution of these two orientations.

Table 3.2: Summary of EDX analysis showing the elemental amounts of lead and zinc relative to that of zirconium, for a nanocomposite film on $SrTiO_3$ without bottom electrode, deposited at 5 Hz with target 30:70 in an environment of 0.13 mbar O_2 (errors are in the order of ~ 20 %). For comparison, the expected amounts present in the target are displayed as well.

Elements	600 °C	650 °C	700 °C	Target 30:70
Pb : 5×Zr	1.1	0.7	0.05	1.05
Zn : 5×Zr	4.5	4.3	3.8	6.3

3.5 VARIATION AND OPTIMIZATION OF DEPOSITION CONDITIONS

In order to obtain nanopillars of PZT, deposition conditions had to be carefully optimized to guarantee large enough diffusivities while simultaneously prevent considerable off-stoichiometry. Although only one target was used for the work described in the preceding sections, two targets with different PZT:ZnO ratios were used during optimization experiments. Initial experiments were performed with a laser pulse frequency of 5 Hz in an O_2 environment of 0.13 mbar.

OPTIMIZATION OF THE HEATER TEMPERATURE

To promote mobilities of the involved species and allow phase separation over sufficient distances,[6,24] a heater temperature was selected as high as possible. Growth temperatures were strongly limited by the volatility of Pb though, as clearly indicated by the EDX results of Table 3.2. In addition to these results, $ZrTiO_4$ (hhh) diffraction peaks were observed in films deposited at 700 °C, and

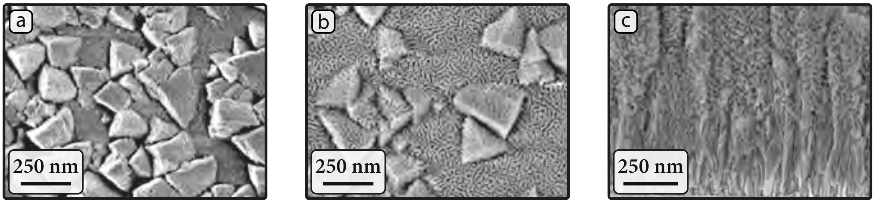

Figure 3.6: InLens HR-SEM images of films deposited with target 53:47 at 5 Hz and 0.13 mbar O_2, (a) after growth and (b,c) after etching (image c is a cross section).

Pb deficiency further increased when the laser pulse frequency was decreased. Besides lead, zinc was also found to be volatile from the EDX studies, which was previously discussed in section 3.3 on page 52. For these reasons, the heater temperature was set at $600\ ^{\circ}\mathrm{C}$ for subsequent depositions.

Using a heater temperature of $600\,^{\circ}\mathrm{C}$ led to inhomogeneous film growth, regardless of which of the two different targets was used. In the case of target 53:47 for instance, pyramidal features were observed that protruded $\sim 100\ \mathrm{nm}$ from the surface, as displayed in Figure 3.6a. XRD patterns obtained from such films showed peaks that could be assigned to (111) oriented PZT, thus indicating that the epitaxial relation with the substrate was lost. Either plane of PZT that is not belonging to the $\{100\}_{\mathrm{pc}}$ family of planes, has a comparatively high surface energy.[25,26] The protruding features of Figure 3.6a may thus have had orientations different from the preferred (001) orientation,[27] and their pyramidal shapes are explained by faceting along the low energy $\{100\}_{\mathrm{pc}}$ planes.

No matrix or pillar phase could be discriminated in these films, but instead a surface structure resulted that closely resembled that of systems formed by spinodal decomposition. Typical meandering features had periodicities of less than $25\ \mathrm{nm}$, and became particularly well visible after etching (Figure 3.6b). A cross section obtained after etching showed that the porous structure consisted of two different regions: A bottom part that showed vertically oriented structures, and a top part that showed tilted structures. This observation indicates that PZT started growing in the (001) orientation, but could not fully maintain this orientation when growth proceeded.

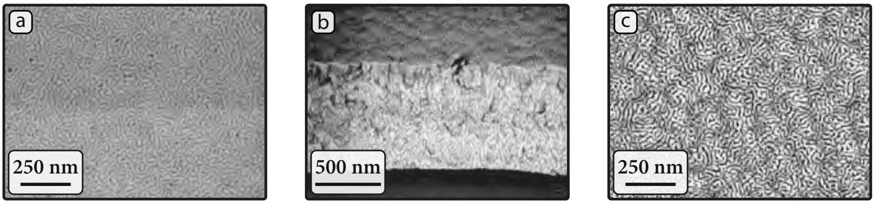

Figure 3.7: HR-SEM images of a film deposited with target 53:47 at $5\ \mathrm{Hz}$ and $0.090\ \mathrm{mbar}$ O_2, (a,b) after growth as measured with the ESB detector, and (c) after etching as measured with the HE-SE2 detector.

OPTIMIZATION OF THE LASER PULSE FREQUENCY AND DEPOSITION PRESSURE

The observed inhomogeneities and presence of undesired film orientations pointed to a system that was trapped before it could reach a thermodynamically favorable arrangement. To promote diffusivities of the adatoms on the sample and allow them to reorganize into a low energy situation, the oxygen background pressure was decreased. The idea behind this measure was primarily to increase the time required for the adatoms to oxidize, leading to increasing diffusivities before being incorporated into an oxide lattice.

Smooth films resulted from depositions at a reduced pressure of $0.090\ \mathrm{mbar}$ (Figure 3.7), and XRD patterns showed only film peaks of $(00l)$ PZT and $(00l)$ ZnO. A cross sectional SEM image of such a film is shown in Figure 3.7b, and shows that the nanostructures were not well vertically aligned, but perturbed over the thickness of the film. Nearly all ZnO was removed during etching, resulting in a nanoporous film as shown in Figure 3.7c.

Next to increasing the actual diffusion length by lowering the deposition pressure, the diffusion time could be increased by decreasing the pulse frequency of the laser. The effects of both approaches were similar, as was concluded from comparing a sample that was deposited at $5\ \mathrm{Hz}$ and $0.090\ \mathrm{mbar}$ (Figure 3.7), with a sample that was formed at $1\ \mathrm{Hz}$ and $0.130\ \mathrm{mbar}$. An SEM image of the latter sample is displayed in Figure 3.8a, and closely resembled that of Figure 3.7, as also in this case a meandering pattern had formed with periodicities typically below $25\ \mathrm{nm}$.

When both deposition pressure and pulse frequency were kept low, as was the case for the sample displayed in Figure 3.8b, nanocomposites with larger sizes formed (periodicities were typically above $25\ \mathrm{nm}$ in this case). From the surface morphology, this nanocomposite film already bore more resemblance with the nanopillars discussed in section 3.3.

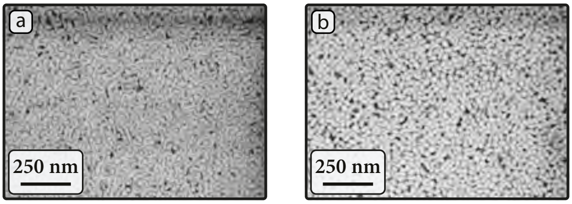

Figure 3.8: HR-SEM images recorded with the ESB detector of films deposited with target 53:47 at $1\ \mathrm{Hz}$ in O_2 environments of (a) $0.130\ \mathrm{mbar}$, and (b) $0.090\ \mathrm{mbar}$.

Because of the significant loss of zinc during the depositions, further reduction of the deposition pressure to 0.013 mbar was only attempted with target 30:70. Though films were still smooth, XRD patterns showed a strongly reduced PZT peak (as compared to the deposition at 0.13 mbar). By increasing the total pressure with Ar this issue was resolved, leading to the results as described in section 3.3 and 3.4. The origin of the effect of adding Ar was not studied, but may be found in altered diagnostics of the plasma, lowered (kinetic) energies of the adatoms that arrived at the sample, or decreased volatilities of the adsorbed species as a result of the increased background pressure.

3.6 CONCLUSIONS

Self-organized nanostructures of $PbZr_{0.2}Ti_{0.8}O_3$ were formed from composite targets containing ZnO, the morphology of which could be controlled by tuning the diffusivities of the adatoms. Increasing oxygen (partial) pressures or laser pulse frequencies led to a gradual change of the self-organized features, from a type where PZT nanopillars existed inside a continuous matrix of ZnO, into a type where both phases meandered through the film. The spinodal-like patterns presumably formed to circumvent excessive build-up of interfacial energies, since the interfacial area is significantly reduced in such a morphology, compared to isolated pillars in a matrix. Formation of these patterns by actual spinodal decomposition is unlikely, since the crystal structures of the two phases are different, and, besides, no solid solution between the two phases was found.

ZnO was removed from the nanocomposite films by wet chemical etching, which led to an increased tetragonality and correspondingly higher piezoresponse of the PZT nanopillars. Nevertheless, the electromechanical response of the pillars was low, which may be related to off-stoichiometry in the films or attack of the PZT features during etching. Milder etching conditions or alkaline etchants should be employed to reduce the detrimental effects of etching, and targets with higher excesses of lead and zinc should be employed to compensate for the losses of these elements during their depositions. The methods described in this chapter may be used to develop porous piezoceramics, and may contribute to the realization of high-aspect ratio epitaxial nanopatterns of other materials, for instance to be used as (gas) sensors, catalysts, or nanoporous electrodes.

REFERENCES

[1] E. Delamarche, H. Schmid, B. Michel, and H. Biebuyck. "Stability of molded polydimethylsiloxane microstructures". *Adv. Mater.* **9** (9):741–746, 1997.

[2] P. M. Rørvik, T. Grande, and M. A. Einarsrud. "One-dimensional nanostructures of ferroelectric perovskites". *Adv. Mater.* **23** (35):4007–4034, 2011.

[3] H. Zheng, J. Wang, S. Lofland, L. Mohaddes-Ardabili, T. Zhao, L. Salamanca-Riba, S. Shinde, S. Ogale, D. Viehland, Y. Jia, D. Schlom, M. Wuttig, A. Roytburd, and R. Ramesh. "Multiferroic $BaTiO_3$-$CoFe_2O_4$ nanostructures". *Science*, **303** (5658):661–663, 2004.

[4] F. Zavaliche, H. Zheng, L. Mohaddes-Ardabili, S. Yang, Q. Zhan, P. Shafer, E. Reilly, R. Chopdekar, Y. Jia, P. Wright, D. Schlom, Y. Suzuki, and R. Ramesh. "Electric field-induced magnetization switching in epitaxial columnar nanostructures". *Nano Lett.* **5** (9):1793–1796, 2005.

[5] H. Zheng, Q. Zhan, F. Zavaliche, M. Sherburne, F. Straub, M. P. Cruz, L. Q. Chen, U. Dahmen, and R. Ramesh. "Controlling self-assembled perovskite-spinel nanostructures". *Nano Lett.* **6** (7):1401–1407, 2006.

[6] H. Zheng, F. Straub, Q. Zhan, P. L. Yang, W. K. Hsieh, F. Zavaliche, Y. H. Chu, U. Dahmen, and R. Ramesh. "Self-assembled growth of $BiFeO_3$-$CoFe_2O_4$ nanostructures". *Adv. Mater.* **18** (20):2747–2752, 2006.

[7] I. Levin, J. Li, J. Slutsker, and A. L. Roytburd. "Design of self-assembled multiferroic nanostructures in epitaxial films". *Adv. Mater.* **18** (15):2044–2047, 2006.

[8] J. Macmanus-Driscoll, P. Zerrer, H. Wang, H. Yang, J. Yoon, A. Fouchet, R. Yu, M. Blamire, and Q. Jia. "Strain control and spontaneous phase ordering in vertical nanocomposite heteroepitaxial thin films". *Nat. Mater.* **7** (4):314–320, 2008.

[9] R. Comes, H. Liu, M. Khokhlov, R. Kasica, J. Lu, and S. A. Wolf. "Directed self-assembly of epitaxial $CoFe_2O_4$ - $BiFeO_3$ multiferroic nanocomposites". *Nano Lett.* **12** (5):2367–2373, 2012.

[10] N. M. Aimon, H. K. Choi, X. Y. Sun, D. H. Kim, and C. A. Ross. "Templated self-assembly of functional oxide nanocomposites". *Adv. Mater.* **26** (19):3063–3067, 2014.

[11] J. Macmanus-Driscoll. "Self-assembled heteroepitaxial oxide nanocomposite thin film structures: Designing interface-induced functionality in electronic materials". *Adv. Funct. Mater.* **20** (13):2035–2045, 2010.

[12] N. Dix, R. Muralidharan, J. Guyonnet, B. Warot-Fonrose, M. Varela, P. Paruch, F. Sanchez, and J. Fontcuberta. "On the strain coupling across vertical interfaces of switchable $BiFeO_3$-$CoFe_2O_4$ multiferroic nanostructures". *Appl. Phys. Lett.* **95** (6):062907, 2009.

[13] B. Kang, H. Wang, J. Macmanus-Driscoll, Y. Li, Q. Jia, I. Mihut, and J. Betts. "Low field magnetotransport properties of $(La_{0.7}Sr_{0.3}MnO_3)_{0.5}$:$(ZnO)_{0.5}$ nanocomposite films". *Appl. Phys. Lett.* **88** (19), 2006.

[14] A. Chen, Z. Bi, C.-F. Tsai, J. Lee, Q. Su, and X. Zhang. "Tunable low-field magnetoresistance in $(La_{0.7}Sr_{0.3}MnO_3)_{0.5}$:$(ZnO)_{0.5}$ self-assembled vertically aligned nanocomposite thin films". *Adv. Funct. Mater.* **21** (13):2423–2429, 2011.

[15] P. Muralt. "Ferroelectric thin films for micro-sensors and actuators: a review". *J. Micromech. Microeng.* **10** (2):136–146, 2000.

[16] S. P. Beeby, M. J. Tudor, and N. M. White. "Energy harvesting vibration sources for microsystems applications". *Meas. Sci. Technol.* **17** (12):R175–R195, 2006.

[17] W. Lee, H. Han, A. Lotnyk, M. A. Schubert, S. Senz, M. Alexe, D. Hesse, S. Baik, and U. Gösele. "Individually addressable epitaxial ferroelectric nanocapacitor arrays with near $\mathrm{Tb\,inch^{-2}}$ density". *Nat. Nanotechnol.* **3** (7):402–407, 2008.

[18] A. R. V. Nagarajan and R. Ramesh. "Nanoscale piezoelectric phenomena in epitaxial PZT thin films". In: *Nanoscale characterisation of ferroelectric materials (scanning probe microscopy approach)*. Ed. by M. Alexe and A. Gruverman. New York: Springer Science & Business Media, 2004. Chap. 6.

[19] A. N. Rybyanets. "Porous piezoceramics: theory, technology, and properties". *IEEE Trans. Ultrason., Ferroelectr., Freq. Control*, **58** (7):1492–1507, 2011.

[20] G. Koster, B. L. Kropman, G. Rijnders, D. H. A. Blank, and H. Rogalla. "Quasi-ideal strontium titanate crystal surfaces through formation of strontium hydroxide". *Appl. Phys. Lett.* **73** (20):2920–2922, 1998.

[21] B. Kuiper, J. L. Blok, H. J. W. Zandvliet, D. H. A. Blank, G. Rijnders, and G. Koster. "Self-organization of $SrRuO_3$ nanowires on ordered oxide surface terminations". *MRS Commun.* **1** (01):17–21, 2011.

[22] "Properties of the Elements and Inorganic Compounds". In: *CRC handbook of chemistry & physics*. Ed. by W. M. Haynes. 95 (Internet Version 2015). Boca Raton, FL.: CRC Press/Taylor and Francis.

[23] L. Schmidt-Mende and J. L. MacManus-Driscoll. "ZnO – nanostructures, defects, and devices". *Mater. Today*, **10** (5):40–48, 2007.

[24] H. Zheng, J. Wang, L. Mohaddes-Ardabili, M. Wuttig, L. Salamanca-Riba, D. Schlom, and R. Ramesh. "Three-dimensional heteroepitaxy in self-assembled $BaTiO_3$- $CoFe_2O_4$ nanostructures". *Appl. Phys. Lett.* **85** (11):2035–2037, 2004.

[25] S. H. Kim, D. Y. Park, H. J. Woo, D. S. Lee, J. Ha, C. Seong Hwang, I. B. Shim, and A. I. Kingon. "Orientation effects in chemical solution derived $Pb(Zr_{0.3},Ti_{0.7})O_3$ thin films on ferroelectric properties". *Thin Solid Films*, **416** (1-2):264–270, 2002.

[26] Y. Z. Chen, T. H. Liu, C. Y. Chen, C. H. Liu, S. Y. Chen, W. W. Wu, Z. L. Wang, J. H. He, Y. H. Chu, and Y. L. Chueh. "Taper $PbZr_{0.2}Ti_{0.8}O_3$ nanowire arrays: From controlled growth by pulsed laser deposition to piezopotential measurements". *ACS Nano*, **6** (3):2826–2832, 2012.

[27] W. Winterbottom. "Equilibrium shape of a small particle in contact with a foreign substrate". *Acta Metall.* **15** (2):303–310, 1967.

4

Locally Controlled Nucleation of Epitaxial Thin Films by Seed Layers of Inorganic Nanosheets

Nanosheets of $Ti_{0.87}O_2$ and $Ca_2Nb_3O_{10}$ were synthesized and transferred onto Si substrates by Langmuir-Blodgett deposition. Using pulsed laser deposition, $SrRuO_3$ films were formed on top of these samples. The underlying nanosheets determined both the morphology and crystallographic orientation of the films. $SrRuO_3$ grew preferentially in the $[110]_{\mathrm{pc}}$ direction on $Ti_{0.87}O_2$ nanosheets, while growth proceeded in the $[001]_{\mathrm{pc}}$ direction on $Ca_2Nb_3O_{10}$ nanosheets. Besides macroscopic control of the out-of-plane crystal direction, single crystal orientations were measured by electron backscatter diffraction on the level of individual nanosheets, indicating that epitaxial growth was achieved on the nanosheets as imposed by their well-defined crystal lattices. The nanosheets also had a clear effect on the magnetic properties of the films, which showed anisotropic behavior only when a seed layer was used. A monolayer consisting of a mixture of both types of nanosheets was made to locally control the nucleation of $SrRuO_3$. In this context, $SrRuO_3$ acted as model material, as it was used to illustrate that nanosheets can be a unique tool to control the orientation of films on a (sub-)micrometer length scale. This concept may pave the way to the deposition of various other functional materials and the fabrication of devices where the properties are controlled locally by the different crystallographic orientations.

4.1 INTRODUCTION

In the previous chapters, examples are found in which a strong correlation between the structure and properties of materials is illustrated. One particular approach to control the properties of a thin film is by changing its crystallographic orientation. For example, Tebano *et al.* showed that for films with thicknesses in the range from 3 to $12\ \mathrm{nm}$, $La_{0.67}Sr_{0.33}MnO_3$ was insulating on (001) oriented $LaAlO_3$ but behaved as a metal on (110) oriented $LaAlO_3$.[1] Also, the magnetization characteristics of several manganites were reported to vary with the orientation of the substrate.[2–4] In the field of ferroelectrics, the ferroelectric activity of a material can be tuned by changing its orientation.[5–8] For instance, the ferroelectric response of epitaxial films of Nd-doped $Bi_4Ti_3O_{12}$ was tuned down to the point were ferroelectricity was completely suppressed by using differently oriented $SrTiO_3$ substrates.[8] A third example of a field where the structure and properties of films were found to vary markedly with the orientation of the substrate is that of nanocomposites made by PLD. These nanocomposite films are generally formed by self-organization processes that take place during the simultaneous deposition of two immiscible phases;[9–12] a concept that underlies the work described in the preceding chapter.

The above examples show that the crystallographic orientation is an important parameter that determines the properties of a film. The reason can be found in geometric constraints defined by the unit cell[5–8] but may also be different. For instance, strain imposed by the substrate,[1–4] or anisotropies in the interfacial, surface, or elastic energies, may play a crucial role.[9–12] In all of the examples, the orientations of the films were completely determined by the lattices of the single crystalline substrates. A versatile method to control the orientation of a film on a smaller scale than the typical dimensions of a substrate has so far not been proposed. If such control will be possible, functional films can be designed where certain position dependent properties are determined by the orientations of the crystallites. Then, an extra degree of freedom will become available for the fabrication of materials with advanced local functionalities.

This chapter describes how different types of nanosheets can be utilized to locally control the nucleation of a film. The concept to use nanosheets for epitaxial growth was first introduced by Kikuta and co-workers in 2007.[13] They showed that the texture of $LaNiO_3$ and $Pb(Zr_{0.3}Ti_{0.7})O_3$ on glass plates could be controlled by the introduction of a seed layer of $Ca_2Nb_3O_{10}$ nanosheets. The films, which were made by chemical solution deposition, showed improved ferroelectric properties compared to films made without the nanosheet layer. Later, Shibata *et al.* used sol-gel processes to deposit textured films of $SrTiO_3$, TiO_2, and ZnO on glass substrates containing monolayers of $Ca_2Nb_3O_{10}$ or MnO_2 nanosheets.[14] Also, PLD was used to form films with certain orientations, even on plastic substrates.[15–17]

In these previous studies, crystalline nanosheets were deposited on amorphous substrates in order to imitate costly single crystal substrates. The, in general, unsurpassed quality of films on single crystal substrates could not be mimicked though, since the films were in-plane randomly oriented. However, as illustrated in this chapter, nanosheets can be a unique tool to control the nucleation of films on a level that can not be attained on single crystal substrates. In brief, the influence of $Ca_2Nb_3O_{10}$ and $Ti_{0.87}O_2$ nanosheets on the nucleation and properties of $SrRuO_3$ is discussed. $SrRuO_3$ is a conductive perovskite, which is ferromagnetic typically below ~ 160 K.[18] The model material was selected mainly because strong magnetic anisotropy is expected.[19–23] PLD was used to grow the films on Si substrates, most of which were pre-coated with a single layer of nanosheets. The morphology and crystallographic orientation of these films are shown to depend on the type of nanosheets that covered the substrates. Epitaxial growth is demonstrated and explained by lattice matching with the underlying nanosheets together with continuation of the oxygen

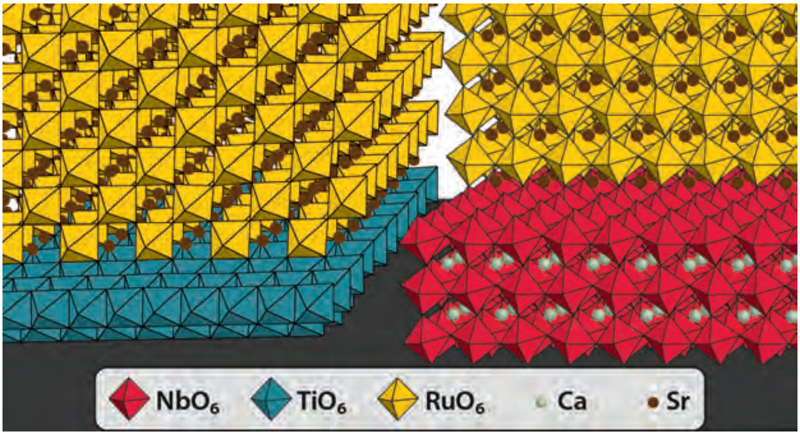

Figure 4.1: Graphical representation of two kinds of nanosheets that are supported on a single substrate to control the orientation of $SrRuO_3$ locally. Note the continuation of the oxygen octahedral rotations.

octahedral backbones, as illustrated in Figure 4.1. Magnetic properties are discussed, and were found to be anisotropic when a layer of nanosheets was present but not when $SrRuO_3$ was directly deposited on a Si substrate. The two types of (sub-)micrometer-sized nanosheets were also combined on a single substrate to locally control the orientation of $SrRuO_3$. This experiment illustrates that nanosheets can be used to create films with position dependent properties that are determined by the local crystallographic orientations.

4.2 EXPERIMENTAL METHODS

MATERIALS Anhydrous K_2CO_3 (purum p.a.; $\geq 99.0\%$) was purchased from Fluka. $CaCO_3$ (A.C.S. reagent, chelometric standard; $\geq 99.95\%$), Nb_2O_5 (trace metals basis; 99.99%), and MoO_3 (A.C.S. reagent; $\geq 99.5\%$) were obtained from Sigma-Aldrich. TiO_2 (technical; $\geq 99\%$) and Li_2CO_3 (purum; $\geq 99\%$) were supplied by Riedel-de Haën. Nitric acid (65% w/w aqueous solution) was purchased from Acros Organics, an ammonium fluoride etching mixture (AF 875-125, PURANAL) from Honeywell, and tetra-*n*-butylammonium hydroxide (TBAOH) (40% w/w aqueous solution) from Alfa Aesar. Because of the serious health hazards associated with handling of the $NH_4F \cdot HF$ mixture, the solution was used only in a fume hood inside a lab with an emergency HEXAFLUORINE washing station while wearing protective gloves, protective clothes and eye protection. All experiments that involved nitric acid were carried out in a fume hood. Ethanol (absolute, $\geq 99.8\%$) and acetone were acquired from Atlas & Assink Chemie and ultrapure water with a resistivity of $18.2\ \mathrm{M\Omega\ cm}$ was used. All chemicals were used as received without further purification.

Single crystal B-doped (100) Si wafers (grown by the Czochralski process) were purchased from Okmetic and single crystalline (001) and (110) $SrTiO_3$ substrates (gown by the Verneuil process) were acquired from CrysTec GmbH. PLD was performed with a stoichiometric polycrystalline target of $SrRuO_3$, which was obtained from Praxair electronics.

PREPARATION OF PRECURSORS

Slightly deviating from the methods described in references [24] and [25], precursor powders were synthesized and exfoliated into unilamellar nanosheets. $KCa_2Nb_3O_{10}$ was prepared by mixing K_2CO_3 (2.81 g), $CaCO_3$ (7.41 g) and Nb_2O_5 (14.76 g) using mortar and pestle and annealing the mixed powders inside a capped alumina crucible (100 ml Coors purchased from Sigma-Aldrich) at 1200 °C, following the heating sequence of Table 4.1. The layered compound was protonated by stirring it at 300 rpm inside a glass screw cap bottle in nitric acid (1.0 L, 5.00 M) for 72 h. The product was recovered by vacuum filtration (using Whatman No. 1450-055 filter paper), washed with a copious quantity of water (at least 6× with 200 ml), and placed inside a petri dish ($\varnothing = 150$ mm) to allow it to dry at room temperature for 48 h.

To prepare $K_{0.8}[Ti_{1.73}Li_{0.27}]O_4$, TiO_2 (10.00 g), K_2CO_3 (16.70 g), Li_2CO_3 (0.722 g), and MoO_3 (13.16 g) were ground in ethanol (35 ml) for 48 h using milling balls of YSZ. The slurry was then placed in a drying oven (Memmert) and kept overnight at 70°C, after which the powder was calcined inside a closed Pt crucible at 1150 °C. Formation of large crystallites of $K_{0.8}[Ti_{1.73}Li_{0.28}]O_4$ was realized under the conditions mentioned in Table 4.1 by formation of a liquid flux of K_2MoO_4. The chunk was placed inside a glass screw cap bottle (500 ml) containing a stirring magnet and after addition of 200 ml water, the bottle was vigorously shaken until the chunk fell apart. The suspension was then stirred at 300 rpm for 90 min, filtered by vacuum filtration (using glass microfiber filter GF8047 from ALBET LabScience), and washed 10× with water to filter out the flux compound. The residue was added to a glass screw cap bottle and protonated in nitric acid (500 mL, 2.00 M) under constant stirring at 300 rpm during 96 h, in the course of which the solution was renewed every 24 h. Similar to the method used to obtain $HCa_2Nb_3O_{10} \cdot 1.5\,H_2O$ (HCNO), $H_{1.07}Ti_{1.73}O_4 \cdot H_2O$ (HTO) was recovered after vacuum filtration and drying.

Table 4.1: Annealing sequences used in a chamber furnace (Carbolite) for solid state synthesis of the parent compounds (a holdback temperature of 20 °C was used).

Powder	Ramp rate $^{\circ}$C min^{-1}	Temperature $^{\circ}$C	Duration h
$KCa_2Nb_3O_{10}$	5	800	4
	0.5	1200	10
	5	25	–
$K_{0.8}[Ti_{1.73}Li_{0.28}]O_4$	3	1150	0.5
	0.1	950	–
	5	25	–

Exfoliation of nanosheets

To obtain $Ca_2Nb_3O_{10}$ nanosheets, 0.4 g of HCNO was suspended in 100 mL water and 480 μL of the $40\,\%$ commercial aqueous solution of TBAOH (exfoliation agent) was added. The $Ti_{0.87}O_2$ nanosheets were formed by adding 0.3 g of HTO and 635 μL exfoliation agent to 200 mL water. Both solutions were shaken vigorously for 1 min after preparation, and were then kept on a rocking shaker (ST3 from Assistent GmbH, Switzerland). To increase stability, the solution containing $Ca_2Nb_3O_{10}$ nanosheets was diluted 9 times after 14 days of exfoliation, and the solution containing $Ti_{0.87}O_2$ nanosheets was diluted 3.3 times after 21 days. Prior to making these stock solutions, the solution containing $Ca_2Nb_3O_{10}$ nanosheets was stirred until all of the precipitate had dispersed in the solution, while the other solution was decanted 30 min after it had been removed from the rocking shaker.

Langmuir-Blodgett deposition

The silicon wafer with native oxide layer was cut into pieces of about $1\times1.5\ \mathrm{cm}^2$. A substrate was first cleaned on a hot plate at $250\,^{\circ}\mathrm{C}$ with a jet of supercritical CO_2 and then in an oxygen plasma cleaner (Harrick plasma) at 30 W for 15 min. Langmuir-Blodgett depositions were carried out in a double-barrier Langmuir trough with a vertical lifting configuration (MiniMicro from KSV NIMA, Finland) under a constant rate of compression ($3.0\ \mathrm{mm\,min^{-1}}$). The development of surface pressure was monitored (Figure 4.2a) and compression was continued until the isotherm leveled off, indicating a dense monolayer film of nanosheets had formed on the surface of the liquid. Especially depending on the kind of nanosheets and age of the stock solution that was used, the required surface pressure for a high coverage was $\Pi \approx 15\ \mathrm{mN\,m^{-1}}$ ($\Pi \approx 20\ \mathrm{mN\,m^{-1}}$) for $Ca_2Nb_3O_{10}$ ($Ti_{0.87}O_2$) nanosheets. By continuous movement of the barriers ($\pm3.0\ \mathrm{mm\,min^{-1}}$), the surface pressure was maintained while the substrate was lifted out of the liquid at a constant rate of $1.0\ \mathrm{mm\,min^{-1}}$, during which the monolayer was transferred to the substrate. AFM height images of resulting samples with a high coverage of $Ca_2Nb_3O_{10}$ and $Ti_{0.87}O_2$ nanosheets are displayed in Figure 4.2b and c, respectively.

Three types of monolayers were deposited on the substrates, *i.e.* $Ti_{0.87}O_2$, $Ca_2Nb_3O_{10}$ and a mixture of both types of nanosheets. $Ti_{0.87}O_2$ nanosheets were deposited after further diluting the stock solution 12.3 times, while the

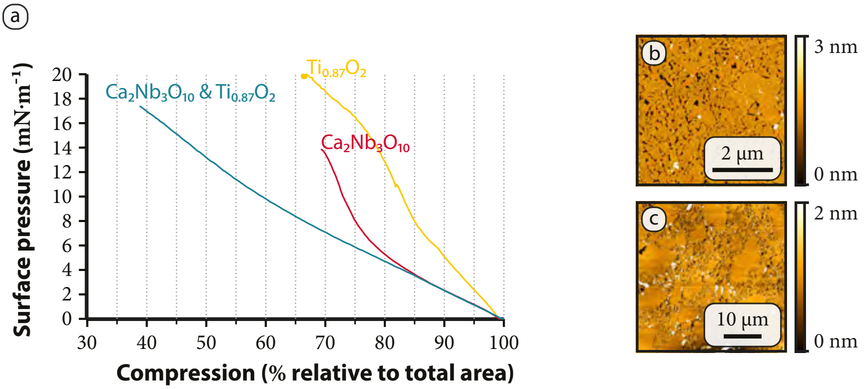

Figure 4.2: (a) Three isotherms that were recorded prior to the deposition of densely packed monolayers of $Ca_2Nb_3O_{10}$, $Ti_{0.87}O_2$ and a combination of the two types of nanosheets. (b,c) TM-AFM images of the resulting monolayers for films of $Ca_2Nb_3O_{10}$ and $Ti_{0.87}O_2$, respectively.

stock solution of $Ca_2Nb_3O_{10}$ was used as prepared. In the case when a mixture of both types of nanosheets was desired, $10\ \mathrm{mL}$ of each stock solutions were mixed with $30\ \mathrm{ml}$ water, and a deposition was performed at $\Pi = 17.5\ \mathrm{mN\ m^{-1}}$.

Pulsed laser deposition of $SrRuO_3$

$SrRuO_3$ films were deposited by pulsed laser deposition using the conditions of Kuiper *et al.*[26], as also described in section 3.2 on page 49. All depositions were carried out for $60\ \mathrm{min}$, yielding a layer thickness of $34 \pm 7\ \mathrm{nm}$.

Analysis and characterization

The topography of the samples was analyzed with a Dimension Icon atomic force microscope (Bruker AXS) using the standard tapping mode option. For selected samples, the relative coverage of nanosheets on the substrates was determined. In these cases, AFM scans were made on at least five different locations on the sample. The data were subsequently processed using Gwyddion (2.29 or higher) and the resulting images were analyzed by ImageJ (1.45s or higher) to obtain a value for the relative coverage of nanosheets.

Crystallographic information was obtained with a D8 Discover diffractometer (Bruker AXS). HR-SEM was performed on a field emission microscope (additional information about the equipment can be found in chapter 2). EBSD was performed using a probe current of $250\ \mathrm{pA}$ and 4×4 binning, and resulting Kikuchi patterns were fit to a cubic unit cell ($\mathrm{P_{m\bar{3}m}}$; $a_\mathrm{c} = 3.928$ Å) using

Aztec 2.0. In addition, an ultra-high vacuum Orion Plus helium ion microscope (Zeiss) equipped with an Everhardt–Thornley detector (to record images based on secondary electrons) was used.

The samples were cut to sizes of $17 \pm 2\ \mathrm{mm}^2$ after which magnetization measurements were conducted on a vibrating sample magnetometer (PPMS by Quantum Design). Magnetic moments were determined as a function of magnetic field and temperature, with the magnetic field applied parallel or perpendicular to the surfaces of the samples.

4.3 INFLUENCES OF NANOSHEETS ON GROWTH OF $\mathrm{SrRuO_3}$

ANALYSIS OF THE MORPHOLOGY OF $\mathrm{SrRuO_3}$ ON NANOSHEETS As can be seen from the TM-AFM images in Figure 4.3, the topography of $SrRuO_3$ was influenced by the underlying nanosheets. On the parts of the substrates that were not covered by nanosheets, larger and more separated grains were found than on the areas that did contain nanosheets. This observation is corroborated by the values for the RMS roughness. For $SrRuO_3$ on $Ca_2Nb_3O_{10}$ nanosheets, $Ti_{0.87}O_2$ nanosheets, and parts free from nanosheets, the RMS roughnesses were $R_\mathrm{q} = 5.8\ \mathrm{nm}$, $4.4\ \mathrm{nm}$, and $11\ \mathrm{nm}$, respectively. These values are significantly larger than those measured for $SrRuO_3$ deposited on single crystalline substrates such as (001) $SrTiO_3$ ($SrRuO_3$ deposited on this substrate using the same conditions had an RMS roughness of $R_\mathrm{q} = 0.24\ \mathrm{nm}$). Note that the AFM images of Figure 4.3 were made on samples with a relative sparse distribution of nanosheets. The reason to show these images is that the different morphologies of $SrRuO_3$ on and off the nanosheets are well visible. Similar film morphologies were obtained on densely packed monolayers of nanosheets (not shown), which were used for all further analysis and characterization.

Marked differences were observed between the morphologies of the films on $Ca_2Nb_3O_{10}$ and $Ti_{0.87}O_2$ nanosheets. The films on $Ca_2Nb_3O_{10}$ nanosheets (Figure 4.3 a,b) were atomically smooth but contained deep trenches that formed a maze of nanostructures that meandered over the substrate. The trenches preferentially ran into two directions on a single nanosheet. This observation is also illustrated by the inset in image 4.3b, which shows the existence of fourfold symmetry in the two dimensional slope distribution analysis of the AFM image. The symmetry in the slope distribution analysis is a strong indication for epitaxy on the $Ca_2Nb_3O_{10}$ nanosheets, where facets follow preferred

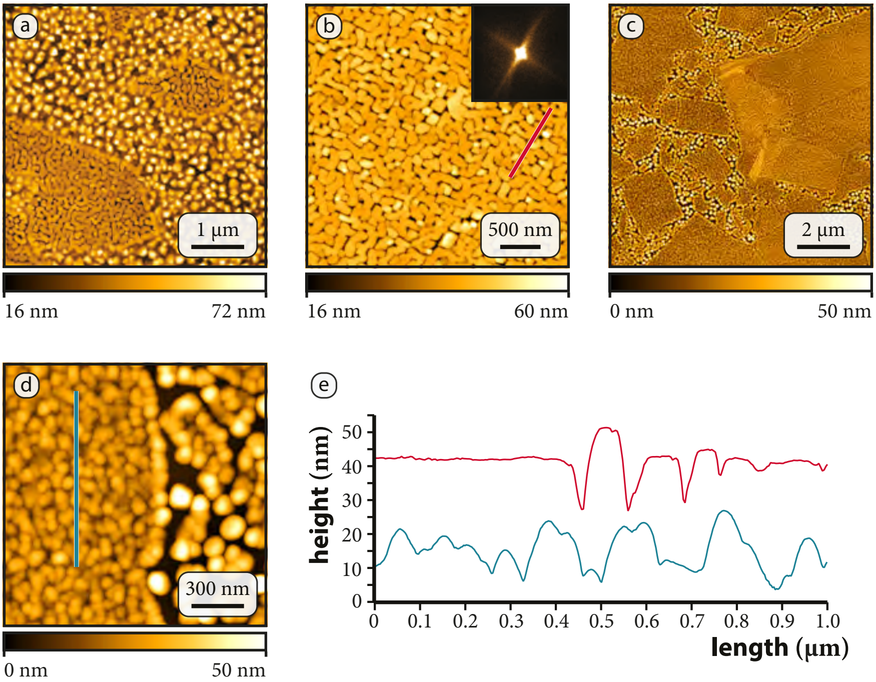

Figure 4.3: TM-AFM height images of $SrRuO_3$ deposited on Si substrates containing seed layers of (a,b) $Ca_2Nb_3O_{10}$ and (c,d) $Ti_{0.87}O_2$ nanosheets. The inset in (b) shows the slope distribution analysis from the corresponding AFM height image. (e) Height profiles measured along the lines in (b) (upper, red line) and (d) (lower, blue line).

crystallographic planes of $SrRuO_3$. On $Ti_{0.87}O_2$ nanosheets the $SrRuO_3$ layer had a typical grain structure in which no such symmetry could be found (Figure 4.3c,d). Regardless of the type of nanosheets that was used, the morphologies of the films were not significantly influenced by changing the deposition pressure between 0.03 and $0.6\ \mathrm{mbar}$, or the substrate temperature between 600 and $700\,^{\circ}\mathrm{C}$.

The observed strong variation in morphologies may be explained both by thermodynamic and kinetic considerations. Kinetically, roughness is determined by surface chemistries (*e.g.* surface charges, contaminations, or dislocations), which may affect sticking coefficients or diffusivities during deposition.[26,27] Thermodynamically, roughness can be caused by stress or by large surface or interfacial energies.[28] In the next chapter, experimental results are presented that suggest a thermodynamic origin for the observed roughening of films of $SrRuO_3$ on $Ca_2Nb_3O_{10}$.

Table 4.2: Lattice structure and parameters of the two kinds of nanosheets and $SrTiO_3$, together with the lattice mismatch of $SrRuO_3$ with these materials.

Material	Lattice structure	Lattice parameters	Mismatch $SrRuO_3$
$Ca_2Nb_3O_{10}$	2D square	$a = b = 3.86$ Å	$+1.7\,\%$
$Ti_{0.87}O_2$	2D rectangular	$a = 3.76$ Å $b = 2.97$ Å	$+4.3\,\%$ $-6.9\,\%$
$SrTiO_3$	3D cubic	$a_c = 3.905$	$+0.6\%$

XRD and EBSD results discussed below indicate epitaxial growth of $SrRuO_3$ on the individual (single crystalline) nanosheets. Relatively large lattice mismatches between the nanosheets and $SrRuO_3$, and consecutive large elastic strain from registry of the two lattices led to rapid development of stress and may explain roughening of these films. Table 4.2 shows the lattice mismatches for $(001)_{pc}$ and $(110)_{pc}$ oriented $SrRuO_3$ on $Ca_2Nb_3O_{10}$ and $Ti_{0.87}O_2$, respectively. The excessive growth of crystallites that was observed in between the nanosheets may be explained by suppression of nucleation due to absence of a periodic potential in the amorphous oxide layer on Si.

Large interfacial energies may have also caused roughening of the films. In particular, the $(110)_{pc}$ oriented film may have coarsened due to anisotropy in the surface energy. Generally in perovskite oxides, the $(001)_c$ planes have the lowest surface energy.[29–32] The facts that the $(001)_{pc}$ oriented crystallites on $Ca_2Nb_3O_{10}$ nanosheets had atomically smooth surfaces and square-shaped facets, indicate that $SrRuO_3$ forms no exception to this generality. Therefore, the $(110)_{pc}$ oriented film may have preferentially formed $(001)_{pc}$ surface planes, thereby increasing its roughness. This theory is further enforced by the high roughness that was measured on a film deposited on (110) $SrTiO_3$ ($R_q = 3.5$ nm).

ANALYSIS OF THE CRYSTAL ORIENTATION OF SRRUO3 ON NANOSHEETS

The XRD data in Figure 4.4a show the result of $\omega - 2\theta$ scans on different films. The bottom curve was obtained from a sample where $SrRuO_3$ was deposited directly on a silicon substrate, the middle curve was obtained when a layer of $Ti_{0.87}O_2$ nanosheets with a relative coverage of $96.3 \pm 0.9\,\%$ was used, and

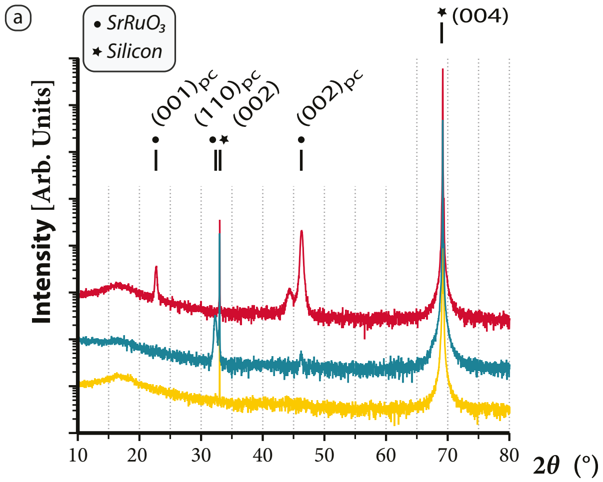

Figure 4.4: (a) XRD patterns of $SrRuO_3$ deposited on silicon (bottom curve), on silicon containing a monolayer of $Ti_{0.87}O_2$ nanosheets (middle curve, multiplied by a factor of 10), and on silicon containing $Ca_2Nb_3O_{10}$ nanosheets (top curve, $\times 100$). The black lines above the patterns indicate the theoretical positions of the diffraction spots of bulk $SrRuO_3$ and Si. Rocking curves that were made on the sample containing (b) $Ca_2Nb_3O_{10}$ ($2\theta = 46.28°$), and (c) $Ti_{0.87}O_2$ nanosheets ($2\theta = 32.26\,°$). The curve in (b) was fitted with a single Gaussian function, while two Gaussian functions were used to fit the curve in (c) (the background was fitted with a linear function).

the top curve was obtained with a seed layer of $Ca_2Nb_3O_{10}$ nanosheets having a relative coverage of $95.7 \pm 1.6\,\%$. When $SrRuO_3$ was directly deposited on silicon, no significant peaks other than those from the substrate were found. When $Ti_{0.87}O_2$ nanosheets were used, the strongest peak was found at $2\theta = 32.3°$. A rocking curve was made at this angle by scanning ω in a window of $18°$ (Figure 4.4c), yielding a FWHM of $3.4°$. A different orientation was measured on $Ca_2Nb_3O_{10}$ nanosheets, where peaks were observed at $2\theta = 22.7°$ and $46.3°$. In this case an additional peak was observed at $2\theta = 44.4°$, having an intensity of 4% compared to the peak at $2\theta = 46.3°$. The rocking curve that was made at $2\theta = 46.3°$ had a FWHM of $1.3°$ (Figure 4.4b).

Control of the crystallographic orientation by nanosheets is illustrated by the fact that film peaks were observed only when $SrRuO_3$ was deposited on nanosheets. The absence of film peaks in the case where $SrRuO_3$ was directly deposited on silicon can be explained by the lack of a preferred orientation in this case, together with the absolute amount of material in the films. The peak observed for the film on $Ti_{0.87}O_2$ nanosheets is matching well with the $(110)_{\mathrm{pc}}$ orientation of $SrRuO_3$. Also, the $(001)_{\mathrm{pc}}$ and $(002)_{\mathrm{pc}}$ planes of $SrRuO_3$ diffract at angles where the two main peaks were found for the film on $Ca_2Nb_3O_{10}$

nanosheets.[33] The ω rocking curves further confirmed preferred orientations of the crystallites when deposited on nanosheets. Thus, preferred out-of-plane orientations of the films were confirmed when seed layers of nanosheets were present.

The observed preferential out-of-plane orientation was in both cases expected from lattice matching with the underlying nanosheets (Table 4.2). After all, *pseudo*-cube on cube epitaxy of $SrRuO_3$ on $Ca_2Nb_3O_{10}$ nanosheets is most likely in the $[001]_{\mathrm{pc}}$ direction, while the rectangular structure of the $Ti_{0.87}O_2$ nanosheets most likely promotes growth in the $[110]_{\mathrm{pc}}$ direction. Besides, epitaxy is likely in these directions because then the oxygen octahedra of the films and nanosheets are aligned (Figure 4.1), resulting in a continuous octahedral backbone through the nanosheets and films. The FWHM of the two rocking curves are significantly different, suggesting that the crystallites were more strongly oriented on $Ca_2Nb_3O_{10}$ than on $Ti_{0.87}O_2$ nanosheets. This observation was also in accordance with the expectations, since the lattice mismatch between $Ca_2Nb_3O_{10}$ and $SrRuO_3$ is significantly smaller than that between $Ti_{0.87}O_2$ and $SrRuO_3$.

The positions of the peaks for both $SrRuO_3$ on $Ca_2Nb_3O_{10}$ and $Ti_{0.87}O_2$ nanosheets indicate that the films were free from strain ($d_{001} = 3.91$ nm and $d_{110} = 2.77$ nm). Most probably, elastic relaxation was accommodated by a large number of dislocations and grain boundaries in the films, which is in line with the observed morphologies, as discussed above. Another cause for release of strain may be found in the 'flexible nature' of the nanosheets, which may have resulted in a relaxed film on a strained seed layer.[17] A rational condition for the latter explanation is that the nanosheets should not clamp to the substrate at the high deposition temperatures. Fractions of the film on $Ca_2Nb_3O_{10}$ nanosheets may have been compressively strained, as that would explain the presence of the small peak ($d_{002} = 2.04$ nm). It is possible that a fraction of $SrRuO_3$ was strained by the unilamellar nanosheets or by thicker crystallites that had not been completely exfoliated into unilamellar sheets.

4.4 MAGNETIC ANISOTROPY IN $SrRuO_3$ FILMS ON NANOSHEETS

Temperature dependent magnetization measurements showed anisotropy when either a layer of $Ti_{0.87}O_2$ or $Ca_2Nb_3O_{10}$ nanosheets was used, but not when $SrRuO_3$ was directly deposited on Si (Figure 4.5). For both films on nanosheets, the easy axis was parallel to the surfaces. Fits of the saturation magnetization

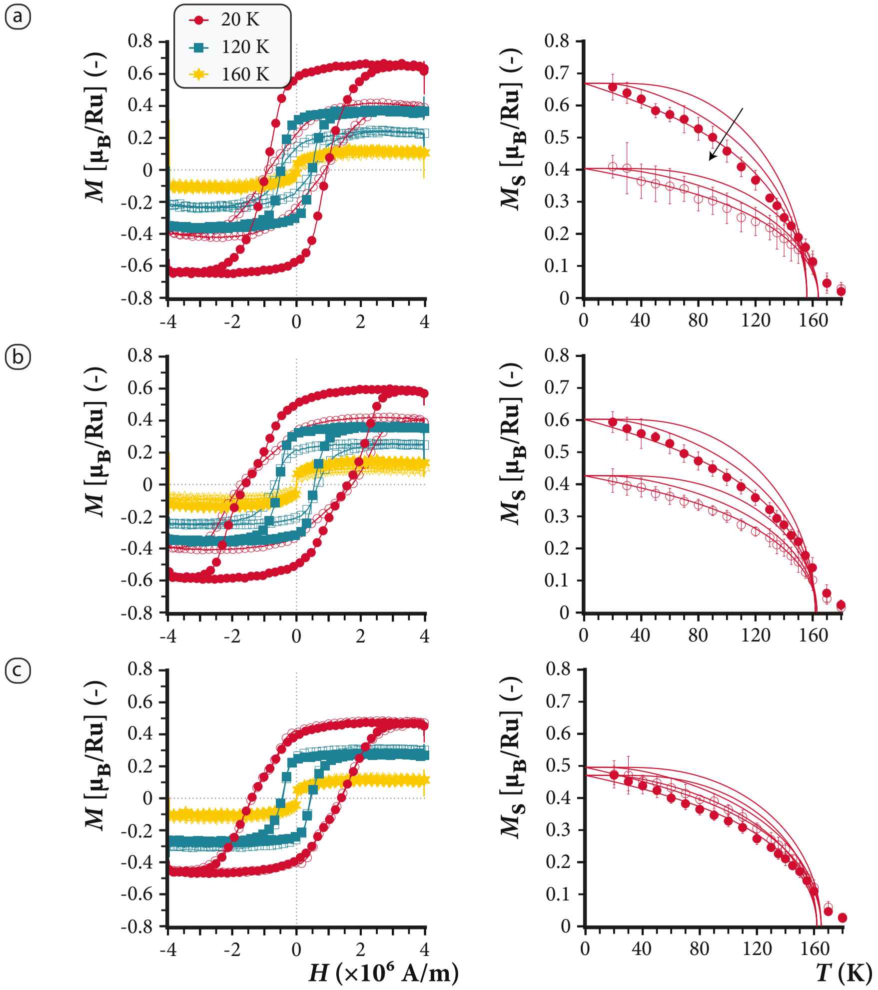

Figure 4.5: Magnetic characterization of $SrRuO_3$ on (a) $Ca_2Nb_3O_{10}$ nanosheets, (b) $Ti_{0.87}O_2$ nanosheets, and (c) silicon without a layer of nanosheets. The data represented by closed symbols were obtained by applying the magnetic field parallel to the plane of the surface, while the field was applied out-of-plane for the data represented by the open symbols. The left side shows magnetic hysteresis curves of films at 20 K, 120 K, and 160 K, for which the diamagnetic background signals from the silicon substrates were extracted. Temperature dependency of the saturation magnetization is displayed on the right, together with fits to Brillouin functions calculated from Weiss theory of ferromagnetism. With the assumption of zero external field and for different angular momenta (J), the theoretical curves were fitted (up to $155\ K$) to the data. Best fits were produced for different values of J by an iterative process, where alternately the absolute saturation magnetization ($M_{\mathrm{S,abs}}$) and the Curie point (T_{C}) were varied. $M_{\mathrm{S,abs}}$ and T_{C} where then chosen from the fit with the lowest least squares. Brillouin curves are shown for $J = 1,\ 4,$ and ∞, where J increases in the direction of the arrow.

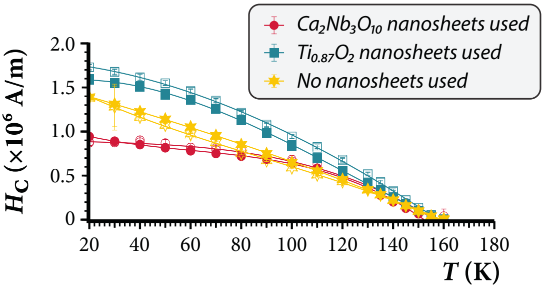

Figure 4.6: Coercive field as a function of temperature for $SrRuO_3$ deposited on silicon containing $Ca_2Nb_3O_{10}$, $Ti_{0.87}O_2$, and no nanosheets. The data obtained with the field applied in the plane of the surface are represented by closed symbols, while the open symbols represent data obtained with the field applied out-of-plane. The solid lines are fits to a third order function and serve only to guide the eye.

versus temperature to theoretical Brillouin functions with $J = 1,\ 4$, and ∞ showed that all data were best followed by the Langevin functional dependency (*i.e.* $J = \infty$). Ferromagnetic behavior was measured up to ~ 160 K in all three cases (Figure 4.5 and 4.6). The only exception was found when the field was applied in the plane of the surface for the case of $SrRuO_3$ on $Ca_2Nb_3O_{10}$ nanosheets, where the Curie temperature appeared ~ 6 K lower.

The anisotropy in the magnetic response for films deposited on nanosheets clearly illustrates that the control of orientation had a significant effect on the properties of the films and was therefore most probably of magnetocrystalline nature. In contrast to these results, the preferred direction of magnetization was measured to be out-of-plane when $SrRuO_3$ was deposited under the same conditions on (110) and (001) oriented $SrTiO_3$ substrates (see *e.g.* Figure 5.13 on page 109). These films on $SrTiO_3$ were compressively strained while those on nanosheets were free from strain. Due to the strong spin-orbit coupling in $SrRuO_3$, strain has a substantial effect on the magnetization. This was previously observed for $SrRuO_3$ on both (110) and (001) oriented $SrTiO_3$, where the strain was tuned between compressive and tensile by the introduction of a buffer layer.[34,35] In both of these cases, the easy axis rotated into the plane of the surface after changing the strain from compressive to tensile. Besides by strain, the direction of the easy axis may have been influenced by the roughness. The films were found to be rougher on the nanosheets than on the $SrTiO_3$ substrates. A preference for out-of-plane magnetization due to surface anisotropy might have been reduced because of the higher roughness of $SrRuO_3$ on the nanosheets. It is noted that on a macroscopic scale, the $SrRuO_3$ films were randomly oriented in the surface plane, because the nanosheet templates were also randomly oriented. On the other hand, the orientations of the films on the single crystalline substrates were fixed in all directions. The two classes of films were therefore essentially different and only for this reason differences in the magnetization behavior are expected.

The measured Curie temperatures are close to the value measured for bulk $SrRuO_3$ ($T_C \approx 165$ K).[18] When $SrRuO_3$ is strained, for example, by clamping on a substrate, the Curie temperature decreases. For example, Gan *et al.* found a Curie temperature of 150 K for $SrRuO_3$ on a (001) oriented $SrTiO_3$ substrate and showed that this temperature had increased by 10 K after decoupling the film from the substrate.[36] With respect to this study, the comparatively high Curie temperatures found in this work form yet another indication of relaxation of the films. The deviant value for the Curie temperature of $SrRuO_3$ on $Ca_2Nb_3O_{10}$ nanosheets may be explained by assuming that this film was partly strained, which is in line with the side peak observed in the XRD pattern of Figure 4.4.

Signatures of high concentrations of defects were seen from the magnetization measurements, for instance by the high coercivity as plotted in Figure 4.6 and the large switching areas in the hysteresis curves of Figure 4.5. These observations can be explained by a large number of free poles, which add up to the magnetostatic energy of the system. Free poles are formed both at the grain boundaries and at imperfections (*e.g.* dislocations) inside the grains, the latter ones cause pinning of the domains during domain wall motion resulting in an increase of the coercive force (compared to films with less imperfections). The magnetic characterization is in accordance with the AFM and XRD analyses, as all results indicate an abundance of grain boundaries and imperfections in the films. The coercive field was significantly lower when $SrRuO_3$ was deposited on $Ca_2Nb_3O_{10}$ than when it was deposited on $Ti_{0.87}O_2$ nanosheets. This observation is also in agreement with the XRD data, which indicated that crystal growth was controlled to a higher extent by $Ca_2Nb_3O_{10}$ than by $Ti_{0.87}O_2$ nanosheets.

The large concentration of defects and high roughness explains the observed classical magnetic behavior by the Langevin functional dependency. In addition, the absence of a preferred in-plane orientation may have caused the total of all magnetic spins in the films to show classical rather than quantum mechanical behavior. Note that a VSM is sensitive only for the complete magnetization of a sample. Therefore, no conclusions can be drawn on the magnetic behavior of $SrRuO_3$ on individual nanosheets.

4.5 TWO PREFERENTIAL ORIENTATIONS ON A SINGLE SUBSTRATE

One of the great promises of nanosheets is that different kinds can be deposited on a single substrate to locally control the orientation of a film deposited thereon. To illustrate this concept, a mixture containing both $Ca_2Nb_3O_{10}$ and $Ti_{0.87}O_2$ nanosheets was made and transferred onto a single substrate. On top of this monolayer, $SrRuO_3$ was deposited.

After the deposition of nanosheets, a densely packed monolayer with a relative coverage of $95.7\pm2.0\,\%$ was obtained (Figure 4.7). The two types of nanosheets could be distinguished in the AFM height images by their respective heights ($Ti_{0.87}O_2$ nanosheets have a thickness of $0.75\ \mathrm{nm}$, while $Ca_2Nb_3O_{10}$ nanosheets are $1.44\ \mathrm{nm}$ thick[37]). From the contrast in height, the relative coverage of $Ti_{0.87}O_2$ nanosheets was determined to be $69.6\pm2.3\,\%$ and the relative coverage of $Ca_2Nb_3O_{10}$ to be $26.1\pm2.8\,\%$. After PLD, both AFM (Figure 4.7b) and helium ion microscopy images (Figure 4.8) showed two clearly distinct surface morphologies on the $SrRuO_3$ film. Both a smooth layer containing trenches (typical for films on $Ca_2Nb_3O_{10}$ nanosheets) and more regular grains (typically observed on $Ti_{0.87}O_2$ nanosheets) were observed.

In the XRD pattern (Figure 4.9), both peaks corresponding to the $(00l)_{\mathrm{pc}}$ and $(hh0)_{\mathrm{pc}}$ planes were found. The FWHM of the two peaks were a bit larger than those found when $SrRuO_3$ was deposited on a substrate with just one of the two nanosheets. However, also in this case the rocking curve on the $(110)_{\mathrm{pc}}$ planes was significantly broader than that on the $(002)_{\mathrm{pc}}$ planes. Assuming that the shapes of the two rocking curves were independent of the rocking direction, the volumes (V) under the two curves were estimated by equation 4.1. This equation was obtained after taking a volume integral over the Gaussian function (I_0 is the intensity at the center of the curve). In a powder diffractogram, the relative intensities of the $(002)_{\mathrm{pc}}$ and $(110)_{\mathrm{pc}}$ peaks are $35\,\%$ and $100\,\%$, respectively.[33] After correcting for these values, the relative amounts of $SrRuO_3$ in the two particular orientations were estimated to be respectively $83\,\%$ and $17\,\%$. This result is another indication that the crystallographic orientation was significantly less well controlled on the $Ti_{0.87}O_2$ nanosheets than on the $Ca_2Nb_3O_{10}$ nanosheets.

$$V = \frac{\pi \cdot I_0 \cdot \mathrm{FWHM}^2}{4 \cdot \ln 2} \tag{4.1}$$

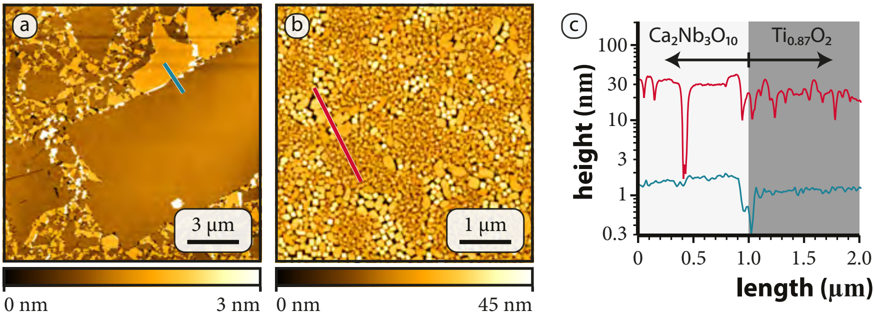

Figure 4.7: TM-AFM height images of a monolayer of mixed $Ca_2Nb_3O_{10}$ and $Ti_{0.87}O_2$ nanosheets on silicon (a) before and (b) after deposition of $SrRuO_3$. The height profiles of the lines drawn in (a) and (b) are shown in (c).

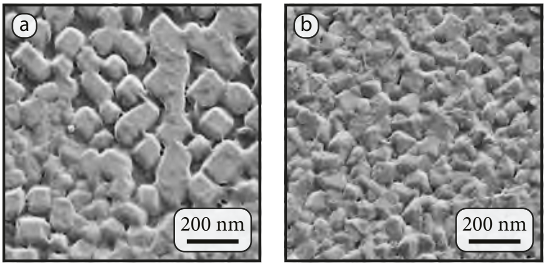

Figure 4.8: Helium ion microscopy images of $SrRuO_3$ on mixed $Ca_2Nb_3O_{10}$ and $Ti_{0.87}O_2$ nanosheets on silicon. Two different regions are shown that are characteristic for $SrRuO_3$ on (a) $Ca_2Nb_3O_{10}$ and (b) $Ti_{0.87}O_2$ nanosheets (acceleration voltage was $35\ \mathrm{kV}$, working distance was $5.5\ \mathrm{mm}$ and sample tilt was $20\,°$).

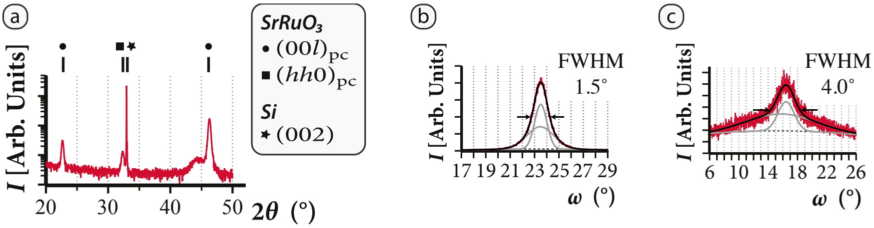

Figure 4.9: (a) XRD patterns of $SrRuO_3$ on silicon containing both $Ca_2Nb_3O_{10}$ and $Ti_{0.87}O_2$ nanosheets. Rocking curves (b) and (c) were obtained with 2θ fixed at $46.30°$ and $32.36°$, respectively. Both rocking curves were fitted with two Gaussian functions.

Part of the sample was mapped by EBSD, the results of which are shown in Figure 4.10. Areas with a clear $(001)_{\mathrm{pc}}$ orientation were present, as can be seen from the inverse pole figure map of the direction perpendicular to the surface (z). More interestingly, the inverse pole figure map of a parallel (x) direction showed that the individual $(001)_{\mathrm{pc}}$ oriented areas had a single orientation parallel to the plane of the surface. On the areas where no strong $(001)_{\mathrm{pc}}$ orientation was observed, the grains were mostly oriented with the $(110)_{\mathrm{pc}}$ planes parallel to the surface. The preference, however, was less clear in these areas than in the areas which showed a $(001)_{\mathrm{pc}}$ orientation. Two different areas were selected for which a single underlying nanosheet was expected. The two pole figures in Figure 4.10d and e were constructed from the resolved diffraction patterns obtained from these areas. A preferred $(001)_{\mathrm{pc}}$ orientation is observed in Figure 4.10d, while Figure 4.10e mainly shows $(110)_{\mathrm{pc}}$ oriented $SrRuO_3$.

The inverse pole figure maps and pole figures demonstrate that the orientation of the crystallites was controlled both parallel and perpendicular to the direction of growth. Particularly, the two pole figures clearly show that both $(001)_{\mathrm{pc}}$ and $(110)_{\mathrm{pc}}$ oriented $SrRuO_3$ had a single preferential orientation in all directions. This observation forms a strong indication for epitaxy, where the crystallographic orientations in the film were determined by the underlying nanosheets. The preference was more pronounced for the $(001)_{\mathrm{pc}}$ oriented parts than for the $(110)_{\mathrm{pc}}$ oriented parts. The difference is partly explained by the higher roughness of the film in the $(110)_{\mathrm{pc}}$ oriented areas, which led to a smaller band contrast in the diffraction patterns (Figure 4.10a). Stronger deviations from the $(110)_{\mathrm{pc}}$ orientation were also indicated by the XRD patterns and divergence of solutions in the inverse pole figure maps. Nevertheless, the single crystal orientations that were most clearly demonstrated by the two pole figures indicate that $SrRuO_3$ grew epitaxially on both $Ca_2Nb_3O_{10}$ and $Ti_{0.87}O_2$ nanosheets.

Magnetic characterization of the film on the mixed nanosheets is shown in Figure 4.11. Magnetization properties of this sample are expected to be the convolution of $SrRuO_3$ on $Ca_2Nb_3O_{10}$ and $Ti_{0.87}O_2$ nanosheets. Markedly, the preference for the magnetization parallel to the surface plane was less pronounced than when only one of the two types of nanosheets was used. This difference was probably caused by small experimental variations during fabrication and measurements of the samples.

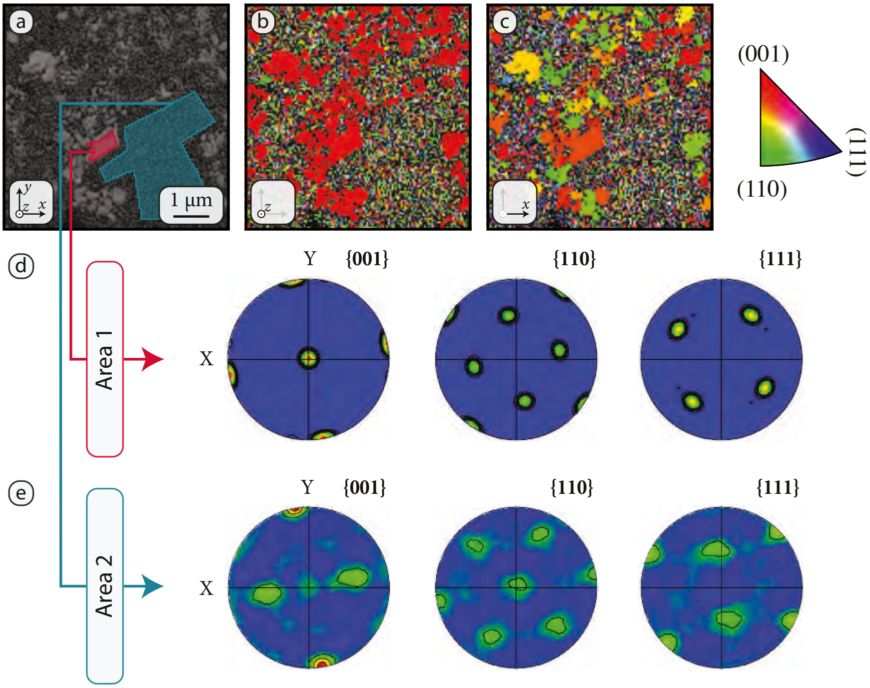

Figure 4.10: Electron backscatter diffraction images showing the (a) band contrast, (b) inverse pole figure map of the z-direction normal to the surface, (c) inverse pole figure map of the x-direction parallel to the surface, and (d,e) pole figures constructed from the two areas highlighted in the band contrast image (contouring was applied).

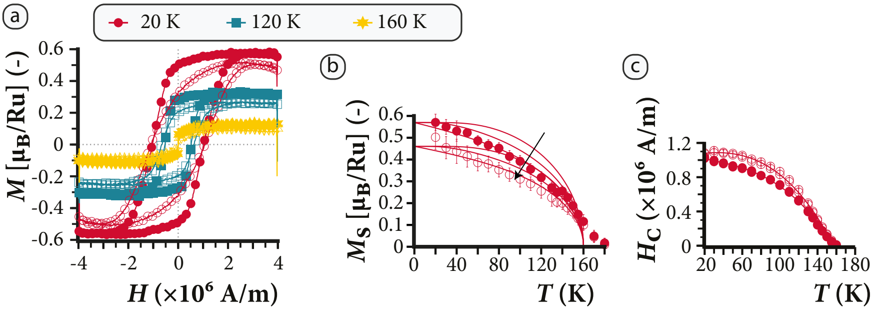

Figure 4.11: Magnetic characterization of $SrRuO_3$ on silicon containing both $Ca_2Nb_3O_{10}$ and $Ti_{0.87}O_2$ nanosheets. (a) Magnetic hysteresis loops for 20, 120, and 160 K. (b) Saturation magnetization versus temperature, together with fits to Brillouin functions (J increases in the direction of the arrow from 1 to 4 to ∞). (c) Coercive field plotted versus temperature, where the third order fits serve to guide the eye. Open symbols represent measurements in which the magnetic field was applied perpendicular to the surface of the sample, while closed symbols are used for the data that was obtained with the magnetic field applied parallel to the surface.

Only data about the complete magnetization of a sample can be obtained with a VSM, so local variations within samples could not be mapped. Since the orientation of $SrRuO_3$ is controlled locally by the different nanosheets, one may postulate that the film had position dependent magnetic properties that were determined by the type of nanosheet under the film. The relative distribution of the two kinds of nanosheets was completely random in this case, which was solved by developing a method to attain control of the positioning of nanosheets, as discussed in the next chapter. Such control may pave the way to advanced functional films where the properties are controlled locally by the crystallographic orientation.

4.6 CONCLUSIONS

Inorganic nanosheets of $Ca_2Nb_3O_{10}$ and $Ti_{0.87}O_2$ were placed on silicon substrates and used to control the nucleation of $SrRuO_3$ during growth by PLD. The nanosheets proved to influence both the crystallographic orientations and magnetic properties of the films. Magnetic anisotropy was measured when $SrRuO_3$ was deposited on one of the two types of nanosheets but not when it was deposited directly on a silicon substrate. The typical dimensions of nanosheets allow to control the orientations of films on much smaller length scales than what is typically achieved on single crystalline substrates. This concept was explored by deposition of $SrRuO_3$ on a mixed monolayer comprising both types of nanosheets. Compared to single crystalline substrates, nanosheets are still considered inferior because of poor control of their dimensions, shapes, positioning, and orientations. However, nanosheets may offer unique advantages over costly single crystalline substrates. For example, previous work proves that nanosheets can be placed on all sorts of (amorphous) substrates to gain control of the crystallinity of films deposited thereon. In this chapter, the aim was to show that another advantage lies in the ability to locally control the nucleation of materials, which allows tailoring their properties on a (sub-)micrometer scale. Possibly, such control will be having important implications in various fields and will prove useful for applications in, for instance, data storage and MEMS.

REFERENCES

[1] A. Tebano, A. Orsini, D. Di Castro, P. G. Medaglia, and G. Balestrino. "Interplay between crystallographic orientation and electric transport properties in $La_{2/3}Sr_{1/3}MnO_3$ films". *Appl. Phys. Lett.* **96** (9):092505, 2010.

[2] I. C. Infante, F. Sánchez, J. Fontcuberta, M. Wojcik, E. Jedryka, S. Estrade, F. Peiro, J. Arbiol, V. Laukhin, and J. P. Espinos. "Elastic and orbital effects on thickness-dependent properties of manganite thin films". *Phys. Rev. B: Condens. Matter Mater. Phys.* **76** (22):224415, 2007.

[3] M. Minohara, Y. Furukawa, R. Yasuhara, H. Kumigashira, and M. Oshima. "Orientation dependence of the schottky barrier height for $La_{0.6}Sr_{0.4}MnO_3/SrTiO_3$ heterojunctions". *Appl. Phys. Lett.* **94** (24):242106, 2009.

[4] H. Boschker, M. Mathews, E. P. Houwman, H. Nishikawa, A. Vailionis, G. Koster, G. Rijnders, and D. H. A. Blank. "Strong uniaxial in-plane magnetic anisotropy of (001)- and (011)-oriented $La_{0.67}Sr_{0.33}MnO_3$ thin films on $NdGaO_3$ substrates". *Phys. Rev. B: Condens. Matter Mater. Phys.* **79** (21):214425, 2009.

[5] K. Aoki, Y. Fukuda, K. Numata, and A. Nishimura. "Dielectric properties of (111) and (100) lead-zirconate-titanate films prepared by sol-gel technique". *Jpn. J. Appl. Phys., Part 1*, **33** (9 B):5155–5158, 1994.

[6] X. Du, J. Zheng, U. Belegundu, and K. Uchino. "Crystal orientation dependence of piezoelectric properties of lead zirconate titanate near the morphotropic phase boundary". *Appl. Phys. Lett.* **72** (19):2421–2423, 1998.

[7] H. N. Lee and D. Hesse. "Anisotropic ferroelectric properties of epitaxially twinned $Bi_{3.25}La_{0.75}Ti_3O_{12}$ thin films grown with three different orientations". *Appl. Phys. Lett.* **80** (6):1040–1042, 2002.

[8] A. Garg, Z. H. Barber, M. Dawber, J. F. Scott, A. Snedden, and P. Lightfoot. "Orientation dependence of ferroelectric properties of pulsed-laser-ablated $Bi_{4-x}Nd_xTi_3O_{12}$ films". *Appl. Phys. Lett.* **83** (12):2414–2416, 2003.

[9] H. Zheng, Q. Zhan, F. Zavaliche, M. Sherburne, F. Straub, M. P. Cruz, L. Q. Chen, U. Dahmen, and R. Ramesh. "Controlling self-assembled perovskite-spinel nanostructures". *Nano Lett.* **6** (7):1401–1407, 2006.

[10] H. Zheng, F. Straub, Q. Zhan, P. L. Yang, W. K. Hsieh, F. Zavaliche, Y. H. Chu, U. Dahmen, and R. Ramesh. "Self-assembled growth of $BiFeO_3$-$CoFe_2O_4$ nanostructures". *Adv. Mater.* **18** (20):2747–2752, 2006.

[11] J. Slutsker, I. Levin, J. Li, A. Artemev, and A. L. Roytburd. "Effect of elastic interactions on the self-assembly of multiferroic nanostructures in epitaxial films". *Phys. Rev. B: Condens. Matter Mater. Phys.* **73** (18):184127, 2006.

[12] Z. Tan, J. Slutsker, and A. L. Roytburd. "Epitaxial self-assembly of multiferroic nanostructures". *J. Appl. Phys.* **105** (6):061615, 2009.

[13] K. Kikuta, K. Noda, S. Okumura, T. Yamaguchi, and S. Hirano. "Orientation control of perovskite thin films on glass substrates by the application of a seed layer prepared from oxide nanosheets". *J. Sol-Gel Sci. Technol.* **42** (3):381–387, 2007.

[14] T. Shibata, K. Fukuda, Y. Ebina, T. Kogure, and T. Sasaki. "One-nanometer-thick seed layer of unilamellar nanosheets promotes oriented growth of oxide crystal films". *Adv. Mater.* **20** (2):231–235, 2008.

[15] T. Shibata, T. Ohnishi, I. Sakaguchi, M. Osada, K. Takada, T. Kogure, and T. Sasaki. "Well-controlled crystal growth of zinc oxide films on plastics at room temperature using 2D nanosheet seed layer". *J. Phys. Chem. C*, **113** (44):19096–19101, 2009.

[16] H. Tetsuka, H. Takashima, K. Ikegami, H. Nanjo, T. Ebina, and F. Mizukami. "Nanosheet seed-layer assists oriented growth of highly luminescent perovskite films". *Chem. Mater.* **21** (1):21–26, 2009.

[17] T. Shibata, Y. Ebina, T. Ohnishi, K. Takada, T. Kogure, and T. Sasaki. "Fabrication of anatase thin film with perfect c-axis orientation on glass substrate promoted by a two-dimensional perovskite nanosheet seed layer". *Cryst. Growth Des.* **10** (8):3787–3793, 2010.

[18] A. Callaghan, C. W. Moeller, and R. Ward. "Magnetic interactions in ternary ruthenium oxides". *Inorg. Chem.* **5** (9):1572–1576, 1966.

[19] A. Kanbayasi. "Magnetocrystalline anisotropy of $SrRuO_3$". *J. Phys. Soc. Jpn.* **41** (6):1879–1883, 1976.

[20] L. Klein, J. S. Dodge, T. H. Geballe, A. Kapitulnik, A. F. Marshall, L. Antognazza, and K. Char. "Perpendicular magnetic anisotropy and strong magneto-optic properties of $SrRuO_3$ epitaxial films". *Appl. Phys. Lett.* **66** (18):2427–2429, 1995.

[21] Q. Gan, R. A. Rao, C. B. Eom, L. Wu, and F. Tsui. "Lattice distortion and uniaxial magnetic anisotropy in single domain epitaxial (110) films of $SrRuO_3$". *J. Appl. Phys.* **85** (8 II B):5297–5299, 1999.

[22] J. I. Kim and C. U. Jung. "Magnetic properties of $SrRuO_3$ thin films having different crystal symmetries". *J. Magn.* **13** (2):57–60, 2008.

[23] R. Palai, H. Huhtinen, J. F. Scott, and R. S. Katiyar. "Observation of spin-glass-like behavior in $SrRuO_3$ epitaxial thin films". *Phys. Rev. B: Condens. Matter Mater. Phys.* **79** (10):104413, 2009.

[24] Y. Ebina, T. Sasaki, and M. Watanabe. "Study on exfoliation of layered perovskite-type niobates". *Solid State Ionics*, **151** (1-4):177–182, Nov. 2002.

[25] T. Tanaka, Y. Ebina, K. Takada, K. Kurashima, and T. Sasaki. "Oversized titania nanosheet crystallites derived from flux-grown layered titanate single crystals". *Chem. Mater.* **15** (18):3564–3568, 2003.

[26] B. Kuiper, J. L. Blok, H. J. W. Zandvliet, D. H. A. Blank, G. Rijnders, and G. Koster. "Self-organization of $SrRuO_3$ nanowires on ordered oxide surface terminations". *MRS Commun.* **1** (01):17–21, 2011.

[27] R. Bachelet, F. Sánchez, J. Santiso, C. Munuera, C. Ocal, and J. Fontcuberta. "Self-assembly of $SrTiO_3(001)$ chemical-terminations: A route for oxide-nanostructure fabrication by selective growth". *Chem. Mater.* **21** (12):2494–2498, 2009.

[28] I. V. Markov. *Crystal growth for beginners*. 2nd. World Scientific Publishing: Singapore, 2003.

[29] S. H. Kim, D. Y. Park, H. J. Woo, D. S. Lee, J. Ha, C. Seong Hwang, I. B. Shim, and A. I. Kingon. "Orientation effects in chemical solution derived Pb($Zr_{0.3}$,$Ti_{0.7}$)O_3 thin films on ferroelectric properties". *Thin Solid Films*, **416** (1-2):264–270, 2002.

[30] T. Sano, D. M. Saylor, and G. S. Rohrer. "Surface energy anisotropy of $SrTiO_3$ at $1400°\mathrm{C}$ in air". *J. Am. Ceram. Soc.* **86** (11):1933–1939, 2003.

[31] M. Alfredsson, J. P. Brodholt, D. P. Dobson, A. R. Oganov, C. R. A. Catlow, S. C. Parker, and G. D. Price. "Crystal morphology and surface structures of orthorhombic $MgSiO_3$ perovskite". *Phys. Chem. Miner.* **31** (10):671–682, 2005.

[32] Z. Xu, M. Suzuki, and S. Yokoyama. "Structure and optical band-gap energies of $Ba_{0.5}Sr_{0.5}TiO_3$ thin films fabricated by RF magnetron plasma sputtering". *Jpn. J. Appl. Phys.* **44** (12):8507–8511, Dec. 2005.

[33] W. Eysel and A. Geyer. "PDF reference code: 43-0472". In: *ICDD grant-in-aid*. Mineral.-Petrogr. Institut der Universitaet Heidelberg, Germany, 1992.

[34] C. U. Jung, H. Yamada, M. Kawasaki, and Y. Tokura. "Magnetic anisotropy control of $SrRuO_3$ films by tunable epitaxial strain". *Appl. Phys. Lett.* **84** (14):2590–2592, 2004.

[35] K. Terai, T. Ohnishi, M. Lippmaa, H. Koinuma, and M. Kawasaki. "Magnetic properties of strain-controlled $SrRuO_3$ thin films". *Jpn. J. Appl. Phys.* **43** (No. 2A):L227–L229, 2004.

[36] Q. Gan, R. A. Rao, C. B. Eom, J. L. Garrett, and M. Lee. "Direct measurement of strain effects on magnetic and electrical properties of epitaxial $SrRuO_3$ thin films". *Appl. Phys. Lett.* **72** (8):978–980, 1998.

[37] M. Osada and T. Sasaki. "Exfoliated oxide nanosheets: New solution to nanoelectronics". *J. Mater. Chem.* **19** (17):2503–2511, 2009.

5

CONTROLLED GROWTH AND PATTERNED ORIENTATIONS OF PEROVSKITE OXIDE THIN FILMS ON NANOSHEETS

Perovskite oxide heteroepitaxy was realized on top of the amorphous oxide surfaces of Si substrates by making use of inorganic nanosheets that acted as single crystalline templates during film growth. Thin films of $SrRuO_3$ were deposited in a $(001)_{\mathrm{pc}}$ and $(110)_{\mathrm{pc}}$ orientation on nanosheets of $Ca_2Nb_3O_{10}$ and $Ti_{0.87}O_2$, respectively. When deposited on a layer of $Ca_2Nb_3O_{10}$, the roughness of these films was reduced down to the atomic-scale by introducing a buffer layer of $SrTiO_3$. A stack of two layers of $Ti_{0.87}O_2$ nanosheets was required to obtain a film of $SrRuO_3$ that was well textured in the $[110]_{\mathrm{pc}}$ direction, because the first layer of nanosheets reacted with the substrate at the elevated deposition temperatures. The films had resistivities close to those measured for fully oriented ones, and showed magnetic anisotropy with the easy axes and Curie temperatures determined by the underlying nanosheets. The two types of nanosheets were patterned to locally tailor the crystallographic orientation and properties of $SrRuO_3$. The success of this approach was demonstrated by EBSD and spatial magnetization maps. An unprecedented control of perovskite film growth on Si substrates is illustrated in this chapter, and the methods that were developed to deposit $SrRuO_3$ thin films are a viable starting point for growth of artificial heteroepitaxial thin films that require a bottom electrode. Control was not just reached in the direction of film growth, as the crystal orientation was regulated laterally on the surface of micropatterned nanosheets. The concept of being able to pattern the orientation and properties of thin films creates new prospects for fabricating heterostructures that may find use in future generation devices.

5.1 INTRODUCTION

The past years have seen an inexhaustive interest in complex oxide electronics, which has largely been fueled by the atomic scale precision with which metal oxide thin films can be deposited and the associated phenomena originating from the artificial interfaces, epitaxial stress and strain, and/or crystallographic orientation.[1–8] Development and commercialization of perovskite-based devices has for a large part been hampered by the challenge to interlace the technology with existing (Si-based) processes, which is related to the requirement for a lattice-matching inert crystal to direct the film formation. Ideally, full control of the crystal structure as can be reached on single crystalline substrates should not only be retained, but also scaled-down in order to achieve miniaturization. Textured growth of various metal oxide layers on arbitrary substrates was recently illustrated by epitaxy on inorganic nanosheets,[9–15] which by their lateral sizes in the (*sub*-)$\mu\mathrm{m}$ range and variety of crystal lattices[16] allow for new possibilities to locally tailor the important structural parameters of a thin film. This opportunity is exploited in this chapter, for which a perovskite oxide thin film was fabricated in which the strain, crystallographic orientation, and properties were patterned for the first time. Therewith, one of the restrictions for the design of functional devices is lifted, as this approach allows to locally control the growth and properties of thin films without changing their compositions.

PLD was used to form thin films of $SrRuO_3$ on silicon substrates with amorphous oxide surfaces, during which two different kinds of nanosheets were used to orchestrate crystal growth: Crystalline templates of $Ca_2Nb_3O_{10}$ led to epitaxial growth in the $[001]_{\mathrm{pc}}$ direction, while seed layers of $Ti_{0.87}O_2$ yielded $(110)_{\mathrm{pc}}$ oriented films. The conducting perovskite was deposited not only as model material to illustrate the ability to locally tune its magnetic behavior, but also because of its widespread application as electrode in all oxide heterostructures.[17] Results on growth of this material on substrates covered exclusively with nanosheets of either $Ca_2Nb_3O_{10}$ or $Ti_{0.87}O_2$ are discussed first, and the purpose of these studies was to comprehend and improve growth on the individual nanosheets. Several ways are introduced to master film growth on top of the two-dimensional seed crystals, which led to thin films of $SrRuO_3$ that showed strong resemblance to fully oriented ones when *e.g.* roughnesses or resistivities were compared. The properties of the films are shown to depend on the underlying nanosheets, and by fabricating micropatterns of both types of nanosheets, these properties were combined into a single sample.

5.2 EXPERIMENTAL METHODS

EXFOLIATION AND DEPOSITION OF NANOSHEETS The same materials and precursors were used as mentioned in the previous chapter from page 66. The precursor powder of choice (0.4 g) was added to a screw cap bottle (250 ml polypropylene from Kautex) containing 100 ml water. The bottle was shaken vigorously for 1 min, after which TBAOH ($40\% \ w/w$; $479 \ \mu\text{l}$ in the case of HCNO and $845 \ \mu\text{l}$ in the case of HTO) was added and mixed with the dispersion by flipping the bottle upside-down ($10\times$). The bottle was then placed horizontally on a rocking-shaker operating at 30 oscillations per minute, and was kept there for 9 (HCNO) or 6 days (HTO). The content of the bottle, including all precipitate, was then diluted in water (400 ml in the case of HCNO and 1900 ml in the case of HTO) and stored for 5 (HCNO) or 4 (HTO) days before use.

Prior to a Langmuir-Blodgett deposition, the surface of the Si substrate was cleaned in a similar way as described in the previous chapter, that is by snow jetting and plasma cleaning. Samples that already contained one or more layers of nanosheets and required an additional layer were cleaned by plasma only (for 2 min). When $Ca_2Nb_3O_{10}$ nanosheets were to be deposited, a syringe was used to carefully extract 50 ml of the top part of the stock dispersion and add the dispersion to the Langmuir trough. For the deposition of $Ti_{0.87}O_2$ nanosheets, a pipette (Eppendorf) was used to transfer the stock dispersion ($4 \times 5 \text{ ml}$) to a screw cap bottle (100 ml polypropylene from Kautex) after which water was added (30 ml; without further agitation). After 15 min of waiting, this dilution was poured into the Langmuir trough. After waiting for (another) 15 min, the cleaned substrate was clamped on the dipper and the Wilhelmy plate was hanged in place on the microbalance after completely immersing it in the dispersion. The dipper was then lowered to submerge the substrate in the liquid, and after again 15 min the microbalance was tared and movement of the barriers was initiated. The actual transfer of a monolayer of nanosheets was done in a similar way as described on page 68. Before conducting any further experiments other than topographic analysis by AFM, all samples were annealed in a microwave furnace (Microsynth, Milestone Srl) that was heated from room temperature to $600 \ ^\circ\text{C}$ at maximum power (1.0 kW) for 30 min.

PATTERNING OF NANOSHEETS

To make alternating line patterns of $Ca_2Nb_3O_{10}$ and $Ti_{0.87}O_2$ nanosheets, first two monolayers of $Ti_{0.87}O_2$ nanosheets were deposited and annealed. On top of this sample, hexamethyldisiloxane (Merck) was spin coated first (at 4000 rpm for 45 s), followed by casting a $1.7\ \mu\mathrm{m}$ thick layer of photoresist (OiR 907-12 from Olin Microelectronic Materials Inc.; spin coated at 4000 rpm for 30 s) and heating at $90\ ^{\circ}\mathrm{C}$ for 2 min. The sample was then optically exposed (in a Karl Suss MA56 Mask Aligner for 10 s with a Hg lamp emitting at wavelength $\nu = 365\ \mathrm{nm}$ and yielding a surface power density $I = 10\ \mathrm{mW\,cm^{-2}}$) under a mask containing various line gratings ranging from $2\ \mu\mathrm{m}$ to $50\ \mu\mathrm{m}$ in width. The photoresist was subsequently developed (for 1 min using OPD 4262 from Arch Chemicals) and baked on a hot plate at $110\ ^{\circ}\mathrm{C}$ for 2 min. Prior to the Langmuir-Blodgett deposition of a layer of $Ca_2Nb_3O_{10}$ nanosheets, the patterned sample was treated with a plasma of oxygen (at 30 W for 2 min; Harrick plasma). After the deposition, the sample was held upside-down in a beaker containing acetone, carefully moved back and forth for 1 min, dipped in and then rinsed with ethanol, and finally dried in a stream of N_2. HR-SEM images of the resulting pattern can be found in Figure 5.1, which demonstrate the success of patterning.

PULSED LASER DEPOSITION OF $SrTiO_3$ AND $SrRuO_3$

Pulsed laser depositions were carried out in a vacuum system equipped with high pressure RHEED (TSST, the Netherlands) and using a KrF excimer laser (LPXpro from Coherent Inc.; operated at 21.5 kV and $\nu = 248\ \mathrm{nm}$). The central part of the laser beam was selected with a mask (rectangular shaped with rounded corners and an aperture of $56\ \mathrm{mm}^2$) and focused on the target of choice to a spot size of $1.8\ \mathrm{mm}^2$. The laser output was controlled with a variable attenuator to yield a fluence of $1.30\ \mathrm{J\,cm^{-2}}$ or $2.10\ \mathrm{J\,cm^{-2}}$ on the stoichiometric targets of $SrTiO_3$ (single crystalline target) or $SrRuO_3$ (sintered powder from Praxair electronics), respectively. Using a continuous stream of O_2 gas, the vacuum chamber ($P_{\mathrm{base}} < 1 \cdot 10^{-6}$ mbar) was brought to a pressure of $P = 0.080$ mbar, after which the targets were pre-ablated (at 5 Hz for 6 min) to remove possible surface contaminations. The resistive heater was then placed in deposition position (directly facing the target at a distance of 5 cm) and heated to $700\ ^{\circ}\mathrm{C}$ at $50\ ^{\circ}\mathrm{C\,min^{-1}}$ (controlled by a thermocouple inside the heater). For deposition of $SrTiO_3$, the pressure was reduced to $P = 0.010\ \mathrm{mbar}$, whereas $SrRuO_3$ was deposited at the same pressure as used

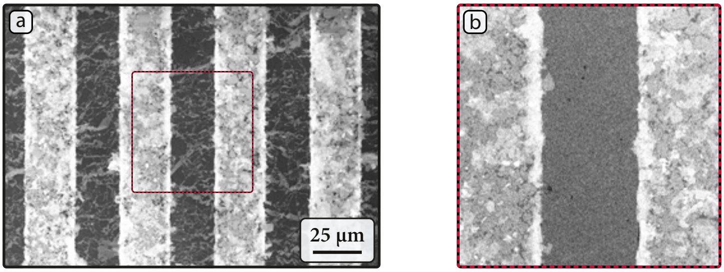

Figure 5.1: High-resolution SEM images of a pattern of $25\ \mu\mathrm{m}$ wide lines of $Ca_2Nb_3O_{10}$ nanosheets on top of two layers of $Ti_{0.87}O_2$ nanosheets supported on a Si substrate, measured using (a) an in-lens and (b) an EsB detector. The latter detector is particularly sensitive to compositional contrast, in the present case to the different atomic numbers of Ti and Nb.

during pre-ablation. In general, $SrTiO_3$ was deposited for $10\ \mathrm{min}$ and $SrRuO_3$ for $20\ \mathrm{min}$, in the course of which both targets were ablated at $1\ \mathrm{Hz}$. After deposition, the samples were cooled in $100\ \mathrm{mbar}$ O_2 at a maximum rate of $20\ ^{\mathrm{o}}\mathrm{C}\,\mathrm{min}^{-1}$.

Analysis and characterization

X-ray reflectivity and diffraction were performed either on an X'pert PRO MRD or an X'pert PRO Powder diffractometer (from PANalytical), both equipped with a Göbel mirror and a PIXcel detector (3D in the case of the MRD; 1D in the case of the Powder). In addition, a four-bounce Ge(220) monochromator was used on the MRD and for selected experiments the PIXcel$^{3\mathrm{D}}$ detector was replaced by a proportional counter with a triple axis module. For the films on nanosheets, ω was aligned on reflectance rather than the diffraction peak of the substrate. Lattice parameters were determined by fitting the different diffraction peaks with Gaussian functions, after which the Nelson-Riley function was used to determine the expected values and errors.

AFM, HR-SEM, EBSD, and magnetization measurements (VSM and scanning MOKE) were performed with the same equipment as mentioned in chapter 2, but the EBSD data discussed in this chapter were fitted using the refined indexing option (Aztec 2.2). Resistance was measured with a PPMS, using a probe current of $1\ \mu\mathrm{A}$, at which a resistance in the $k\Omega$ range was measured for the native Si substrate (in contrast to the thin films, the resistance of the substrate was non-ohmic of origin). Before conducting magnetization measurements, the samples were cut using a wafering blade (Isomet, Buehler) to fit in the pick-up coil, and their back-sides were polished to remove possible magnetic contaminations.

5.3 GROWTH AND PROPERTIES OF $\mathrm{SrRuO_3}$ ON $\mathrm{Ca_2Nb_3O_{10}}$

OPTIMIZATION OF GROWTH OF $\mathrm{SrRuO_3}$ BY INTRODUCTION OF A BUFFER LAYER Nanosheets were transferred onto Si substrates by Langmuir-Blodgett depositions, after which AFM was used to confirm successful formation of dense monolayers. An example of a resulting image is given in Figure 5.2a, in which single nanosheets can be recognized that collectively formed a closely packed film, of which only a minor part consisted of overlapping or stacked sheets. Based on AFM images recorded at six random locations, the coverage of nanosheets on this sample was determined to be $95 \pm 2\ \%$.

Utilizing RHEED during subsequent PLD of $SrTiO_3$ and $SrRuO_3$, growth was monitored *in situ* by measuring the intensity and FWHM of the specular spot. It developed from a faint elongated spot before growth (Figure 5.3a) into a spot of much higher intensity which remained clearly visible during the entire depositions of both $SrTiO_3$ (Figure 5.3b) and $SrRuO_3$. As shown in Figure 5.3c and observed in all of the experiments performed, the intensity of the specular spot dipped during deposition of the first one or two monolayers of $SrTiO_3$, after which it sharply increased and started to oscillate while it further increased steadily.

The low intensity of the RHEED specular spot observed before growth can be explained by the small number of crystal planes in the nanosheets. During the first few pulses of $SrTiO_3$, the intensity of the specular spot dropped even further due to increased scattering of the electrons from the coarsened surface. Continuation of growth led to formation of additional crystal planes from which the electrons could diffract, causing the (sharp) increase of intensity. Most importantly though, oscillations were observed which are a footprint of atomic layer-by-layer growth and enable monitoring and controlling thin film growth on the atomic level. Note that similar observations have only been reported on lattice-matching single crystalline substrates, while in this case epitaxial registry with the substrate was absent.

Figure 5.2b shows an AFM image of this sample after growth of the $SrTiO_3$ and $SrRuO_3$ heterostructure. The sample was analyzed by X-ray reflectivity (XRR) and XRD as well, and resulting values for the thicknesses, roughnesses and out-of-plane lattice parameters of both perovskite layers are given in Table 5.1. This table also includes values for the same variables of a $SrRuO_3$ thin film that was deposited under similar conditions on a $(001)_\mathrm{c}$ oriented single crystalline substrate of $SrTiO_3$, which was made for reference. XRD data in

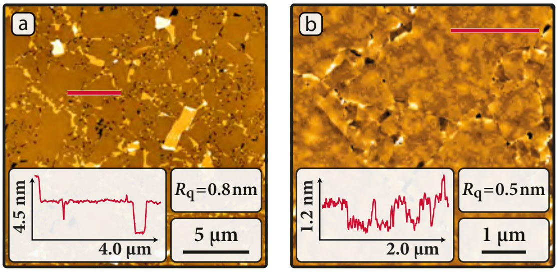

Figure 5.2: TM-AFM height images of (a) a layer of $Ca_2Nb_3O_{10}$ nanosheets on Si measured directly after Langmuir-Blodgett deposition and (b) the same sample after PLD of $SrTiO_3$ and $SrRuO_3$. The insets show height profiles measured along the (red) lines in the corresponding images and values for the RMS roughness (R_q) are given as well.

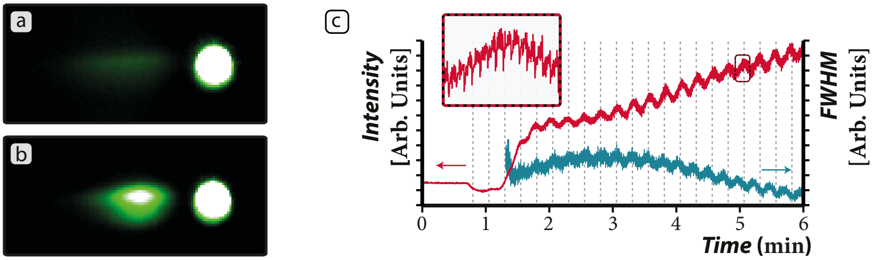

Figure 5.3: RHEED images (a) before and (b) after growth of $SrTiO_3$ together with (c) the evolution of specular spot intensity (red) and FWHM (blue) during initial growth of $SrTiO_3$ (the inset is a magnification of a single oscillation).

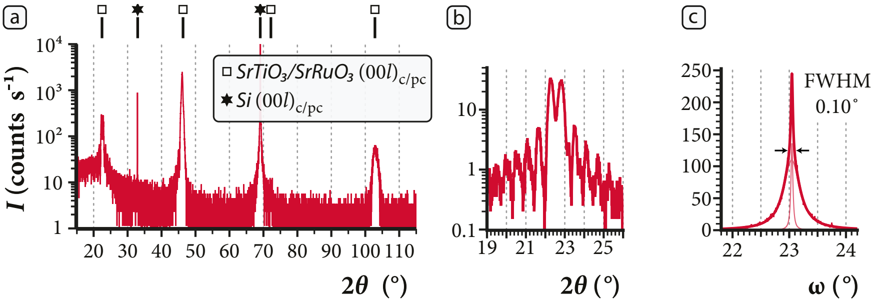

Figure 5.4: XRD patterns of a film of $SrRuO_3|SrTiO_3$ on a Si substrate covered with a monolayer of $Ca_2Nb_3O_{10}$ nanosheets, showing results from (a,b) $2\theta - \omega$ scans, and (c) ω-rocking around $2\theta = 46.08^{o}$. The pattern in image (b) was recorded using a triple axis module, and the rocking curve in (c) is displayed together with fits to two Lorentzian functions.

Figure 5.4 indicate that both layers of $SrTiO_3$ and $SrRuO_3$ were epitaxially coupled to the underlying nanosheets. In the $2\theta - \omega$ scan of Figure 5.4a, all peaks could be assigned either to the $(00l)_{\mathrm{c/pc}}$ planes of the perovskite oxide layers or of the Si substrate. The out-of-plane lattice parameters indicate that at least the layer of $SrRuO_3$ was compressively strained on the $SrTiO_3$ buffer layer. The lattice spacing of the interlayer was also larger than that of bulk $SrTiO_3$, but the obtained value does not necessarily signify that the buffer layer was compressively strained. Film peaks were found when similar growth conditions were used to deposit $SrTiO_3$ on a single crystalline substrate of $SrTiO_3$, suggesting that the increased lattice parameter may just as well have resulted from off-stoichiometric growth. Clear Laue oscillations were observed around the $(001)_{\mathrm{c/pc}}$ diffraction spots (Figure 5.4b), the periodicities of which corresponded well with the thicknesses of the two layers as determined from XRR. A strong preferential orientation of the layers was confirmed from ω-rocking scans around the $(002)_{\mathrm{c/pc}}$ peaks assigned to $SrTiO_3$ (at $2\theta = 46.47\,^o$) and $SrRuO_3$ (at $2\theta = 46.08\,^o$); the latter rocking curve can be found in Figure 5.4c. The rocking curves were best fitted with two Lorentzian functions having a combined FWHM of 0.10^o, which is the smallest value ever reported for a film on nanosheets. Still, the spread of crystal orientations is larger than that measured for the film of $SrRuO_3$ deposited on a $(001)_{\mathrm{c}}$ oriented $SrTiO_3$ substrate (FWHM $= 0.03^o$).

Films grown on nanosheets were almost as smooth as those deposited on single crystalline $(001)_{\mathrm{c}}$ oriented $SrTiO_3$ substrates, and even atomic terraces were observed, as illustrated by the height profile in Figure 5.2b. Growth clearly benefited from the presence of the interlayer of $SrTiO_3$, since islands of $SrRuO_3$ were obtained when the buffer layer was excluded. The reason for the strong influence of the buffer layer on the morphology of $SrRuO_3$ may be twofold: The newly created interfaces lead to alteration of the interfacial energies and chemistries, which influences growth kinetics of $SrRuO_3$; and epitaxial strain may be released in the interlayer, which leads to slower evolution of stress during epitaxial growth of the conducting perovskite. To distinguish between these two possible causes, the effect of reducing the thickness of the interlayer on the morphology of the films of $SrRuO_3$ was studied *ex situ* (see Figure 5.5). These studies showed that the first unit cells of $SrTiO_3$ played a crucial role in the formation of islands during deposition of $SrRuO_3$, since only four to six unit cells were required to obtain smooth films of $SrRuO_3$. Smooth interlayers were

Table 5.1: Values obtained from analysis and characterization of films of $SrRuO_3$ on single crystalline $SrTiO_3$ substrates, and films of $SrRuO_3|SrTiO_3$ on Si substrates containing $Ca_2Nb_3O_{10}$ or $Ti_{0.87}O_2$ nanosheets. Values for the layer thickness (t) and roughness (R) were determined by XRR, and the out-of-plane lattice parameters (d) were determined from $2\theta - \omega$ scans. The number in brackets behind every value is the error of the last digit to fall within a certainty of 95%. The characterization part includes values for the absolute saturation magnetization ($M_{\mathrm{s,abs}}$), Curie temperature (T_{C}), sheet resistivity at 300 K ($\rho_{300\,\mathrm{K}}$), and the residual resistivity ratio ($\rho_{300\,\mathrm{K}}/\rho_{5\,\mathrm{K}}$).

Substrate	**Layer**	**Analysis**			**Characterization**			
		t (nm)	R (nm)	d (Å)	$M_{\mathrm{s,abs}}$ $[\mu_{\mathrm{B}}/\mathrm{Ru}]$	T_{C} (K)	$\rho_{300\,\mathrm{K}}$ $(\mu\Omega cm^{-1})$	$\frac{\rho_{300\,\mathrm{K}}}{\rho_{5\,\mathrm{K}}}$
Si with $Ca_2Nb_3O_{10}$	$SrRuO_3$ $(001)_{\mathrm{pc}}$	14.5(1)	0.67(3)	3.942(4)	1.05	137	360	2.6
	$SrTiO_3$ $(001)_{\mathrm{c}}$	17.2(3)	0.5(2)	3.915(7)				
$SrTiO_3$	$SrRuO_3$ $(001)_{\mathrm{pc}}$	14.1(3)	0.23(4)	3.96(1)	1.20	125	322	2.7
Si with $Ti_{0.87}O_2$	$SrRuO_3$ $(110)_{\mathrm{pc}}$	13(1)	3.1(3)	3.925(8)	1.04	155	358	3.7
	$SrTiO_3$ $(110)_{\mathrm{c}}$	18.3(5)	1.1(5)	3.908(3)				
$SrTiO_3$	$SrRuO_3$ $(110)_{\mathrm{pc}}$	14(2)	4.2(7)	3.958(3)	1.47	154	318	5.9

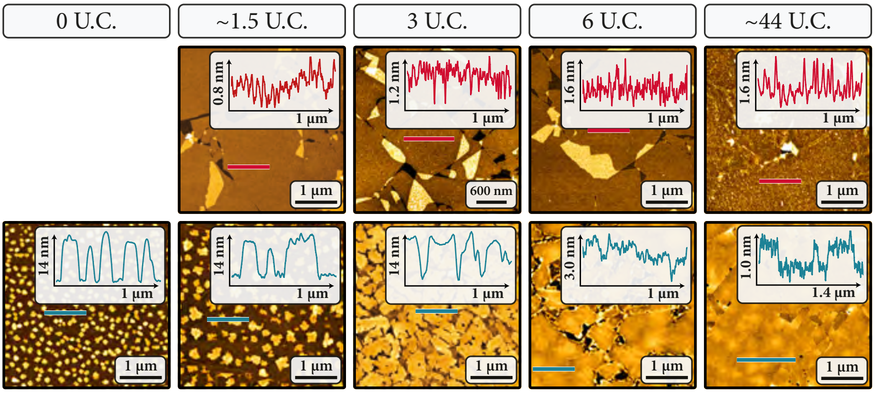

Figure 5.5: TM-AFM height images of films deposited on Si substrates containing monolayers of $Ca_2Nb_3O_{10}$ nanosheets, recorded after deposition of the buffer layer of $SrTiO_3$ (top) and after growth of the buffer layer followed by growth of approximately $14\ \mathrm{nm}$ $SrRuO_3$ (bottom). In the different experiments, the thickness of the buffer layer was varied between 0 and 44 unit cells (U.C.) as indicated above the AFM images. In all images a horizontal line can be found, marking the location from which the height profile in the corresponding inset was obtained.

obtained in every case, and the AFM data indicate that three unit cells were sufficient to completely cover the surfaces of the nanosheets. Still, nucleation of islands was not completely suppressed in this case, which suggests that island formation can not be explained solely by interfacial effects.

The other hypothesis to explain the effect of the buffer layer that remains standing, namely that the initially large lattice mismatch between $SrRuO_3$ and the nanosheets ($+1.7\%$) was reduced by the introduction of an interlayer of $SrTiO_3$, is more plausible. Since the roughness of the $SrRuO_3$ thin film was determined by the first unit cells of the buffer layer, this hypothesis requires that elastic strain was relieved in the first few atomic layers of $SrTiO_3$. Relaxation of the buffer layer may have resulted from formation of dislocations to reduce stress caused by lattice matching with the nanosheets, but may also be explained by transfer of strain into the nanosheets. The latter option considers the nanosheets to be flexible as a result of their two-dimensional nature,[12,13] but requires them to be attached to the substrate by weak (non-directional) interactions only during PLD of the initial atomic layers. When a film with larger lattice parameters than that of the nanosheets is grown (like in the present case), sufficient space should be available for the nanosheets to allow their lateral expansion. Considering the dense packing of nanosheets, large atomic displacements in the nanosheets were obstructed with the result that generation of defects in the film was inevitable.

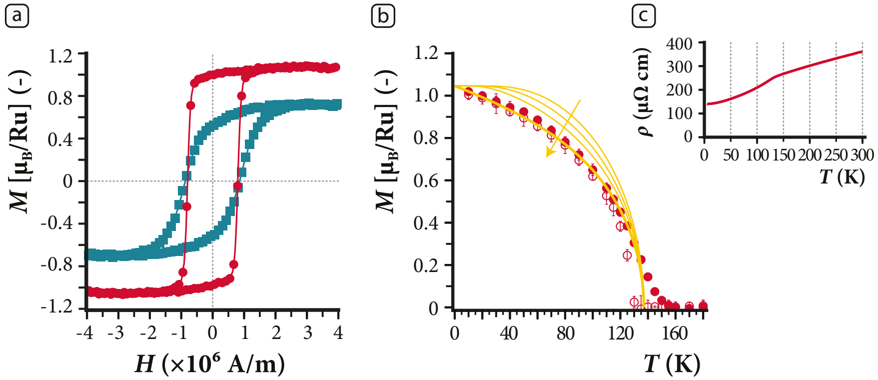

Figure 5.6: Magnetic and electrical characterization of the film of $SrRuO_3$ on Si containing a seed layer of $Ca_2Nb_3O_{10}$ nanosheets and a buffer layer of $SrTiO_3$. (a) Magnetic hysteresis curves obtained at $10\ \mathrm{K}$ measured with the field applied in the surface plane (blue squares) and out-of-plane (red circles). (b) Temperature dependence of saturation magnetization (closed circles) and remnant magnetization (open circles) for the out-of-plane direction, together with Brillouin curves (in yellow) from Weiss theory of ferromagnetism for different total angular momentum quantum numbers $J = 1, 2, 4, \infty$, where J increases in the direction of the arrow (the best fit is displayed in bold, the other curves use the values of the absolute saturation magnetization and Curie temperature obtained from the best fit). (c) Sheet resistivity (ρ) plotted versus temperature.

MAGNETIC AND ELECTRICAL CHARACTERIZATION OF THE $(001)_{\mathrm{pc}}$ ORIENTED FILM

Since $SrRuO_3$ is a good conductor and possesses large magnetocrystalline anisotropy that is highly sensitive to its condition in a thin film, the material has served as electrode in various perovskite heterostructures, and has evolved as model system for studying magnetism.[17] Here, magnetic and electrical properties were studied to evaluate the applicability of the film as conducting layer, and to understand how properties are determined by the seed layer, putting this film in perspective with a fully oriented one.

Figure 5.6a shows magnetic hysteresis loops of the sample measured at $10\ \mathrm{K}$ for the in-plane (blue squares) and out-of-plane (red circles) directions. In both cases a coercive field of $H_c = 0.8 \cdot 10^6\ \mathrm{A\,m^{-1}}$ was measured, and the easy axis was found to be pointing out of the surface plane. The temperature dependence of saturation and remnant magnetization measured along the easy direction is shown in Figure 5.6b, and includes the best result from fits of the saturation magnetization with Brillouin functions for different total angular momentum quantum numbers (J). The best fit was obtained for the Langevin functional dependency ($J = \infty$), yielding an absolute saturation magnetization and Curie temperature as given in Table 5.1. This table also includes values for the room temperature resistivity and residual resistivity ratio obtained from the graph displayed in Figure 5.6c. Values resulting from magnetic and electrical characterization of the reference film of $SrRuO_3$ on single crystalline $SrTiO_3$ are also included in Table 5.1.

Clear magnetic anisotropy was observed together with a Curie temperature lower than that of bulk $SrRuO_3$. The reduced Curie temperature was the result of strain in the layer of $SrRuO_3$, as strain is known to affect both electrical and magnetic properties of the material.[18,19] An even lower Curie temperature was observed in the film on $(001)_c$ oriented $SrTiO_3$ (see Table 5.1 and Figure 5.13 in the appendix). This observation indicates that $SrRuO_3$ experienced more strain from the single crystal than from the buffer layer on nanosheets, which is in accordance with the out-of-plane lattice parameters. Variation of stoichiometry between the single crystal and buffer layer may explain the different amounts of strain between the two films of $SrRuO_3$. In addition, imperfections existing in the interlayer may affect growth of $SrRuO_3$, and lead to partial relaxation of strain.

Upon further comparing the magnetic properties of the fully oriented film and the film on nanosheets, a stronger anisotropy was found in the former case. Full comparison between the two samples in this context is not meaningful, since one sample had a single crystallographic orientation while the other had an orientation that was only fixed in the out-of-plane direction. Still, this difference may be explained by unequal strain states between the two films, as strain has a strong influence on anisotropy in films of $SrRuO_3$.[19] Another difference between the two samples is that Brillouin fits suggest classical behavior ($J = \infty$) of the spins in $SrRuO_3$ on nanosheets, while partial quantization of the angular momentum ($J = 4$) is indicated for the fully oriented film. This difference is possibly the result of the slightly better out-of-plane crystallographic order in the film on the $SrTiO_3$ substrate, resulting in detection of quantization only in this case.

Even though the film of $SrRuO_3$ and $SrTiO_3$ on $Ca_2Nb_3O_{10}$ nanosheets consisted of multiple grains with different in-plane orientations, its resistivity was only slightly higher than that of $SrRuO_3$ on single crystalline $SrTiO_3$, and residual resistivity ratios were comparable. In combination with the atomic scale roughness and well-controlled crystal structure, these results reveal the potential of using nanosheets to prepare artificial epitaxial heterostructures with $SrRuO_3$ bottom-electrodes, as nanosheets offer a high degree of control during PLD and remove the restriction of having to use specific substrates with matching lattice parameters.

5.4 Growth and properties of $SrRuO_3$ on $Ti_{0.87}O_2$

Optimization of growth of $SrRuO_3$ by deposition on two nanosheet layers Two consecutive Langmuir-Blodgett depositions were performed to coat a Si substrate with two layers of $Ti_{0.87}O_2$ nanosheets, of which the first layer covered 97.7 ± 0.8 % of the substrate, and the second layer covered 94.8 ± 0.9 % of that surface. An AFM image recorded after deposition of the second layer is shown in Figure 5.7a, where the height profile in the inset was obtained at one of the rare locations where the substrate was still exposed, and clearly reveals the two layers of nanosheets. The AFM image of Figure 5.7b was measured after PLD of $SrTiO_3$ and $SrRuO_3$, and shows that the surface morphology had coarsened by formation of *sub*-100 nm grains. Table 5.1 contains values resulting from XRR and XRD analyses of this sample and a $(110)_{\mathrm{pc}}$ oriented film of $SrRuO_3$ that was deposited under similar conditions on a single crystalline $SrTiO_3$ substrate.

Figure 5.8 shows XRD patterns of two samples where $SrTiO_3$ and $SrRuO_3$ were deposited under similar conditions, but on substrates that were covered by either one or two layers of $Ti_{0.87}O_2$ nanosheets. When just a single layer of nanosheets was used (covering 97.3 ± 0.2 % of the substrate), undesired crystallographic orientations were observed, which could not be suppressed by changing the PLD growth temperature between $650\,^{o}\mathrm{C}$ and $800\,^{o}\mathrm{C}$. Using a second layer of nanosheets led to complete suppression of undesired orientations and an over tenfold increase of the peak intensities of the preferred $(hh0)$ orientation, which is even more significant when considering that the monolayer of nanosheets consisted for $5 \pm 1\%$ of overlaps and stacks.

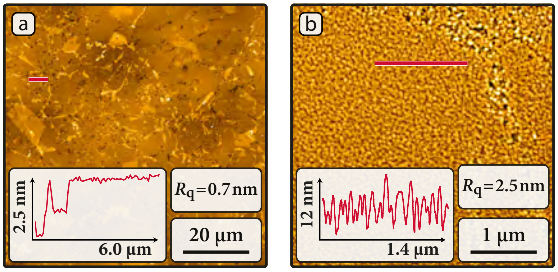

Figure 5.7: TM-AFM height images of $Ti_{0.87}O_2$ nanosheets on Si (a) after the second Langmuir-Blodgett deposition and (b) after PLD of $SrTiO_3$ and $SrRuO_3$. Both images include a value for the roughness (R_q) and a height profile measured along the (red) line in the corresponding image.

The second layer of nanosheets was required because at elevated temperatures the first layer reacted with the substrate and underwent partial structural transformations, impeding epitaxial growth of the perovskite film. These transformations did not involve long-range migrations of atoms, since no significant morphological changes were observed by AFM before and after heating a Si substrate containing a single layer of $Ti_{0.87}O_2$ nanosheets. X-ray photoelectron spectroscopy (XPS) was used to study changes of chemistry in the nanosheets and substrate by comparing the spectra of samples before and after thermal treatment, the results of which are displayed in Figure 5.9. Various changes were observed after heating a sample under deposition conditions. The intensity of the Si $2\mathrm{p}$ peak of silicon bound to oxygen (around a binding energy of $BE \approx 104$ eV) clearly increased compared to that of bare Si (around $BE \approx 100$ eV), which means that the originally native oxide grew at elevated temperatures. At the same time, the intensity of the O $1\mathrm{s}$ peak around $BE \approx 533$ eV did not show such increase, indicating that although the thickness of the SiO_x layer increased, x actually decreased. Small shifts to higher binding energy were observed in the Ti $2\mathrm{p}$ peaks ($\Delta BE = +0.13 \pm 0.02$ eV) while the O $1\mathrm{s}$ and Si $2\mathrm{p}$ peaks from the native oxide layer shifted to lower binding energies (the peaks shifted by $\Delta BE = -0.26 \pm 0.11$ eV and $\Delta BE = -0.25 \pm 0.07$ eV, respectively). No significant peak shifts were found for the O $1\mathrm{s}$ peak of the nanosheets and the Si $2\mathrm{p}$ peaks of the substrate, and no signs of formation of silicides were found. Also, no significant change of the atomic ratio in the titania nanosheets was found before and after heating. The spectral shifts indicate (small) changes of chemistry in the nanosheets and SiO_x layer, suggesting that the first layer of nanosheets may have been prone to formation of titanium silicates by reaction with the amorphous silicon oxide surface, provoked by the direct contact between the two.

Using two layers of $Ti_{0.87}O_2$ nanosheets instead of one did not only influence the crystallographic orientation, but also resulted in a smoother film (the roughness of the film on just a single layer of nanosheets was $R_\mathrm{q} = 3.9$ nm). Still, this film was significantly rougher than that discussed in the preceding section, which is attributed to the high surface energy of the $(110)_\mathrm{pc}$ planes of $SrRuO_3$, as discussed in the previous chapter. The roughness of $SrRuO_3$ on two layers of nanosheets was similar to that of the film deposited on a $(110)_\mathrm{c}$ oriented single

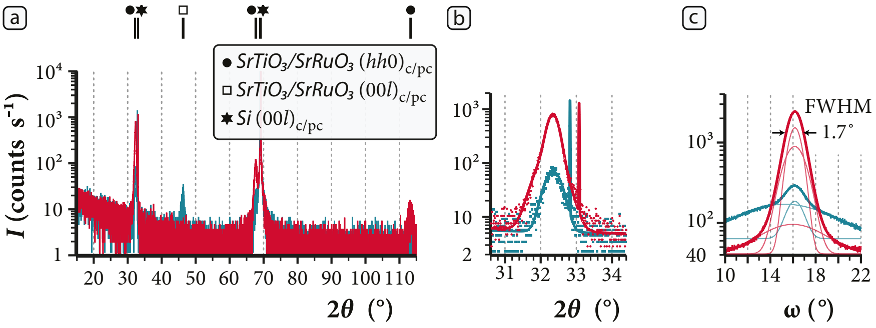

Figure 5.8: XRD patterns of films of $SrTiO_3|SrRuO_3$ on substrates covered with $Ti_{0.87}O_2$ nanosheets, including results from (a,b) $2\theta - \omega$ scans and (c) rocking ω around $2\theta = 32.35\,^{o}$. The red curves (the ones that show highest intensity around $2\theta = 32.35\,^{o}$) were obtained on a sample containing two layers of nanosheets, the blue curves were acquired from a sample containing just a single layer of nanosheets. The curve in image (b) was fitted to three Gaussian functions, where one was used to fit the peak of the Si substrate, and two to fit those of the film. The ω-rocking curves in image (c) are displayed together with Gaussian fits that were used to determine the FWHM (the value for the FWHM applies to both rocking curves).

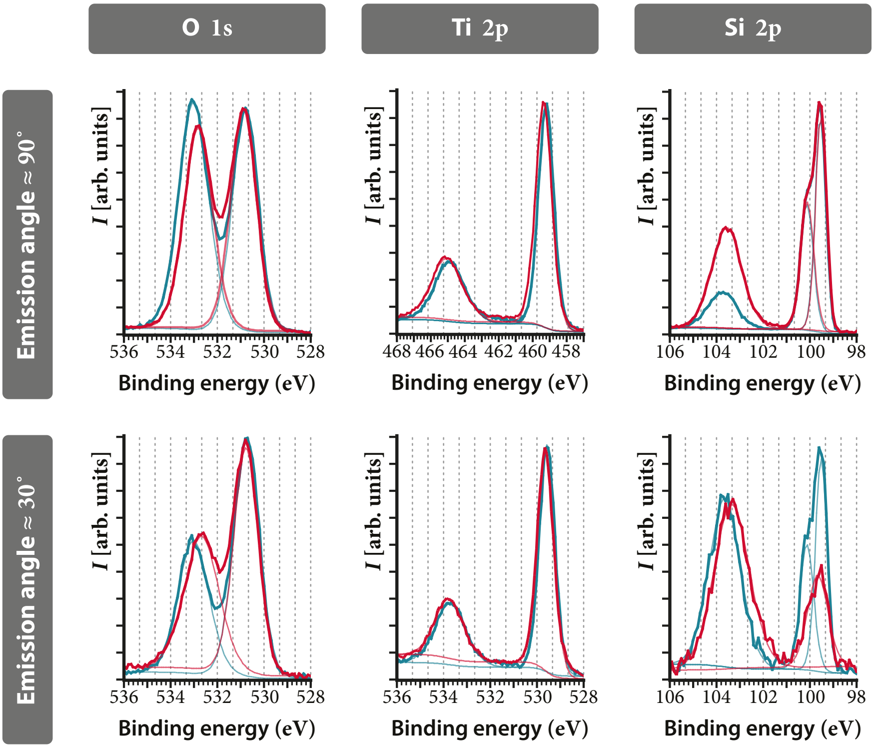

Figure 5.9: XPS spectra obtained from scanning two samples at two different emission angles around the O 1s, Ti 2p and Si 2p peaks. Both samples consisted of a single layer of $Ti_{0.87}O_2$ nanosheets on a Si substrate with oxide layer, of which one (in blue) was measured directly after Langmuir-Blodgett deposition of the nanosheets and the other (in red) after bringing the sample to deposition conditions.

crystalline $SrTiO_3$ substrate. Crystallographically these two films differed to a greater extent, since XRD studies on the fully oriented film indicated partial preservation of strain, as well as a smaller angular spread of the crystallographic orientation (rocking ω around $(110)_{\mathrm{pc}}$ yielded a FWHM of 0.04^o). Substantial lattice mismatch between the perovskite layers and $Ti_{0.87}O_2$ nanosheets (Table 4.2) lies at the basis of the reduced control of crystallographic orientation, and the absence of strain in these films.

MAGNETIC AND ELECTRICAL CHARACTERIZATION OF THE $(110)_{\mathrm{pc}}$ ORIENTED FILM

Magnetic and electrical characterization was performed on the film deposited on two layers of $Ti_{0.87}O_2$ nanosheets. The results can be found in Figure 5.10 and Table 5.1. Comparing the hysteresis curves measured in the two directions, almost equal coercivities ($H_{\mathrm{c}} = 1.0$ to $1.1 \cdot 10^6\ \mathrm{A\ m^{-1}}$) but different saturation and remnant magnetization were measured, which showed highest values when the field was applied in the surface plane. Compared to the film on $Ca_2Nb_3O_{10}$ nanosheets, the easy axis pointed in a different direction and the anisotropy appeared weaker. The latter observation can be explained by considering that the easy axis of the film on $Ti_{0.87}O_2$ nanosheets did have an in-plane component, meaning that the magnetostatic energy could never be completely minimized (since the in-plane orientation of the nanosheets could not be controlled). Evidently, the magnetic properties of the film on $Ti_{0.87}O_2$ nanosheets were different from those on $Ca_2Nb_3O_{10}$ nanosheets, illustrating the ability to manage material properties by using lattice matching nanosheets.

In contrast to the film on $Ti_{0.87}O_2$ nanosheets, the easy axis of the $SrRuO_3$ thin film on a single crystalline $(110)_{\mathrm{c}}$ oriented $SrTiO_3$ substrate was pointing out-of-plane (Figure 5.13). Rotation of the easy axis can be explained by differences in strain between the two films, as Jung and co-workers illustrated that the magnetic anisotropy and direction of the easy axis in films of $(110)_{\mathrm{pc}}$ oriented $SrRuO_3$ changed under the act of strain engineering.[20] Another difference between the film on nanosheets and that on single crystalline $SrTiO_3$, is that in the former case no signs of quantization of the magnetic spins were observed, while in the latter case $J = 4$ was found. In addition, although the room temperature resistivities of the two samples were of the same order of

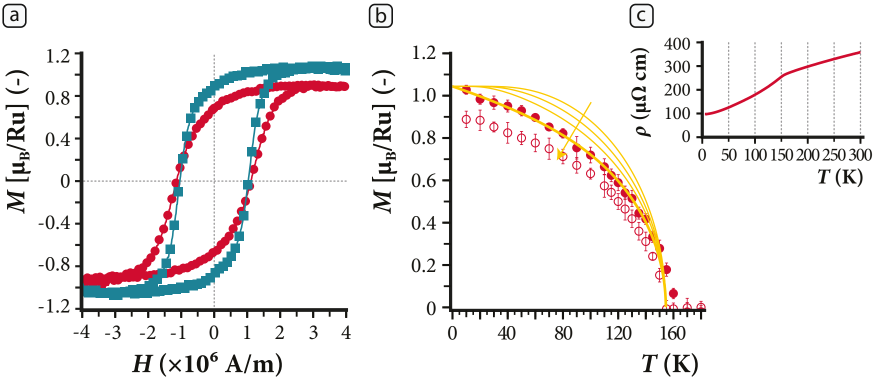

Figure 5.10: Magnetic and electrical characterization of the stack of $SrRuO_3$ on $SrTiO_3$ on two layers of $Ti_{0.87}O_2$ nanosheets supported on Si. Magnetic characterization includes (a) hysteresis curves measured at $10\ \mathrm{K}$ for the in-plane (blue squares) and out-of-plane (red circles) directions and (b) temperature dependence of saturation magnetization (closed circles) and remnant magnetization (open circles) when the field was applied in-plane. Similar as in Figure 5.6, Brillouin curves are displayed that resulted from the best fit (indicating $J = \infty$). Electrical characterization includes (c) the sheet resistivity of the sample plotted versus temperature.

magnitude, values diverged when the temperature was reduced, as clearly reflected by the higher residual resistivity ratio of the fully oriented film (Table 5.1). These differences possibly originate from the inferior crystallographic order of the film on nanosheets, as reflected by its multitude of grain boundaries and poorer film texture.

5.5 FILMS OF $SrRuO_3$ WITH MICROPATTERNED ORIENTATIONS

The preceding discussion illustrates the potential of nanosheets to control crystal nucleation, which not only provides a low-cost alternative to single crystalline substrates, but also an entirely new toolbox to locally tune the structural parameters and properties of thin films. To illustrate the latter concept, $Ca_2Nb_3O_{10}$ nanosheets were micropatterned on top of two layers of $Ti_{0.87}O_2$, and used to locally tailor the orientation of $SrRuO_3$. Crystallographic information of this film was obtained by EBSD, see Figure 5.11. The inverse pole figure maps in this figure indisputably prove the ability to control the crystal structure, since line patterns altering between an $(001)_{\mathrm{pc}}$ and $(110)_{\mathrm{pc}}$ orientation can clearly be recognized. Strong proof for epitaxy can be found in the maps containing the in-plane crystallographic information, in which the shapes and sizes of the different domains corresponded to those of the nanosheets.

A texture map showing misorientation from the ideal $[001]_{\mathrm{pc}}$ and $[110]_{\mathrm{pc}}$ directions is found in Figure 5.11e, from which clear differences in microtexture can be observed that are directly related to the control of crystal nucleation and growth that was achieved on the two types of nanosheets. The $(110)_{\mathrm{pc}}$ oriented part consisted of small subgrains that did not show any mutual correlation, which was caused by the significant mismatch between $Ti_{0.87}O_2$ and the perovskite film. In contrast, a more gradual change of orientation was indicated on the $(001)_{\mathrm{pc}}$ oriented film and intra-grain boundaries were observed in some of the (larger) domains. Note for instance the misorientation profile in Figure 5.11f that was made along a single $(001)_{\mathrm{pc}}$ oriented domain, which indicates coexistence of two subgrains having a boundary approximately halfway. This kind of microtexture may have originated from imperfections in the seed layer, like undulations or cracks of the nanosheets, but may have also developed during relaxation events.

The spatial Kerr maps in Figure 5.12 demonstrate that patterning of the orientations allowed local tuning of the magnetic characteristics of the film. At $78\ \mathrm{K}$, the complete film was ferromagnetic and the $(001)_{\mathrm{pc}}$ oriented lines showed highest magnetization of the two. Upon increasing the temperature, half of the material could be rendered paramagnetic, while the other $(110)_{\mathrm{pc}}$ oriented half remained ferromagnetic until $T_{\mathrm{C}} \approx 150\ \mathrm{K}$. These observations are corresponding with the measurements performed on the unpatterned thin films. For instance, dissimilar Curie temperatures were measured for the film on $Ca_2Nb_3O_{10}$ and $Ti_{0.87}O_2$ nanosheets (see Table 5.1). As most markedly recognized in the area enclosed by the dashed box, the paramagnetic lines still contained traces of ferromagnetic material. These erratic features shared their Curie temperature with the $(110)_{\mathrm{pc}}$ oriented lines, and appeared at the same location and with the same shape at $78\ \mathrm{K}$ by showing a lower magnetization than their surrounding. These observations strongly indicate that these regions actually contained $SrRuO_3$ oriented in the $[110]_{\mathrm{pc}}$ direction. Such deviations from the intended crystal orientation may have resulted from an incomplete coverage of $Ca_2Nb_3O_{10}$ nanosheets, as can also be discerned in the EBSD images. Note that the spot size of the modified Sagnac interferometer corresponded to $\sim 2\ \mu\mathrm{m}$, implying that the ferromagnetic features may appear larger than they actually were. Considering the overall picture, the magnetic characteristics of the patterned lines are matching well with those measured for the two thin films discussed in the previous sections, indicating that the deposition was not influenced by the act of patterning.

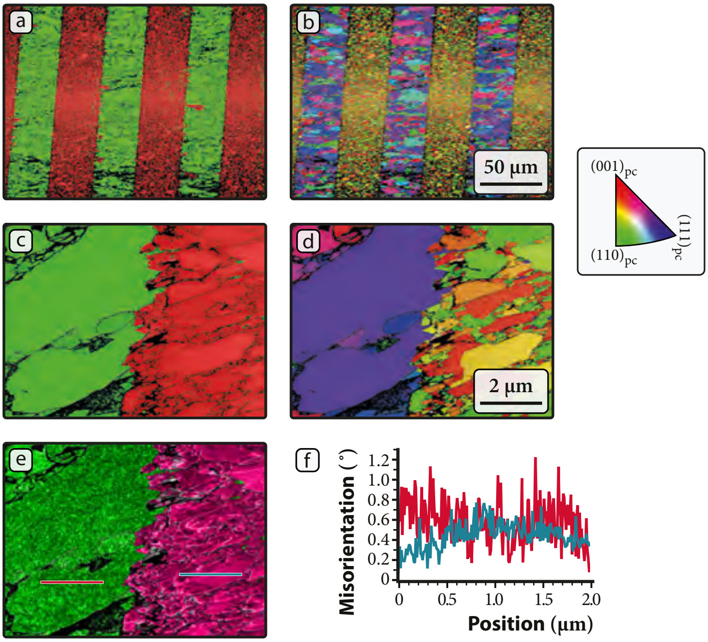

Figure 5.11: Inverse pole figure maps at (a,b) low (step size of $300\ \mathrm{nm}$); (c,d) high (step size of $10\ \mathrm{nm}$) magnification measured by electron backscatter diffraction (EBSD). For both magnifications, the orientation of the film is displayed from (a,c) the out-of-plane and (b,d) an in-plane perspective. (e) Out-of-plane texture map of the $(110)_{\mathrm{pc}}$ and $(001)_{\mathrm{pc}}$ oriented grains using a green and purple color gradient, respectively (both maps cover a total misorientation range of 1.5^o). (f) Misorientation profiles measured along the lines in the texture map (the color of the profiles and the lines along which they were measured are equivalent). The inverse pole figure maps are overlayed on the band contrast image whereas in the case of the texture map, the band contrast image is displayed only for the locations without solution. All maps are viewed as measured, without application of any form of noise reduction.

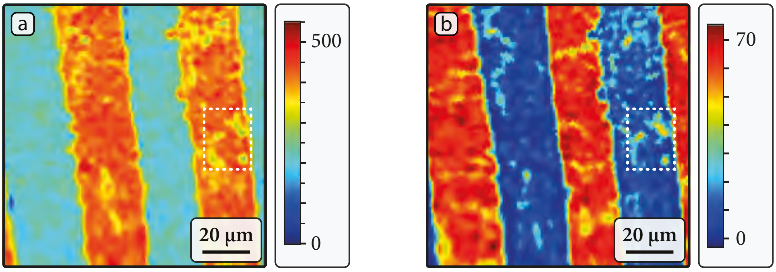

Figure 5.12: Spatial Kerr signal of $SrRuO_3$ with patterned orientations obtained by optical magnetometry at (a) $78\ \mathrm{K}$, and (b) $135\ \mathrm{K}$ after cooling the sample in a field of $0.2\ \mathrm{T}$. The values on the color scales are in $\mu\mathrm{rad}$, and both map scans show the same area.

5.6 CONCLUSIONS

Perovskite oxide thin films were deposited on Si substrates covered with inorganic nanosheets of $Ca_2Nb_3O_{10}$ or $Ti_{0.87}O_2$. These nanosheets were used as crystalline templates to control the nucleation of the films, which consisted of a $SrTiO_3$ buffer layer and a $SrRuO_3$ top layer. Films were $(001)_{\mathrm{pc}}$ oriented on $Ca_2Nb_3O_{10}$ nanosheets, and $(110)_{\mathrm{pc}}$ oriented on $Ti_{0.87}O_2$ nanosheets. The buffer layer of $SrTiO_3$ was introduced to decrease the roughness of the films on $Ca_2Nb_3O_{10}$ to the point where atomic steps could be recognized. At the elevated deposition temperatures, the first layer of $Ti_{0.87}O_2$ nanosheets reacted with the substrate, impeding control of nucleation of the perovskite film. This issue was resolved by adding a second layer of nanosheets to the substrate. Micropatterns of $Ca_2Nb_3O_{10}$ were fabricated on two layers of $Ti_{0.87}O_2$ nanosheets, which allowed us to locally control the structure and properties of a perovskite thin film.

Inorganic nanosheets can act as templates for growth of heteroepitaxial thin films on substrates that are unsuited for epitaxy by themselves. They allow to control the morphology, crystal structure, and properties of films to a nearly similar extent as can be achieved on lattice-matching substrates. Since growth can be mastered in the atomic limit by *in situ* monitoring of RHEED, nanosheets enable strain and interfacial engineering in similar ways as costly single crystalline substrates do. Their tunable lateral sizes and variable lattice parameters offer completely new pathways to tailor nucleation and growth on micrometer length scales. The control of topography, crystal structure, and properties illustrated in this chapter may serve as foundation for prospective work on all oxide heterostructures, as the atomically smooth thin films of $SrRuO_3$ are ideally suited for bottom electrodes. Besides, the whole new degree of freedom to locally tune the structural parameters, as illustrated by patterning the orientation of $SrRuO_3$ thin films, may have important implications in the design and realization of electronic or electromechanical devices.

REFERENCES

[1] A. Garg, Z. H. Barber, M. Dawber, J. F. Scott, A. Snedden, and P. Lightfoot. "Orientation dependence of ferroelectric properties of pulsed-laser-ablated $Bi_{4-x}Nd_xTi_3O_{12}$ films". *Appl. Phys. Lett.* **83** (12):2414–2416, 2003.

[2] A. Ohtomo and H. Y. Hwang. "A high-mobility electron gas at the $LaAlO_3/SrTiO_3$ heterointerface". *Nature*, **427** (6973):423–426, 2004.

[3] H. N. Lee, H. M. Christen, M. F. Chisholm, C. M. Rouleau, and D. H. Lowndes. "Strong polarization enhancement in asymmetric three-component ferroelectric superlattices". *Nature*, **433** (7024):395–399, 2005.

[4] H. Zheng, Q. Zhan, F. Zavaliche, M. Sherburne, F. Straub, M. P. Cruz, L. Q. Chen, U. Dahmen, and R. Ramesh. "Controlling self-assembled perovskite-spinel nanostructures". *Nano Lett.* **6** (7):1401–1407, 2006.

[5] E. Bousquet, M. Dawber, N. Stucki, C. Lichtensteiger, P. Hermet, S. Gariglio, J. M. Triscone, and P. Ghosez. "Improper ferroelectricity in perovskite oxide artificial superlattices". *Nature*, **452** (7188):732–736, 2008.

[6] J. Mannhart and D. G. Schlom. "Oxide interfaces–An opportunity for electronics". *Science*, **327** (5973):1607–1611, 2010.

[7] S. A. Chambers. "Epitaxial growth and properties of doped transition metal and complex oxide films". *Adv. Mater.* **22** (2):219–248, 2010.

[8] J. Ma, J. Hu, Z. Li, and C. W. Nan. "Recent progress in multiferroic magnetoelectric composites: From bulk to thin films". *Adv. Mater.* **23** (9):1062–1087, 2011.

[9] K. Kikuta, K. Noda, S. Okumura, T. Yamaguchi, and S. Hirano. "Orientation control of perovskite thin films on glass substrates by the application of a seed layer prepared from oxide nanosheets". *J. Sol-Gel Sci. Technol.* **42** (3):381–387, 2007.

[10] T. Shibata, K. Fukuda, Y. Ebina, T. Kogure, and T. Sasaki. "One-nanometer-thick seed layer of unilamellar nanosheets promotes oriented growth of oxide crystal films". *Adv. Mater.* **20** (2):231–235, 2008.

[11] H. Tetsuka, H. Takashima, K. Ikegami, H. Nanjo, T. Ebina, and F. Mizukami. "Nanosheet seed-layer assists oriented growth of highly luminescent perovskite films". *Chem. Mater.* **21** (1):21–26, 2009.

[12] T. Shibata, Y. Ebina, T. Ohnishi, K. Takada, T. Kogure, and T. Sasaki. "Fabrication of anatase thin film with perfect c-axis orientation on glass substrate promoted by a two-dimensional perovskite nanosheet seed layer". *Cryst. Growth Des.* **10** (8):3787–3793, 2010.

[13] T. Shibata, H. Takano, Y. Ebina, D. S. Kim, T. C. Ozawa, K. Akatsuka, T. Ohnishi, K. Takada, T. Kogure, and T. Sasaki. "Versatile van der Waals epitaxy-like growth of crystal films using two-dimensional nanosheets as a seed layer: orientation tuning of $SrTiO_3$ films along three important axes on glass substrates". *J. Mater. Chem. C*, **2** (3):407, 2014.

[14] M. Nijland, S. Kumar, R. Lubbers, D. H. A. Blank, G. Rijnders, G. Koster, and J. E. ten Elshof. "Local control over nucleation of epitaxial thin films by seed layers of inorganic nanosheets". *ACS Appl. Mater. Interfaces*, **6** (4):2777–2785, 2014.

[15] K. Taira, Y. Hirose, S. Nakao, N. Yamada, T. Kogure, T. Shibata, T. Sasaki, and T. Hasegawa. "Lateral solid-phase epitaxy of oxide thin films on glass substrate seeded with oxide nanosheets". *ACS Nano*, **8** (6):6145–6150, 2014.

[16] V. Nicolosi, M. Chhowalla, M. G. Kanatzidis, M. S. Strano, and J. N. Coleman. "Liquid exfoliation of layered materials". *Science*, **340** (6139):1226419–1226419, 2013.

[17] G. Koster, L. Klein, W. Siemons, G. Rijnders, J. S. Dodge, C. B. Eom, D. H. A. Blank, and M. R. Beasley. "Structure, physical properties, and applications of $SrRuO_3$ thin films". *Rev. Mod. Phys.* **84** (1):253–298, 2012.

[18] Q. Gan, R. A. Rao, C. B. Eom, J. L. Garrett, and M. Lee. "Direct measurement of strain effects on magnetic and electrical properties of epitaxial $SrRuO_3$ thin films". *Appl. Phys. Lett.* **72** (8):978–980, 1998.

[19] K. Terai, T. Ohnishi, M. Lippmaa, H. Koinuma, and M. Kawasaki. "Magnetic properties of strain-controlled $SrRuO_3$ thin films". *Jpn. J. Appl. Phys.* **43** (No. 2A):L227–L229, 2004.

[20] C. U. Jung, H. Yamada, M. Kawasaki, and Y. Tokura. "Magnetic anisotropy control of $SrRuO_3$ films by tunable epitaxial strain". *Appl. Phys. Lett.* **84** (14):2590–2592, 2004.

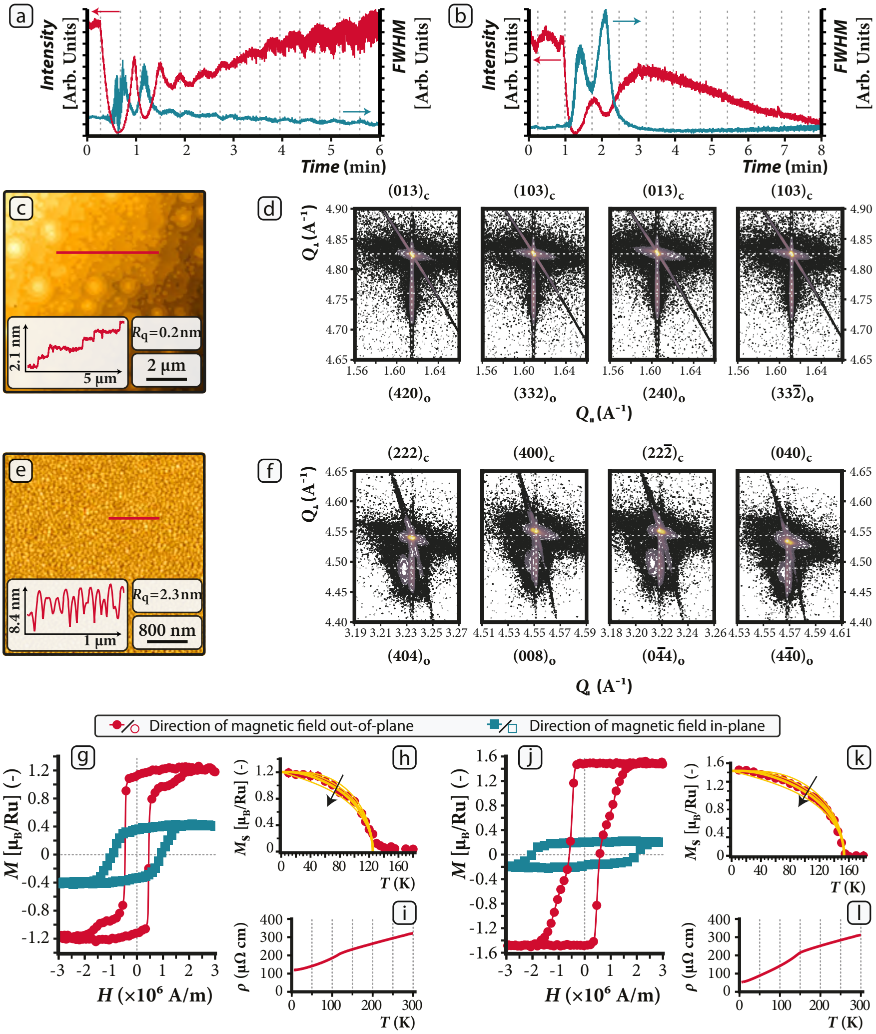

Figure 5.13: Analysis and characterization of fully oriented films of $SrRuO_3$ on $SrTiO_3$ $(001)_c$ and $(110)_c$, deposited under the same conditions as those on Si covered with nanosheets. Course of the intensity and FWHM of the RHEED specular spot during initial growth on a (a) $(001)_c$ oriented and (b) $(110)_c$ oriented substrate. (c) Topographical and (d) structural analysis of the $(001)_c$ oriented thin film by TM-AFM and XRD, respectively, and (e,f) similar analyses performed on the other film. The lattice parameters of the $(001)_c$ oriented film were refined to $a_O = 5.57$ Å, $b_O = 5.55$ Å, $c_O = 7.80$ Å, $\alpha = 89.9^o$, $\beta = 89.9^o$, $\gamma = 89.2^o$ and that of the $(110)_c$ oriented film to $a_O = 5.54$ Å, $b_O = 5.53$ Å, $c_O = 7.86$ Å, $\alpha = 90.6^o$, $\beta = 89.3^o$, $\gamma = 90.5^o$. Magnetic and electrical characterization of the (g-i) $(001)_c$ and (j-l) $(110)_c$ oriented films include (g,j) hysteresis loops measured at 10 K, (h,k) temperature dependence of saturation magnetization together with the best fit to Brillouin functions obtained when total angular momentum quantum number $J = 4$ (the different curves were obtained for $J = 1, 2, 4, \infty$, where J increases in the direction of the arrow), and (i,l) sheet resistivity versus temperature.

6

Towards Reaching Nanometer Resolution in Patterning Epitaxial Thin Films and Enable their Transfer onto Flexible Substrates

In the first section of this chapter, limits of the nanotransfer molding approach of chapter 2 are discussed, and two alternative approaches are proposed to aim for further miniaturization. When the aspect ratio of the patterns on the soft elastomeric mold were increased, different kinds of failure occurred, like collapsing, buckling or rupturing of these features. The first potential method that may yield smaller structures is to make stencil masks by infiltrating self assembled monolayers of polystyrene beads with a metal oxide precursor solution, and the second suggestion is to use hot embossing for obtaining the nanostructures. Only preliminary work is presented on these approaches, but both may lead to practicable methods to pattern sacrificial stencil masks with nanometer dimensions.

In the second half of this chapter, the idea of transferring oriented films onto polymeric substrates is presented. Nanosheets are in principle bound to the substrate by non-covalent bonds, but after PLD this bonding appeared too firm to realize lift-off by mechanical means. Still, nanosheets allow for growth of epitaxial films on many different substrates, and therefore sacrificial substrates were considered to support growth and facilitate transfer of thin films. Mica was used among other things, which is a material that can be cleaved along its layered structure, and is also thermally stable and inexpensive. Growth of epitaxial films and transfer onto polymeric substrates were both realized, but films blistered during cool down after growth. Nonetheless, the concept of transferring oriented thin films from thermally stable supports onto flexible substrates was illustrated, which may open new pathways for studying the behavior of such films upon bending and may lead to the application of epitaxial thin films in flexible electronics.

6.1 Limits of and alternatives to molded stencil masks

Patterns with periods down to $700\ \mathrm{nm}$ were fabricated and discussed in chapter 2, but further reduction of lateral sizes is desired for several reasons. One of these reasons is the ongoing pursuit of increasing the information densities in functional devices, like in (ferroelectric) memories.[1] Also from a more fundamental point of view further miniaturization is required, for instance to study and control physics resulting from confinement or substrate clamping effects. In addition, some types of experiments require patterns with nanometer dimensions. For example, the self-organization processes used to form epitaxial nanocomposites (like those discussed in chapter 3) may be controlled by pre-patterning a substrate.[2,3]

Various phenomena were observed that hindered further size reduction in stencil masks prepared by soft lithography. The transfer molded line patterns were made directly after the molds were peeled off the master, which was required to prevent lateral collapse of the features, typically observed a day after storing these molds in air (Figure 6.1a). Reducing the period to $600\ \mathrm{nm}$ led to immediate collapse, rendering these molds unusable. Due to the relatively low Young's modulus of PDMS ($\sim 2\ \mathrm{MPa}$), together with the high surface-to-volume ratio and associated high surface energy, pairing can be initiated already by the forces used when peeling the mold from the master.[4]

Also, attempts were made to pattern with molds having hexagonally ordered pillars, which, owing to the small lateral sizes in both dimensions, turned more challenging than transfer molding of line patterns. Indications of buckling (Figure 6.1b; note the asymmetric pore shapes and disordered periodicity) and

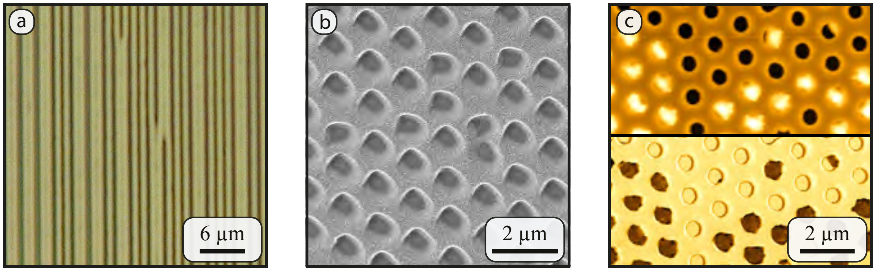

Figure 6.1: (a) Optical microscopy image of a mold containing a line pattern that appears disrupted at several locations because of lateral collapse. (b) HR-SEM image illustrating the effect of buckling on the final geometry of a ZnO stencil mask. (c) TM-AFM (top) height and (bottom) phase images of a patterned organometallic membrane on which fractured PDMS pillars can be recognized.

cohesive failure (Figure 6.1c) were regularly found for these zero dimensional patterns, and became more problematic when the aspect ratio ($^{height}/_{width}$) of the features was increased. Lateral collapse and buckling may be inhibited by using PDMS with a higher Young's modulus,[5,6] but features in this type of PDMS are more prone to fracture by the lower toughness compared to standard PDMS,[7] which is why experiments in this direction were not performed.

Instead of only focusing on soft lithographic techniques, two possible alternative routes were evaluated that could lead to further miniaturization. A first route involved using polystyrene (PS) nanospheres that self-assembled into hexagonally close packed mono- and multilayers during evaporation of the solvent of a commercially available colloid. Resulting self-assembled monolayers (SAMs) were infiltrated with solutions containing PAA and Zn^{2+}, were then exposed to toluene to remove the PS beads, and were finally annealed to form a porous network of ZnO. In a second route that was just briefly explored, a hard mold was used in a hot embossing step to pattern a film of PMMA directly onto a single crystalline substrate. This step was then followed by a second step that comprised negative replication of the pattern by deposition of ZnO, followed by lift-off of the PMMA structures. None of these routes did yet lead to a viable route for fabricating epitaxial nanostructures, but the initial work demonstrates the potential success of both approaches.

ZnO stencil masks made from SAMs of PS beads

The process of making ZnO stencil masks from self-assembled PS nanospheres with an average size of 199 ± 6 nm is schematically illustrated in Figure 6.2. A singly terminated $SrTiO_3$ substrates was cleaned by oxygen plasma (30 W for 4 min), and then covered with 1 μl of a $3\times$ dilution of a commercial colloid of

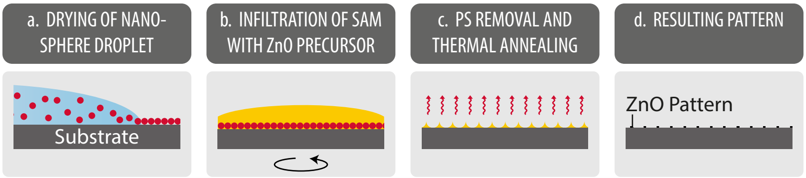

Figure 6.2: Schematical description of formation of nanostructured ZnO by utilizing SAMs of polystyrene spheres. (a) A substrate is covered with a droplet of the commercial colloid that is allowed to dry, forming self-assembled mono- and multilayers. (b) The ZnO precursor solution is then spin cast on top of the sample and cured on a hot stage. (c) The PS beads are then dissolved in toluene and the sample is heated under the conditions of Table 2.2 to form (d) ZnO.

nanospheres (1% w/w; catalog # 3200A; from Duke Scientific Corporation). Formation of SAMs was achieved at room temperature by allowing the film to dry in a petri dish ($\varnothing = 50$ nm) in which the air was saturated with water vapor; a process that typically took less than 5 min. The sample was then observed by optical microscopy, with which the number of layers and stacking faults could clearly be recognized. Stock solutions containing 0.05 g PAA and 0.197 g $Zn(NO_3)_2 \cdot 6\,H_2O$ in either water or ethanol (6 ml) were prepared, and spin cast using a similar sequence as that of Table 2.1, with the only difference that the sample was coated for 2 min at 5000 rpm. The sample was then placed on a heating stage that was heated from room temperature to $180\ ^{o}C$, on which it was left for 30 min. The polymeric nanospheres were then removed by dissolving them in toluene (99.0%; from Alfa Aesar), after which the sample was annealed in a microwave furnace using the sequence of Table 2.2.

By varying the solvent of the ZnO precursor solutions, the shape of the organometallic structures could be tuned. Using aqueous solutions led to an open nanostructured network (Figure 6.3a), indicating that the solution dewetted from the PS beads during solvent evaporation (the structures had a height of $h \approx 65$ nm). The pores were smaller in the case when ethanol was used as solvent (Figure 6.3c), suggesting that the nanospheres were completely wetted by the solution during the entire process of solvent evaporation ($h \approx 165$ nm, close to the diameter of the original PS spheres).

To confirm the tendency of the ethanol based solution to dry by forming a shell surrounding the PS beads, the experiment was repeated with a $4\times$ diluted ZnO precursor solution, resulting in a pattern as displayed in Figure 6.3e. The pattern had a similar height ($h \approx 150$ nm) as that made with the non-diluted solution. In addition to the circular pores, smaller triangular pores were found at the three-point boundaries in this case. Both the constant

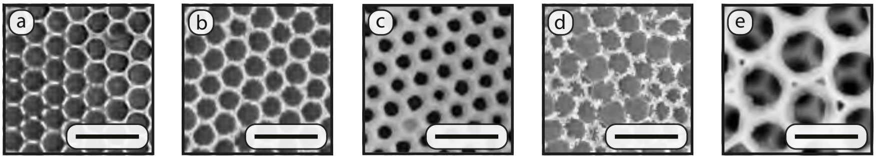

Figure 6.3: HR-SEM images (in-lens) of patterns made by infiltrating SAMs of PS beads with (a,b) aqueous and (c-e) ethanol based solutions of PAA and Zn^{2+}. These measurements were conducted after removal of the nanospheres, both (a,c,e) before and (b,d) after annealing. The scale bars of the first four images correspond to a distance of 500 nm, while the last image has a scale bar of 200 nm.

height and triangular pores form strong indications that the PS beads were entirely wetted during evaporation of the solvent. Also note the opal structure in Figure 6.3e, which was obtained on a location that originally contained a double layer of self-assembled beads. Such double layers can potentially lead to fabrication of epitaxial nanostructures that are significantly smaller than the size of the nanospheres.

After annealing the samples, the original shape of the pattern made from the aqueous solution was preserved (Figure 6.3b) without showing significant shrinkage in any direction ($h \approx 50$ nm). This result is in clear contrast with the pattern made from a solution in ethanol (Figure 6.3d), which had shrank and ruptured after annealing ($h_{\text{average}} \approx 20$ nm). The observed strong differences are explained by the deviant wetting behavior, as drying of the ethanol based solution (compared to the aqueous one) led to less compaction of the organometallic material and formation of a weak spot at the hemispheres of the beads (due to the direct contact between beads midway their heights). Relating these observations to the aim of the present work, using aqueous solutions results in nanostructured ZnO that appears to be most promising for utilization as stencil masks. In essence, this method is experimentally very simple and may allow bottom-up fabrication of epitaxial nanostructures, but its downside is that the shapes of these nanostructures are limited as they are defined by the SAMs.

ZnO STENCIL MASKS MADE BY HOT EMBOSSING

Another possible route to fabricate ZnO stencil masks with nanoscale dimensions is schematically described in Figure 6.4. A layer of PMMA was spin coated onto TiO_2 terminated $SrTiO_3$ at 4000 rpm for 50 s (the commercial solution was the same as that used for chapter 2, and added during a spin-on stage at 500 rpm for 10 s). The film was then cured for 2 min on a hot plate that was pre-heated at 160 °C. Nano-imprint lithography (NIL) was used to transfer pat-

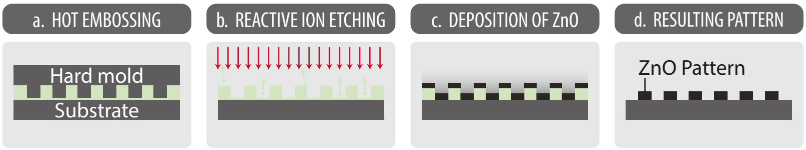

Figure 6.4: Schematic description of steps taken as an attempt to fabricate stencil masks of ZnO by (a) hot embossing of PMMA, followed by (b) reactive ion etching to remove any residual layer and (c) deposition of ZnO, of which (d) nanostructures may be obtained after lift-off.

terns from an imprint template into the PMMA film. The template contained circular pores having depths of ~ 120 nm and diameters ranging from 80 to 200 nm, separated by the same or double amounts. The process was carried out with an Eitre NIL system (from Obducat) at 195 °C for 18 min, in the course of which the pressure was increased from 0 to 40 bar, 3 min after the temperature was reached (the stack was demolded after the temperature dropped below 50 °C). A parallel plate reactive-ion etching (RIE) system (home-built) was used to remove (part of) the residual layer (using a power of 10 W for 30 s in an O_2 background gas of 0.20 mbar).

A typical pillar structure that resulted from the imprint step is shown in Figure 6.5, which was recorded after a short RIE step to remove parts of the residual layer. Still, some traces of PMMA were left in the recessed parts, but as long as a continuous mask of ZnO can be formed that is sufficiently fixed to the substrate (so that it will not detach during subsequent processing), small residual material in this step will not necessarily hinder the intended fabrication of epitaxial nanostructures.

Efforts to fabricate stencil masks from these patterns were limited to a single attempt, during which PLD was used to deposit approximately 25 nm ZnO at room temperature, and acetone was used to aim for lift-off of the sacrificial polymer. The laser was focused on a homemade polycrystalline target of ZnO to a spot size of 1.5 mm^2, and was fired at 1 Hz for 20 min reaching an energy density of 2.5 J cm^{-2} on the target. Target-to-substrate distance was 6 cm, and O_2 was used to reach a pressure of 0.001 mbar. This attempt was unsuccessful, as AFM studies indicated that the patterns had partly collapsed during PLD, and almost all material was removed from the substrate after putting the sample in a beaker containing acetone.

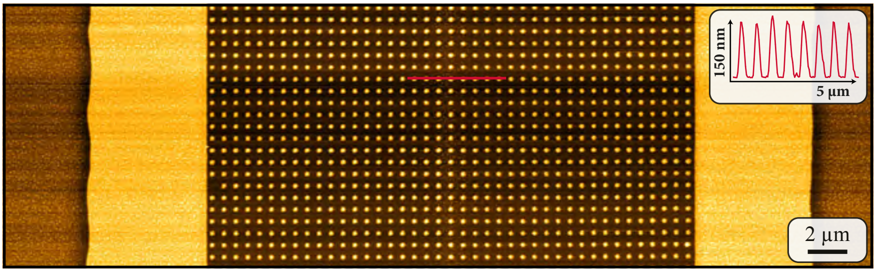

Figure 6.5: TM-AFM height image of PMMA on singly terminated $SrTiO_3$, after NIL and RIE.

The drawbacks of using soft elastomeric molds do not apply to hot embossing with a hard mold, and therefore further miniaturization of the patterns could be realized. The resulting structures in PMMA were not successfully translated into a ZnO stencil mask though, and further experiments are required to evaluate the applicability of NIL for fabricating thermally stable stencil masks. Either the PLD conditions should be optimized, or alternative methods should be sought to deposit a sacrificial metal oxide. In this context, a solution based process may for instance be considered to infiltrate the PMMA nanostructures with a metal oxide precursor.

6.2 PROSPECTS OF NANOSHEETS FOR TRANSFERRING ORIENTED FILMS TO FLEXIBLE SUBSTRATES

In the two preceding chapters, perovskite oxide heteroepitaxy was demonstrated on arbitrary substrates by covering these substrates with crystalline nanosheets having the appropriate lattice parameters. New possibilities stem from such seed layers, like the capability to pattern the orientation and properties of a thin film, as discussed in chapter 5. Epitaxial growth of perovskites was once restricted to a small set of single crystalline substrates, but since this constraint is now lifted, one has become virtually free to choose between many different substrates. The major condition for successful growth is that the nanosheets and substrate should be stable under the deposition conditions, which, in the case of PLD, means that they should resist temperatures that are generally above $500\,^{\circ}\mathrm{C}$.

Polymeric substrates are generally inexpensive, of light weight, chemically robust, and bendable. They play an important role in current technological developments for application in flexible electronics like solar cells,[8] piezoelectric energy harvesting systems,[9,10] and wearable or implantable sensors.[11] On the other hand, several hundred degrees cause these substrates to deform, melt, or decompose, rendering them incompatible with high temperature depositions. A general method to place oriented perovskite layers on thermally unstable substrates remains lacking, while such a method is in demand as it will allow studying the performance of these films upon bending and working towards their application in flexible electronics. Using a thermally stable support during film growth and transferring these films onto flexible substrates in a second step may be a way to attain such a method deviously, where nanosheets may be used

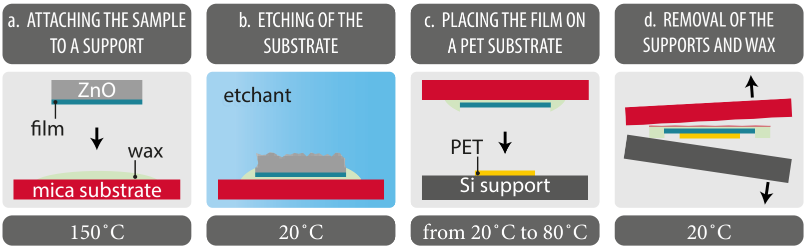

Figure 6.6: Schematic representation of the method that was followed to transfer epitaxial films from ZnO to PET substrates. The different steps are briefly described above the images, and the temperatures at which these steps were performed are given below the images. Additional experimental details are provided in the main text.

to control the crystal orientation of these films. The transfer may either be realized by using (inexpensive) sacrificial substrates that can be etched under mild conditions, or by pealing the film and substrate apart. Both approaches were explored.

Experimental methods for transferring thin films

The exfoliation and deposition of nanosheets was carried out using methods similar to those described in chapter 4. Besides on silicon, Langmuir-Blodgett depositions were performed on copper, (0001) zinc oxide, $(11\bar{2}0)$ sapphire, and phlogopite mica grade V-1 substrates, obtained from Goodfellow Cambridge Limited, Crystec $(2\times)$, and SPI Supplies, respectively. Prior to depositing the nanosheets, some of the mica substrates were annealed in a tube furnace (Nabertherm) at $700\,^\circ\mathrm{C}$ under ambient conditions for 24 h. Also just before PLD, these substrates were annealed at $700\,^\circ\mathrm{C}$ inside the vacuum chamber at base pressure, for a duration of 45 min or 3 h dependent on whether or not these substrates were already annealed in the tube furnace.

PLD was carried out under the conditions described in chapter 5, except that a spot size of $2.5\ \mathrm{mm}^2$ was used and that both $SrTiO_3$ and $SrRuO_3$ were deposited for 15 min. After depositing $SrRuO_3$, a third layer of $BiFeO_3$ was deposited from a target containing bismuth in an excess of $10\,\%$ (Praxair electronics). In this case, the laser fluence was controlled at $2.4\ \mathrm{J\,cm^{-2}}$ and depositions were carried out at 0.5 Hz for 60 min in 0.30 mbar O_2. Detailed analysis and characterization of this film is not provided, since the main focus is on the different attempts to transfer these films onto flexible substrates.

Films that were deposited on ZnO were transferred to poly(ethylene tereph-

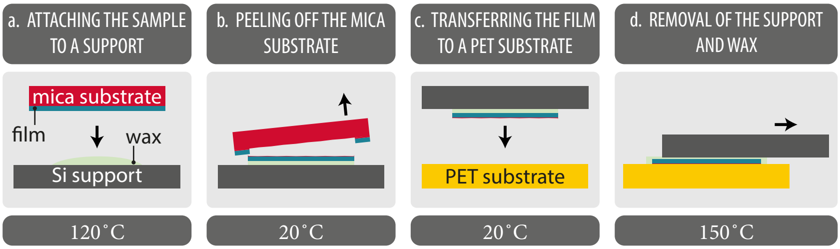

Figure 6.7: Schematical representation of the method to transfer thin films from mica to plastic substrates, where the experiments are briefly described above the images and the temperatures are given below.

thalate) (PET) substrates (supplied by Sigma Aldrich) by following the procedure of Figure 6.6. The film was placed upside down in a layer of molten wax (Quickstick 135 mounting wax) on a mica substrate, which was heated on a hot plate at $150\,^{\circ}\mathrm{C}$ and then cooled to room temperature. The sample was then immersed in an excess of aqueous hydrochloric acid ($0.5\ \%\ {}^{v}/_{v}$) until the substrate was completely etched (several days). The downside of the film was then rinsed with water and ethanol, dried in a stream of N_2 gas, and applied on the PET substrate supported by a large piece of silicon. The plastic substrate was smaller than the film in order to prevent wax from leaking in between the two parts. The wax was softened by heating the stack on a hot plate at $80\ ^{\circ}\mathrm{C}$, while the center of the film was pressed down firmly onto the PET substrate. The stack was allowed to cool to room temperature again, after which the supports (mica and silicon) were carefully removed. The wax with mica residues was removed by rinsing with acetone, which was followed by rinsing with ethanol and drying with N_2 gas.

Films on mica substrates were transferred by mechanical cleavage within the substrate, of which the different steps are displayed schematically in Figure 6.7. The film was attached onto a silicon support containing wax that was softened at $120\ ^{\circ}\mathrm{C}$ and subsequently allowed to cool to room temperature. No wax was applied near the edges of the film, so that the substrate could be peeled off while minimizing the amount of residual mica left on the thin film. The downside of the film was then applied on a PET substrate (having a larger size than the film), the wax was then molten and the silicon support was carefully removed by sliding it over the flexible substrate. The plastic substrate was then cooled to room temperature and residual wax was removed by rinsing in acetone, after which the sample was further rinsed with ethanol and dried in a stream of N_2.

Nanosheets were found to be loosely bound to their substrates after Langmuir-Blodgett depositions, which was attributed to the presence of interfacial tetra-*n*-butylammonium cations that adhered to the nanosheets to compensate their charges. The alkyl chains attached to the substrates by Van der Waals forces only, and prevented close contact between these substrates and the nanosheets. After decomposing the organic compound by thermal annealing or irradiation of the samples by UV light (for $24\ \mathrm{h}$ with an effective energy density of $56\ \mathrm{mW\ cm^{-2}}$), the nanosheets could no longer be mechanically separated from their substrates by using adhesives, regardless whether Si, Cu, ZnO, or Al_2O_3 substrates were used. The increased bonding strength may be attributed to electrostatic interactions between the nanosheets and partial charges on the surface of the substrate, hydrogen bonds between substrate oxygen atoms and the interfacial ions (possibly ${NH_4}^+$),[12] or even covalent bonds like formation of silicates as discussed in chapter 5. Additional prove for clamping can be obtained by high temperature XRD measurements after PLD. For instance, clamping on a substrate of low thermal expansion, like Si ($\alpha = 3.8 \cdot 10^{-6}\ \mathrm{K^{-1}}$), will suppress the in-plane expansion of a film and consequently induce a larger out-of-plane expansion. A film of $SrTiO_3$ was deposited on a Si substrate containing a single layer of $Ca_2Nb_3O_{10}$ nanosheets and indeed appeared to be clamped, as the out-of-plane thermal expansion coefficient of this film ($\alpha = 15.7 \cdot 10^{-6}\ \mathrm{K^{-1}}$) was larger than that of a single crystalline substrate of $SrTiO_3$ ($\alpha = 10.8 \cdot 10^{-6}\ \mathrm{K^{-1}}$). Apparently, films on nanosheets can not simply be removed from their substrate by mechanical means, as even without growing a film and by using substrates that are considered stable at their surfaces,[13] lift-off could not be effected.

One way to overcome the challenge to detach the epitaxial thin films from their substrates is to use sacrificial ones, which are preferably inexpensive and etched under mild conditions. To evaluate the feasibility of this concept, oriented films were deposited on ZnO substrates that were covered with nanosheets, and these films were then transferred onto flexible PET substrates, as confirmed by XRD and AFM. Still, ZnO substrates are costly and thus do not seem to be of use for practical applications, creating the demand for alternative substrates. Though many metals are relatively inexpensive and easily etched, severe oxidation generally occurs when heating these substrates. Such degradation was experimentally verified under PLD conditions for Cu substrates covered with nanosheets.

Mica crystals exhibit a layered structure with interlayer cations that enable cleavage of separate layers, and are additionally inexpensive and thermally stable. For these reasons, substrates of this material were used to support the growth of oriented films on nanosheets, and selected for the ease of tearing them off the grown films. General concern of using natural phlogopite mica substrates is that non-structural water is entrapped between the silicate layers, which is responsible for the anomalously high thermal expansion of these materials.[14] The entrapped water led to substantial blistering in the final stage of cooling, even when low cooling rates of $1\ ^{\circ}\mathrm{C\ min}^{-1}$ were used. Blistering also hindered successful film transfer, since films were no longer intact and wax could creep in between fractions of these films and the PET substrates. The magnitude of blistering could be reduced by annealing the substrates prior to PLD, but flaking could never be completely suppressed.

AFM height images after PLD and after transfer are displayed in Figure 6.8a and b, respectively. Apart from the cracks that had formed during cooling, a smooth film was obtained after PLD, of which the roughness was $R_\mathrm{q} = 0.3\ \mathrm{nm}$ on the level of single nanosheets. After transferring this film to a PET substrate, its morphology remained largely intact, but the roughness of the film on the nanosheets increased to $R_\mathrm{q} = 0.8\ \mathrm{nm}$. EBSD was used to confirm the transfer of an oriented film, the results of which are displayed in Figure 6.9. These results clearly demonstrate that mechanical cleavage within mica substrates is a route that allows the transfer of oriented films, since a single out-of-plane

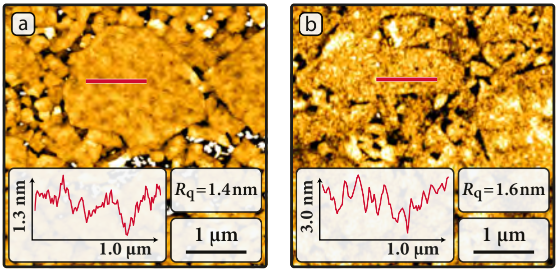

Figure 6.8: TM-AFM height images of a thin film of $\mathrm{BiFeO_3|SrRuO_3|SrTiO_3}$ on $\mathrm{Ca_2Nb_3O_{10}}$ nanosheets (a) after growth on a mica substrate and (b) after its transfer to a flexible plastic substrate. The insets of both images contain a value for the root mean square roughness (R_q), and a height profile obtained along the red lines.

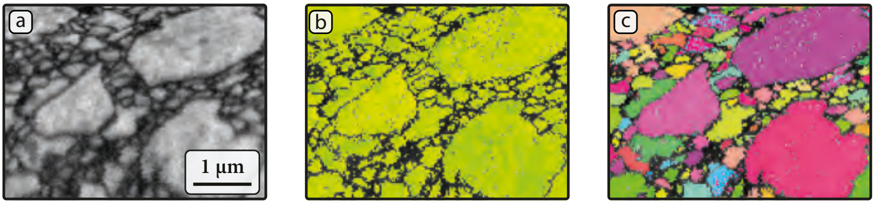

Figure 6.9: EBSD images showing the (a) band contrast and inverse pole figure maps in the (b) out-of-plane and (c) in-plane directions of a film of $BiFeO_3|SrRuO_3|SrTiO_3$ on $Ca_2Nb_3O_{10}$ nanosheets after its transfer onto a PET substrate.

orientation was measured. In addition, the domains shared their shapes and sizes with those of the nanosheets, pointing to an epitaxial relation on the level of individual nanosheets (Figure 6.9c).

Nanosheets allow for growth of thin films in preferred crystallographic orientations on substrates that do no longer require to have matching lattice parameters. They therefore offer new possibilities to engineer functional structures on a wide range of substrates. This ability also yields new prospects to transfer epitaxial thin films to polymeric substrates, which is relevant for studying the behavior of these films when bended and applying them in flexible electronics. The nanosheets were in principle attached to the substrate by non-covalent bonds only. However, after heating the samples to temperatures that are typically used during PLD, the bonding appeared too firm to be broken just by mechanical means. Here, a sacrificial mica substrate was used that could later be removed by cleaving it along its layers, but blistering of these film could never be prevented and requires further optimization. Also plenty of alternative routes to lift-off thin films may still be exploited. For instance, metals may be coated with anti-corrosion layers to prevent their oxidation during PLD, or sacrificial layers can be used to support the nanosheets. These supports may be removed after growth to separate the epitaxial films from their substrates.

References

[1] W. Lee, H. Han, A. Lotnyk, M. A. Schubert, S. Senz, M. Alexe, D. Hesse, S. Baik, and U. Gösele. “Individually addressable epitaxial ferroelectric nanocapacitor arrays with near $\mathrm{Tb\,inch^{-2}}$ density”. *Nat. Nanotechnol.* **3** (7):402–407, 2008.

[2] R. Comes, H. Liu, M. Khokhlov, R. Kasica, J. Lu, and S. A. Wolf. "Directed self-assembly of epitaxial $CoFe_2O_4$ - $BiFeO_3$ multiferroic nanocomposites". *Nano Lett.* **12** (5):2367–2373, 2012.

[3] N. M. Aimon, H. K. Choi, X. Y. Sun, D. H. Kim, and C. A. Ross. "Templated self-assembly of functional oxide nanocomposites". *Adv. Mater.* **26** (19):3063–3067, 2014.

[4] E. Delamarche, H. Schmid, B. Michel, and H. Biebuyck. "Stability of molded polydimethylsiloxane microstructures". *Adv. Mater.* **9** (9):741–746, 1997.

[5] T. W. Odom, J. C. Love, D. B. Wolfe, K. E. Paul, and G. M. Whitesides. "Improved pattern transfer in soft lithography using composite stamps". *Langmuir*, **18** (13):5314–5320, 2002.

[6] D. Qin, Y. Xia, and G. M. Whitesides. "Soft lithography for micro- and nanoscale patterning". *Nat. Protoc.* **5** (3):491–502, 2010.

[7] K. M. Choi and J. A. Rogers. "A photocurable poly(dimethylsiloxane) chemistry designed for soft lithographic molding and printing in the nanometer regime". *J. Am. Chem. Soc.* **125** (14):4060–4061, 2003.

[8] G. Li, R. Zhu, and Y. Yang. "Polymer solar cells". *Nat. Photonics*, **6** (3):153–161, 2012.

[9] R. Yang, Y. Qin, L. Dai, and Z. L. Wang. "Power generation with laterally packaged piezoelectric fine wires". *Nat. Nanotechnol.* **4** (1):34–39, 2009.

[10] Y. Qi, N. T. Jafferis, K. Lyons Jr, C. M. Lee, H. Ahmad, and M. C. McAlpine. "Piezoelectric ribbons printed onto rubber for flexible energy conversion". *Nano Lett.* **10** (2):524–525, 2010.

[11] M. C. McAlpine, H. Ahmad, D. Wang, and J. R. Heath. "Highly ordered nanowire arrays on plastic substrates for ultrasensitive flexible chemical sensors". *Nat. Mater.* **6** (5):379–384, 2007.

[12] M. Osada, K. Akatsuka, Y. Ebina, H. Funakubo, K. Ono, K. Takada, and T. Sasaki. "Robust high-κ response in molecularly thin perovskite nanosheets". *ACS Nano*, **4** (9):5225–5232, 2010.

[13] Y. Golan, P. Fini, S. P. DenBaars, and J. S. Speck. "Substrate reactivity and "controlled contamination" in metalorganic chemical vapor deposition of GaN on sapphire". *Jpn. J. Appl. Phys., Part 1*, **37** (9 A):4695–4703, 1998.

[14] F. G. Karioris, L. Cartz, G. Hishmeh, X. Yang, and C. Templier. "Mica/gas composites as thermal actuators". In: *Proceedings of SPIE - The International Society for Optical Engineering*. 1993, 255–265.

SUMMARY

The perovskite class encompasses a multiplicity of oxide materials with widely divergent properties and many potential applications. The similar unit cell dimensions and common oxygen octahedral backbone of the different perovskites allow stacking their building blocks on top of each other in a structurally ordered fashion. In the form of such heteroepitaxial thin films, properties can be fully exploited and manipulated under the act of strain or interfacial engineering. Pulsed laser deposition (PLD) is exceedingly suitable for growing artificial films of perovskite-type oxides, where single crystalline substrates with matching lattice parameters are required to completely dictate the crystal orientation. The technique allows manipulating material at a unit cell level in the direction of film growth, but lacks standardized approaches to control the deposition in other directions. Such lateral control is indispensable for future device integration, but particularly complicated by the elevated substrate temperatures that are required for the adatoms to reorganize into an energetically favorable configuration.

In this thesis, different routes are introduced that are compatible with PLD and enable parallel patterning of epitaxial perovskite heterostructures on micrometer length scales and below. Patterns were made either by selective-area epitaxial growth of a perovskite oxide or by locally tailoring the crystal orientation of a thin film. Regarding the first option of patterning a material, sacrificial micro- or nanostructures were used to screen parts of a single crystalline substrate and permit epitaxial growth of a perovskite on particular areas only. Regarding the second option of patterning the crystal orientation, inorganic nanosheets with different lattice parameters were combined on a single substrate to locally tailor the nucleation and growth of a thin film that was deposited on top. Most of the different approaches to pattern epitaxial thin films did not interfere with the unprecedented control of growth that can be achieved with

PLD, since properties were measured that are reminiscent of well-oriented thin films. Simultaneously, properties were influenced by the patterns and showed to clearly depend on the position or direction of a measurement, reflecting the potential use of these patterned heterostructures for different electronic and electromechanical applications.

A first approach to pattern heteroepitaxial perovskite-type oxide materials combines soft lithographic molding with PLD. This approach consists of two consecutive bottom-up fabrication steps, started by molding sacrificial ZnO stencil masks on single crystalline substrates, and followed by PLD to form negative and heteroepitaxial replicas. Micro molding in capillaries (MiMiC) and transfer molding were used complementary to cover both the micrometer and nanometer lateral size ranges, and both methods allowed fabrication of residue-free patterns of ZnO with high fidelity over the entire area of the substrate. ZnO was used because of its compatibility with the high temperatures reached during PLD and because of the ease of its removal after use by benefiting from its amphoteric nature. *Sub*-micrometer sized lines of $La_{0.67}Sr_{0.33}MnO_3$ were made by the transfer molding approach, in which the anisotropic features expected for a fully oriented thin film were preserved and a magnetostatic contribution from the line shapes was introduced. Different patterns of $SrRuO_3$ were made with lateral dimensions of a few micrometers, for which electrical isolation was illustrated. Both molding approaches did not compromise in the control of growth that is generally achieved for unpatterned films, as surface morphology, RHEED patterns, crystal structure, and magnetic properties of patterned and unpatterned films were comparable. The bottom-up soft lithographic methods can be compliantly utilized for making epitaxial structures of various shapes and sizes in the $\mu\mathrm{m}$ down to the nm range, and offer unique opportunities for fundamental studies as well as for realizing technological applications.

Restrictions that are inherent to using soft elastomeric molds limit the aspect ratio of the stencil masks, and as a consequence only planar epitaxial features can be obtained. Applications like catalysis or gas sensing require the functional materials to have high surface areas, and thus ask for other approaches for patterning. An approach that was explored makes use of mixed targets consisting of $PbZr_{0.2}Ti_{0.8}O_3$ and ZnO to form self-organized heteroepitaxial nanostructures. By carefully controlling the deposition conditions, ferroelectric nanopillars were formed with periodicities of approximately $40\ \mathrm{nm}$. Increasing the repetition rate of the laser pulses or the O_2 partial pressure led to reduced lateral sizes of the patterns, accompanied by a change of the morphology from a pillars-and-matrix-like pattern into a maze structure where both phases were meandering through the films. Etching ZnO led to an increase of the tetragonality of the nanostructures of $PbZr_{0.2}Ti_{0.8}O_3$, indicating that both phases were coherently coupled and strain was of elastic origin. The electromechanical response of the nanopillars was found to increase upon removal of the matrix, but fell behind that predicted for a single domain and bulk single crystal of $PbZr_{0.2}Ti_{0.8}O_3$. Still, the high surface area and epitaxial nature of these nanostructures may offer distinct advantages over thin film or bulk counterparts, and the work may act as model for growth of other perovskite/ZnO composites that can potentially be applied in other fields.

Instead of patterning materials, thin films with position dependent properties can be made by locally controlling the crystallographic orientation. As reported in this thesis, nanosheets can be a unique tool to control the nucleation of films on a level that can not be attained on single crystal substrates. Inorganic nanosheets of $Ca_2Nb_3O_{10}$ and $Ti_{0.87}O_2$ were placed on silicon substrates and used to control the nucleation of $SrRuO_3$ during growth by PLD. The underlying nanosheets determined both the morphology and crystallographic orientation of the films, and $SrRuO_3$ preferentially grew in different directions on the two types of nanosheets. Epitaxial growth was demonstrated and explained by lattice matching with the underlying nanosheets together with continuation of the oxygen octahedral backbones. The nanosheets had a clear effect on the magnetic properties of the films, which showed anisotropic behavior only when a seed layer of nanosheets was used. The crystallographic orientation of $SrRuO_3$ was locally controlled by depositing this material on a single layer that comprised both types of nanosheets, which suggests that nanosheets can be used to deposit films with position dependent properties.

Several ways were introduced to master film growth of $SrRuO_3$ on top of the two-dimensional seed crystals. When deposited on a layer of $Ca_2Nb_3O_{10}$, the roughness of these films was reduced down to the atomic-scale by introducing a buffer layer of $SrTiO_3$. A stack of two layers of $Ti_{0.87}O_2$ nanosheets was required to obtain a film of $SrRuO_3$ that was well oriented, because the first layer of nanosheets reacted with the substrate at the elevated deposition temperatures. The films had resistivities close to those measured for fully oriented ones, and showed magnetic anisotropy with the easy axis and Curie temperature determined by the underlying nanosheets. The two types of nanosheets were patterned to locally tailor the crystallographic orientation and properties of $SrRuO_3$. An unprecedented control of perovskite film growth on Si substrates was illustrated, and the methods that were developed to deposit $SrRuO_3$ thin films are a viable starting point for growth of artificial heteroepitaxial thin films that require a bottom electrode. Control was not just reached in the direction of film growth, as the crystal orientation was regulated laterally on the surface of micropatterned nanosheets. The concept of being able to pattern the orientation and properties of thin films creates new prospects for fabricating heterostructures that may find use in future generation devices.

This thesis is concluded with an outlook, containing preliminary results that sprang from the work presented in the preceding chapters. Limits of the nanotransfer molding method are discussed, and two alternative approaches are proposed to aim for further miniaturization. In addition, the concept of transferring oriented films from thermally stable supports onto flexible substrates is illustrated. This ability may open new pathways for studying the behavior of such films upon bending and may lead to the application of epitaxial thin films in flexible electronics.

SAMENVATTING

De perovskiet groep bevat een verscheidenheid aan oxidische materialen met sterk uiteenlopende eigenschappen en veel potentiële toepassingen. De overeenkomstige dimensies van de eenheidscellen en gemeenschappelijke achtvlakkige zuurstof structuur van de verschillende perovskieten maakt het mogelijk hun bouwstenen op een geordende manier te stapelen. In de vorm van dergelijke heteroepitaxiale dunne lagen kunnen de eigenschappen volledig worden benut en beïnvloed door het onderliggend substraat, waarmee de kristalstructuur en -symmetrie kan worden gemanipuleerd. Gepulste laser depositie (PLD) is een uitermate geschikte methode om kunstmatige dunne lagen van perovskiet-type oxides te groeien, waarbij monokristallijne substraten met overeenkomstige roosterconstanten noodzakelijk zijn om volledige controle over de kristaloriëntatie te verwerven. Met deze techniek is het mogelijk de groei van een materiaal te beheersen op het niveau van een eenheidscel, maar slechts in de groeirichting. Gestandaardiseerde benaderingen om de groei in de andere richtingen te beheersen zijn niet voorhanden, terwijl een dergelijke controle onmisbaar is met het oog op toekomstige integratie in diverse apparatuur.

In dit proefschrift worden verschillende routes geïntroduceerd waardoor, tijdens PLD, epitaxiale patronen van perovskieten kunnen worden verkregen met lengteschalen van micrometers en daaronder. Patronen werden gemaakt door epitaxiale groei van een perovskiet op selectieve delen van een substraat toe te staan, of door de kristal oriëntatie van een dunne laag lokaal te sturen. De eerstgenoemde optie, het maken van patronen van een materiaal, werd uitgevoerd met behulp van tijdelijke micro- of nanostructuren die delen van een monokristallijn substraat afschermden, waardoor een perovskiet slechts op specifieke gebieden epitaxiaal kon groeien. Voor de andere optie, het lokaal controleren van de kristal oriëntatie, werden tweedimensionale anorganische nanokristallen met verschillende roosterconstanten gecombineerd op een enkel substraat om vervolgens de nucleatie en groei van een dunne perovskiet laag lokaal te reguleren. Deze verschillende benaderingen om patronen aan te brengen in epitaxiale dunne lagen hadden over het algemeen weinig invloed op de sterke controle over de groei die bereikt kan worden met PLD, aangezien veelal eigenschappen werden gemeten die behoren bij een goed georiënteerde dunne laag. Tegelijkertijd werden de eigenschappen beïnvloed door de patronen en lieten deze een duidelijke positie of richtingsafhankelijkheid zien, wat het potentiële nut van deze heterostructuren voor verschillende elektronische en elektromechanische toepassingen verhoogt.

Een eerste benadering om heteroepitaxiale patronen van perovskiet-type oxiden te maken combineert zachte lithografie met PLD, en bestaat uit twee opeenvolgende fabricagestappen waarbij in beide gevallen van beneden af een structuur wordt opgebouwd. In de eerste stap wordt een zachte mal gebruikt om een tijdelijk patroon van ZnO op een monokristallijn substraat te vormen. Na deze stap wordt PLD gebruikt om een negatieve en heteroepitaxiale replica van een perovskiet te verkrijgen, waarna het originele patroon van ZnO wordt verwijderd. Patronen van ZnO werden verkregen met lengteschalen in een bereik van micro- en nanometers, waarbij deze patronen de complete oppervlaktes van de substraten bestreken en er zich geen residu laag tussen de structuren bevond. ZnO werd gebruikt vanwege de compatibiliteit met de hoge temperaturen die bereikt worden tijdens PLD en vanwege de eenvoud waarmee het, na gebruik, verwijderd kan worden door te profiteren van het amfotere karakter. Lijnen met een periodiciteit van minder dan een micrometer werden vervaardigd van $La_{0.67}Sr_{0.33}MnO_3$, waarvoor de magnetische anisotropie sterke overeenkomsten vertoonde met die van een volledig georiënteerde dunne laag en een vormanisotropie gemeten werd als bijdrage van het lijnpatroon. Patronen met afmetingen van enkele micrometers werden gemaakt van $SrRuO_3$ die aantoonbaar elektrisch geïsoleerd van elkaar bleken te zijn. De ontwikkelde zacht lithografische benadering kan flexibel worden ingezet om epitaxiale patronen met verscheidene vormen en afmetingen te fabriceren, en biedt unieke kansen voor fundamenteel onderzoek en het realiseren van technologische toepassingen.

Beperkingen die inherent zijn aan het gebruik van zachte mallen begrenzen de hoogte/breedte verhouding van de patronen, waardoor slechts vlakke epitaxiale structuren kunnen worden verkregen. Toepassingen in bijvoorbeeld katalyse of gas detectie vereisen dat de functionele materialen grote contactoppervlakten hebben en vragen dus om andere methoden om de patronen te fabriceren.

De benadering die werd onderzocht richt zich op zelforganisatie om heteroepitaxiale nanostructuren te vormen. PLD werd uitgevoerd met gemengde targets bestaande uit $PbZr_{0.2}Ti_{0.8}O_3$ en ZnO, waarbij ferroelektrische nanopilaren met een periodiciteit van ongeveer $40\ \mathrm{nm}$ werden gevormd door nauwkeurige controle van de depositie condities. Door het verhogen van de herhalingsfrequentie van de laser pulsen of de partiële zuurstof druk werden de patronen kleiner en ondergingen ze een verandering in de morfologie. Het verwijderen van ZnO leidde tot een toename van de tetragonaliteit van de nanostructuren van $PbZr_{0.2}Ti_{0.8}O_3$, wat erop wijst dat beide fasen coherent gekoppeld waren en de spanningen van elastische aard waren. Daarnaast werd een toegenomen elektromechanische reactie gemeten na verwijderen van de ZnO fase, welke echter achterbleef bij de waarde die verwacht wordt voor een bulk eenkristal van $PbZr_{0.2}Ti_{0.8}O_3$ met een enkel domein. Het grote contactoppervlak en de epitaxiale aard van deze nanostructuren kunnen niettemin onderscheidende voordelen opleveren ten opzichte van dunne lagen of bulk materiaal. Daarnaast kan het werk model staan voor de groei van andere perovskiet/ZnO composieten welke potentieel kunnen worden toegepast in andere velden.

In plaats van patronen van materialen te maken, kunnen dunne lagen met plaatsafhankelijke eigenschappen gemaakt worden door de kristal oriëntatie lokaal te controleren. Zoals gerapporteerd in dit proefschrift kunnen tweedimensionale nanokristallen fungeren als uniek middel om de nucleatie van dunne lagen te controleren op een niveau dat niet bereikt kan worden met monokristallijne substraten. Anorganische nanokristallen van $Ca_2Nb_3O_{10}$ en $Ti_{0.87}O_2$ werden op silicium substraten geplaatst, om vervolgens tijdens PLD de nucleatie van $SrRuO_3$ te controleren. Zowel de morfologie als de kristaloriëntatie van de dunne lagen van $SrRuO_3$ werden bepaald door de onderliggende tweedimensionale nanokristallen en epitaxiale groei werd aangetoond op beide typen nanokristallen. Dergelijke groei werd verklaard door de roosterconstanten van de tweedimensionale nanokristallen te vergelijken met die van $SrRuO_3$ en leidde tot voortzetting van de achtvlakkige zuurstof structuur. De tweedimensionale nanokristallen hadden een duidelijk effect op de magnetische eigenschappen van de dunne lagen, welke alleen na groei op nanokristallen anisotroop gedrag vertoonden. De kristallografische voorkeursrichting werd gevarieerd door $SrRuO_3$ te deponeren op een enkele laag waarin beide typen nanokristallen waren gemengd, wat suggereert dat tweedimensionale nanokristallen gebruikt kunnen worden om dunne lagen te groeien met positie afhankelijke eigenschappen.

Verschillende manieren werden geïntroduceerd om de groei van dunne lagen van $SrRuO_3$ bovenop de tweedimensionale nanokristallen te verbeteren. Een bufferlaag van $SrTiO_3$ werd gebruikt om de ruwheid van de dunne lagen van $SrRuO_3$ op nanokristallen van $Ca_2Nb_3O_{10}$ te reduceren tot een atomair niveau en twee lagen van $Ti_{0.87}O_2$ nanokristallen werden gestapeld om een sterk toegenomen voorkeursoriëntatie van de kristalrichting te verkrijgen. De dunne lagen hadden soortelijke weerstanden die in de buurt kwamen van die van volledig georiënteerde lagen en vertoonden magnetische anisotropie waarbij de voorkeursrichting van de magnetisatie en Curie temperatuur bepaald werden door de onderliggende tweedimensionale nanokristallen. Een patroon van deze twee typen nanokristallen werd gemaakt om de kristallografische oriëntatie en eigenschappen van $SrRuO_3$ lokaal te beheersen. Een ongeëvenaarde controle van de groei van dunne perovskiet lagen op onbehandelde Si substraten werd geïllustreerd. De methoden die werden ontwikkeld om $SrRuO_3$ op tweedimensionale nanokristallen te groeien vormen dan ook een goede uitgangspositie voor de groei van kunstmatige heteroepitaxiale dunne lagen die een bodem elektrode behoeven. Controle is niet slechts bereikt in de richting van de laaggroei, aangezien de kristallografische voorkeursrichting lokaal geregeld werd op de oppervlaktes van micropatronen van de twee typen nanokristallen. Het concept om de oriëntatie en eigenschappen van dunne lagen lokaal te bepalen schept nieuwe mogelijkheden voor de fabricage van heterostructuren die wellicht in de toekomst toepassingen vinden.

Dit proefschrift eindigt met een vooruitblik, dat inleidende resultaten bevat die voortvloeiden uit het werk dat gepresenteerd is in de voorgaande hoofdstukken. Limieten van de zacht lithografische methode worden behandeld en twee alternatieve benaderingen worden voorgesteld met het doel tot verdere miniaturisering. Daarnaast wordt het concept om georiënteerde dunne lagen van hittebestendige naar flexibele substraten over te plaatsen behandeld. Deze mogelijkheid kan een nieuwe weg banen voor studies naar het gedrag van dergelijke dunne lagen wanneer deze gebogen worden en kan leiden tot toepassingen van epitaxiale dunne lagen in flexibele elektronica.

DANKWOORD

De afgelopen vier jaren heb ik een droom mogen verwezenlijken door te werken aan het in dit proefschrift beschreven promotieonderzoek. Veel mensen hebben een bijdrage geleverd aan deze fantastische tijd, zowel op de werkvloer als in de privésfeer. Graag wil ik de laatste pagina's van dit proefschrift besteden aan het bedanken van een ieder die hierin een rol heeft gespeeld.

Om te beginnen wil ik André en Gertjan bedanken voor de begeleiding van dit onderzoek. Jullie hebben mij vanaf het begin haast volledige vrijheid gegeven in de invulling van dit project, waarbij jullie telkens een torenhoog vertrouwen uitstraalden. Vaak leek jullie vertrouwen veel groter dan dat van mijzelf, maar juist uit dit vertrouwen wist ik een flinke dosis energie te putten. Ik wil jullie ook bedanken voor alle suggesties die jullie mij de afgelopen jaren hebben gegeven, want deze hebben een cruciale bijdrage geleverd aan de kwaliteit van dit werk en mijn eigen ontplooiing.

Er zijn veel mensen waarmee ik de afgelopen jaren heb samengewerkt en een deel wil ik graag in het bijzonder kort noemen. Antony, thank you for your inspiration and help during the time we were office mates, and Suresh thank you for familiarizing me with nanosheets. I would like to thank Sean Thomas and Jing Xia for performing the local magnetic measurements. Mark Smithers, bedankt voor de vele gezellige uren achter de SEM en interessante momenten waarin we de EBSD leerden kennen. Petra en David, het was mij een groot genoegen jullie te mogen begeleiden tijdens jullie masteropdrachten en ik ben blij dat een significant deel van dit proefschrift tot stand is gekomen met jullie resultaten. Wouter en Bouwe, bedankt voor de samenwerking en interessante TOP bijeenkomsten met soms een bijna onbeperkte toestroom van ideeën.

Ik heb een geweldige tijd gehad bij IMS, en heb veel goede herinneringen aan de besprekingen, colloquia en tijd die ik doorbracht in de labs, in het kantoor of aan de koffietafel. In het bijzonder wil Ik Guus, Dave, Mark, en Bernard bedanken voor hun kritische kijk en input tijdens de verschillende meetings en op andere momenten. Then I would like to thank some of the 'chemical brothers' for the always pleasant working atmosphere and the sometimes hilarious moments in the lab; in this context I would like to name Rogier, Sjoerd, Pablo, Gerard, Huiyu and Alessandro. I would also like to thank the MASIF team for all the hours we spend together on fixing the PLD system and keeping it operational, in particular I would like to mention Peter, Alim, and Matjaz. Ook wil ik Henk en Dominic van IMS, en Frank en Dick van ICE bedanken voor alle technische ondersteuning; en José en Marion voor hun ondersteuning bij financiële en administratieve zaken. Daarnaast zijn er nog een groot aantal andere personen binnen IMS die ik wil bedanken voor de inspiratie en hulp die ze mij de afgelopen jaren geboden hebben: Rik, Tom, Kenan, Kurt, Werner, Brian, Ruud, Josée, Michelle, Anirban, Ronald, Peter de Veen, Nicolas, Hans, Jeroen, Michiel, Tomasz, Evert, Hajo, Minh, Ben, Xin, Tjeerd, Zhaoliang, Lin, Anuj, Kees, Laura, Muhammed, Ole, Debakanta, Thomas, Wouter Vijselaar, Herman, Melanie, Bahruz, Tom Hammer, Vera, Jasper, Jaap, en Roy.

Ik wil hierbij ook mijn paranimfen Nirupam en Bindikt bedanken. Nirupam, wanneer ik eens een avondje ongestoord hard wou doorwerken, wist jij mij te vinden en mij van mijn werk te houden. Ik heb deze 'rooibosmomentjes' en de gesprekken die we hadden altijd erg gewaardeerd. Bindikt, in de eerste jaren van onze studietijd hebben wij vaak samengewerkt aan verscheidene practica en zo de eerste beginselen geleerd. Gelukkig hebben we ook in de daarop volgende jaren altijd contact gehouden en ik ben dan ook zeer blij dat jij nog een keer stil mag zitten terwijl ik al het werk doe.

Tot slot wil ik mijn vrienden, familie en schoonfamilie bedanken, vooral voor het zorgen voor de nodige afleiding. In het bijzonder wil ik mijn ouders bedanken, die beiden hun handen vol hebben gehad aan oppassen en klussen in en om het huis. Ook wil ik mijn kleine bengel Mats bedanken, jij was het die mij gedurende de afgelopen twee jaar steeds weer duidelijk maakte wat er werkelijk toe doet. Een laatste woord van dank is voor mijn lieve vrouw. Selma, bedankt voor al je steun en liefde de afgelopen jaren, ik vind het een geweldig idee om samen met jou de toekomst tegemoet te mogen gaan!

Maarten Nijland